Forschungszentrum Jülich
in der Helmholtz-Gemeinschaft
50 Jahre / Zukunft

# Finite Element Simulation of Stress Evolution in Thermal Barrier Coating Systems

Piotr Bednarz


Energietechnik
Energy Technology

Schriften des Forschungszentrums Jülich
Reihe Energietechnik / Energy Technology Band / Volume 60

Forschungszentrum Jülich GmbH
Institut für Energieforschung (IEF)
Werkstoffstruktur und Eigenschaften (IEF-2)

# Finite Element Simulation of Stress Evolution in Thermal Barrier Coating Systems

Piotr Bednarz

Schriften des Forschungszentrums Jülich
Reihe Energietechnik / Energy Technology Band / Volume 60

ISSN 1433-5522 ISBN 978-3-89336-471-8

Bibliographic information published by the Deutsche Nationalbibliothek.
The Deutsche Nationalbibliothek lists this publication in the Deutsche Nationalbibliografie; detailed bibliographic data are available in the Internet at http://dnb.d-nb.de.

| | |
|---|---|
| Publisher and Distributor: | Forschungszentrum Jülich GmbH<br>Zentralbibliothek, Verlag<br>D-52425 Jülich<br>Telefon (02461) 61-5368 · Telefax (02461) 61-6103<br>e-mail: zb-publikation@fz-juelich.de<br>Internet: http://www.fz-juelich.de/zb |
| Cover Design: | Grafische Medien, Forschungszentrum Jülich GmbH |
| Printer: | Grafische Medien, Forschungszentrum Jülich GmbH |
| Copyright: | Forschungszentrum Jülich 2007 |

Schriften des Forschungszentrums Jülich
Reihe Energietechnik / Energy Technology Band / Volume 60

D 82 (Diss., Aachen, RWTH, 2006)

ISSN 1433-5522
ISBN 978-3-89336-471-8

The complete volume is freely available on the Internet on the Jülicher Open Access Server (JUWEL) at http://www.fz-juelich.de/zb/juwel

"Dreams come true for those
who work while they dream.
Sweet dreams."
by H. Jackson Brown Jr.

## Acknowledgements

This thesis is the product of years of work, procrastination, changing minds and opinions. It is a delight to acknowledge those who have supported me over the last years.

Firstly, I wish to express my deepest gratitude to my supervisor Prof. Dr. Lorenz Singheiser for his excellent concern and endless support during the course of my research study.

To Dr. Patrick Majerus, I owe thanks beyond measure for his tremendous help, for his many astute comments, stimulating discussions and critique of this work. Thanks for beeing always ready to share your wide knowledge, and also for your wise yet flexible approach. I also wish to thank my last minute proofreader, Mr. Philip J. Ennis was a lifesaver; with the eye of a knowledgeable technical scientific writer.

My very special thanks go to Lineo Makhele for being a constant source of encouragement and support in times of crisis, thanks for the your huge smiles and patience which kept me going despite all the frustrations of these last three years. Thanks also for effort to proofread various chapters of this thesis.

I gladly acknowledge Dr. Iryna Marchuk, who has always been understanding and supportive. Thanks for being my friend. It gives me great pleasure to thank Dr. Teresa Majerus for putting up with me and this thesis. Many thanks go to Dr. Tatyana Kashko for the interesting discussions about science and other secret topics.

I must surely thank Dr. Roland Herzog for the contribution that he has made to my hard work. What would this thesis be like without your remarks?

Finally, the encouragement provided by my parents, family and close friends, during this work has been a constant form of support and motivation. I acknowledge my brother Dr. Eugeniusz Bednarz for the funny time in the childhood as well as now. Personal thanks are due to numerous people around the world, to everyone who has made the past three years memorable, interesting and enjoyable.

# Abstract

**Finite Element Simulation of Stress Evolution in Thermal Barrier Coating Systems**

by Piotr Bednarz

Gas turbine materials exposed to extreme high temperature require protective coatings. To design reliable components, a better understanding of the coating failure mechanisms is required. Damage in *Thermal Barrier Coating Systems* (TBCs) is related to oxidation of the *Bond Coat*, sintering of the ceramic, thermal mismatch of the material constituents, complex shape of the BC/TGO/TBC interface, redistribution of stresses via creep and plastic deformation and crack resistance. In this work, experimental data of thermo-mechanical properties of CMSX-4, MCrAlY (Bond Coat) and APS-TBC (partially stabilized zirconia), were implemented into an FE-model in order to simulate the stress development at the metal/ceramic interface. The FE model reproduced the specimen geometry used in corresponding experiments. It comprises a periodic unit cell representing a slice of the cylindrical specimen, whereas the periodic length of the unit cell equals an idealized wavelength of the rough metal/ceramic interface. Experimental loading conditions in form of thermal cycling with a dwell-time at high temperature and consideration of continuous oxidation were simulated. By a stepwise consideration of various material properties and processes, a reference model was achieved which most realistically simulated the materials behavior. The influences of systematic parameter variations on the stress development and critical sites with respect to possible crack paths were shown. Additionally, crack initiation and propagation at the peak of asperity at BC/TGO interface was calculated. It can be concluded that a realistic modeling of stress development in TBCs requires at least reliable data of i) BC and TGO plasticity, ii) BC and TBC creep, iii) continuous oxidation including in particular lateral oxidation, and iv) critical energy release rate for interfaces (BC/TGO, TGO/TBC) and for each layer. The main results from the performed parametric studies of material property variations suggest that porosity in the TBC should be increased and sintering decreased, in order to prevent or hinder continuous paths of tensile stresses above the valleys in the TBC. It was shown that variations of creep rates in the BC influence marginaly stress values in TBCs . Therefore neither a positive nor a negative influence on the lifetime can be extrapolated. It was shown that higher creep rates in the TBC layer led to a lower stress level. The extreme variations of thermal expansion coefficient ($\pm 50\%$) help in better understanding of these variations on stress development. The creep of base material only slightly affects stress field development, under pure thermal cycling and can therefore be neglected in this case. As the tensile stresses increase with a relatively high fraction of lateral oxidation not only the out-of-plane oxidation kinetics, but also its lateral component should be low. The modification of amplitude and wavelength of the asperity showed that with increasing roughness a continuous radial tensile path in the TBC and partially in the TGO was formed already after 161 cycles. The variations of wavelength, amplitude and shapes improve the understanding of stress development. The large variety of parametric variations studied by the present work in a highly complex and rather realistic FE model contribute significantly to an enhanced understanding of TBCs. This is supported by the final conclusion, that the set of crucial parameters could be reduced to the time dependent deformation behavior of TBC and TGO, the oxidation kinetics, including lateral oxidation and the shape function of the interface asperity.

# Contents

# List of Figures

# List of Tables

# Nomenclature

**TBCs** Thermal Barrier Coating system

**TBC** Thermal Barrier Coating (ceramic layer)

**TGO** Thermally Grown Oxide

**BC** Metallic Bond Coat

**Base Material** Metallic blade material (such as CMSX-4 Superalloys )

**Asperity** Interface shape between the BC and TBC

**Positions**

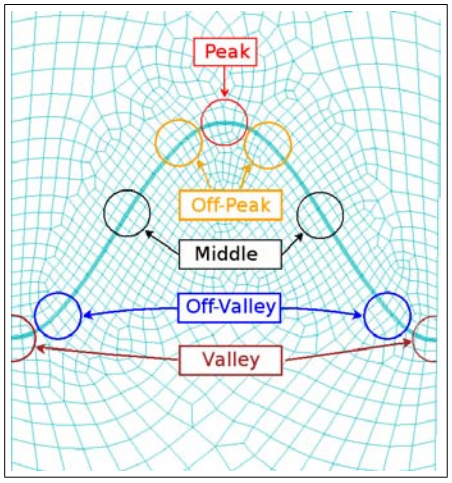


**APS** Air-Plasma Spray

**EB-PVD** Electron-Beam Physical Vapor Deposition

**FE** Finite Element

**FEA** Finite Element Analysis

**FEM** Finite Element Method

| | |
|---|---|
| $\mathbf{F}$ | Deformation gradient |
| $dX$ | Linear element at reference configuration |
| $dx$ | Linear element at current configuration. |
| $ds$ | Length of the linear element at reference configuration |
| $dS$ | Length of the linear element at current configuration |
| $E$ | Lagrange strain tensor |
| $e$ | Euler strain tensor |
| $\sigma_{ij}$ | Stress tensor |
| $T_j$ | Stress vector |
| $n_j$ | Normal vector |
| $C_{ijkl}$ | Stiffness tensor |
| $\varepsilon_{ij}^{tot}$ | Total strain tensor |
| $\varepsilon_{ij}^{el}$ | Elastic strain tensor |
| $\varepsilon_{ij}^{pl}$ | Plastic strain tensor |
| $\varepsilon_{ij}^{cr}$ | Creep strain tensor |
| $\varepsilon_{ij}^{th}$ | Thermal strain tensor |
| $\varepsilon_{ij}^{ox}$ | Oxidation strain tensor |
| $\alpha$ | The physical thermal expansion coefficient |
| $\Delta T$ | Change of temperature |
| $\hat{\alpha}$ | Engineering or secant thermal expansion coefficient |
| $T$ | Tempeature |
| $T_{ref}$ | A temperature of the strain free state |
| $Q$ | Plastic potential |
| $\dot{\lambda}$ | A proportional and positive scalar factor |
| $F$ | Yield function |
| $J_1$ | First stress invariant |
| $J_2$ | Second stress invariant |

| | |
|---|---|
| $J_3$ | Third stress invariant |
| $S_{ij}$ | Deviatoric stress tensor |
| $\kappa$ | A critical value |
| $\varepsilon^{\hat{cr}}$ | The uniaxial equivalent creep strain |
| $p$ | The equivalent pressure stress |
| $\hat{\sigma}$ | The equivalent deviatoric stress |
| $A'$ | First primary Norton creep pre-factor |
| $A''$ | Second primary Norton creep pre-factor |
| $A$ | Secondary Norton creep pre-factor |
| $n'$ | First primary Norton creep power |
| $n''$ | Second primary Norton creep power |
| $n$ | Secondary Norton creep power |
| $\varepsilon'$ | First primary strain |
| $\varepsilon''$ | Second primary strain |
| $\varepsilon$ | Secondary strain |
| $t$ | Time |
| $\Delta t$ | Time increment |
| $d^{ox}$ | Oxide thickness |
| $A_{Ox}$ | Oxidation pre-factor |
| $E_A$ | Oxidation activation energy |
| $R$ | Ideal gas constant |
| $n_{ox}$ | Power factor |
| $d^{ox}_{tot}$ | Total thickness of oxide layer |
| $d^{ox}_0$ | Initial thickness of oxide layer |
| $\Delta d^{ox}$ | Increase of the oxide thickness |
| $\hat{t}_i$ | Traction forces |
| $u_i$ | Displacement conditions |

**Nomenclature**

| | |
|---|---|
| $N_i$ | Shape function |
| $\mathbf{q}$ | Nodal displacement vector |
| $\mathbf{K}$ | Stiffness matrix |
| $\mathbf{F}_B$ | Body loads |
| $\mathbf{F}_\sigma$ | External loads |
| **NURBS** | Non-Uniform Rational B-Spline |
| **DOF** | Degree of Freedom |
| **GPS** | General Plain Strain |
| **RT** | Room temperature |
| **SEM** | Scanning Electron Microscope |
| $A_h$ | Amplitude of interface |
| $\lambda_w$ | A wavelength of interface |
| $\int_{S_a}^{S_b} C(s)ds$ | A length of interface curve |

# Introduction

Continuous development of industrial gas turbine technology is leading to more severe loading conditions for the metallic components via increase of turbine inlet temperature. This increase is related to the improvement of energy conversion in power plants, which in the most modern ones is currently achieved to be in the range from 58% to 60% . Consequently, refinement of the metallic components will contribute to environmental protection, as well as an economical benefit would be reached. Any increase of inlet temperature is a challenge. However, it has to be emphasized that materials able to withstand temperatures above $1050^oC$ and at the same time resist the high mechanical demand the main components of gas turbines are subjected to, do not still exist. In past years it became clear that a further development of base material to operate at increasingly higher temperature will not be sufficient to reach the targets. Therefore, a multi layer structure has been introduced to protect the materials against high temperature and it is called thermal barrier coatings (TBC). In such a system we can identify at least four parts, namely: the base material, a bond coat, a thermally grown oxide and the thermal barrier coating itself. Such a system has the advantage of a ceramic layer on the hot side of the cooled component, which withstands high temperature. On the colder side, a metallic base materials guarantees the required mechanical strength. A schematic drawing of a **TBC** system with a temperature gradient over the structure is shown in Fig. 1.1

Introducing a more effective system increases the lifetime of a multi layer metallic component under high temperature loading, but it requires better models, to predict the lifetime relevant parameters. The lifetime of a component depends on stress development, which controls crack initiation (formation) and propagation. Moreover, materials properties of each layer and the shape of the oxide layer influence stresses in TBC's, because of a complex interaction of elastic, plastic, creep, thermal, oxidation, phase transformation and sintering.

The top layer protects metallic blade material against high temperature. The thermal conductivity of this layer (**TBC**) is very low in comparison with others layers, but during operation time in this layer the process of sintering is present. **A***ir*-**P***lasma* **S***pray* (**APS**) or **E***lectron*-**B***eam* **P***hysical* **V***apor* **D***eposition* (**EB-PVD**) techniques are commonly used for production of *Thermal Barrier Coatings* (Fig. 1.2 has been published [37] and was kindly provided by P. Majerus). This coating consist of partially stabilized zirconia ($ZrO_2$) with $7 \pm 1$ wt.% $Y_2O_3$ (YSZ). The thermomechanical properties depend on the coating technique. Coatings produced by EB-PVD are more strain resistant,

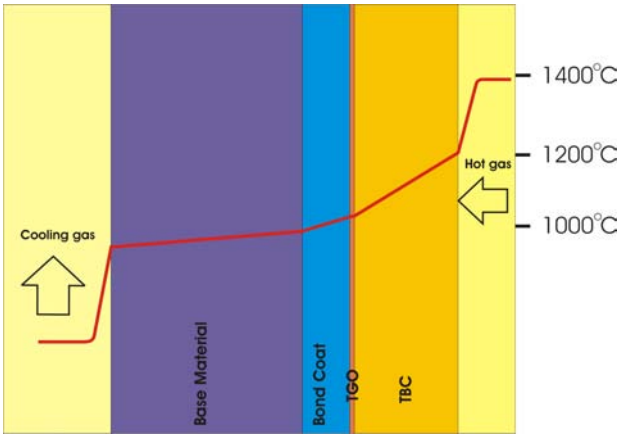


Figure 1.1: Scheme of thermal barrier coating System with temperature distribution along the cross section of the internally cooled componet.

but have higher values of thermal conductivity. APS-TBC coatings are more cost attractive and are characterized by a lower thermal conductivity, as they contain splats parallel to the interface (Fig. 1.2(a)). Further, important difference between them is the different shape of the interface between BC and TBC. During operation this layer oxidise, forming $Al_2O_3$ scale which causes a depletion of Al in the BC and dissolution the $\beta$ -phase (NiAl). Those processes have an impact on material properties and lifetime. The growth of the oxide layer further introduces extra strains. This makes this interface a weak point in the thermal protective system. Therefore, the oxidation induced spallation of plasma-sprayed thermal barrier coatings (APS-TBCs) is regarded as a one of the major failure modes in gas turbine components. The intermediate MCrAlY

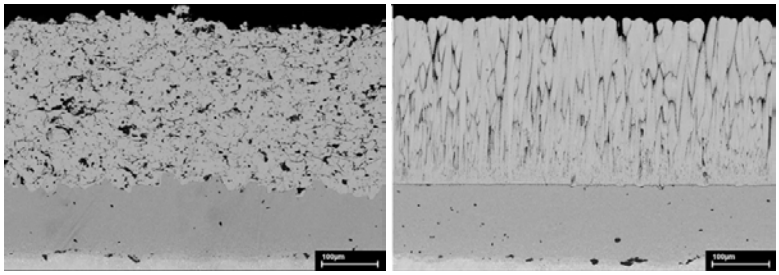

(a) APS (b) EB-PVD

Figure 1.2: Microstructure of a typical TBC

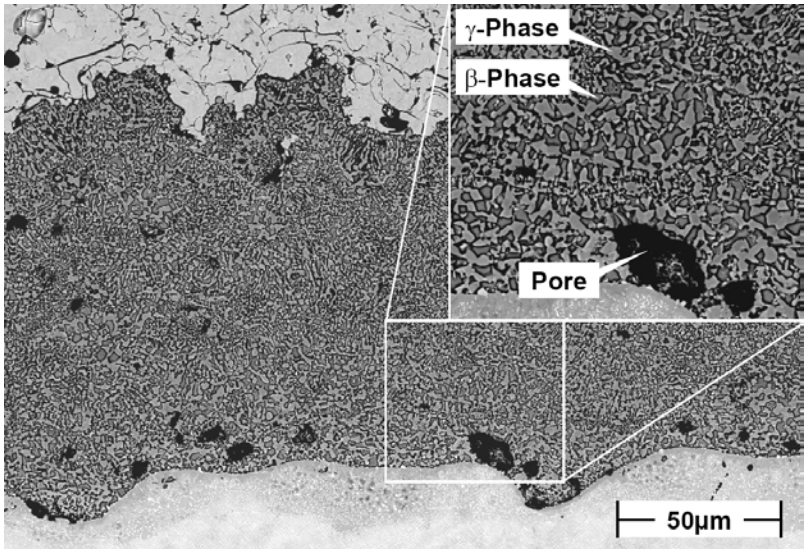


Figure 1.3: Two-phase MCrAlY

*Bond Coat* layer has been added to protect the base material against oxidation and to improve the adhesion of the TBC.

Fig. 1.3 shows two-phase (ß /$\gamma$) MCrAlY [37]. A failure crack path, which is located partly in the thermally grown oxide (TGO) and partly in the TBC, characterizes this type of failure (grey failure). Recent investigations have shown that the related damage evolution starts within the first 10% of lifetime by the formation of microcracks in the TGO and by opening of pre-existing microcracks in the TBC. Crack growth and linking of these cracks along the metal/ceramic interface lead to final spallation. However, parameters, which govern the kinetics and thus the lifetime are not sufficiently known. In order to quantify the influence of each parameter and by that complete the experience gained from long-term application in gas turbines as well as intensive experimental investigation, systematic numerical studies need to be performed.

The main goal of this work is to improve the understanding of stress development in TBC's, its relation to crack formation, and the crack growth. This can be achieved by a systematic and consistent development of numerical models. The present contribution shall determine the stresses near the TGO as a function of time under thermal cycling with high temperature dwell-time (cyclic oxidation) using the finite element method. A systematic development via a stepwise improvement of the model by studying a variety of interface shapes, checking the influence of different materials behavior, and considering continuous oxidation is performed. Moreover, one crack type is more often reported, i.e. crack formation at the BC/TGO interface at peak regions of undulations. It is observed to propagate through the TGO at the flanks of

undulations and to penetrate into the TBC over valleys. The current simulation results are particularly compared to these experimental findings.

# Literature overview

The interface between a plasma sprayed *Thermal Barrier Coating* (TBC) and the metallic corrosion protective coating, the *Bond Coat* (BC) has a complex shape (see Fig. 1.3). In a 2D approach, this shape can be simplified as sinusoidal, semicircle, semiellipsoid or any other geometrical function. The stress development in thermal barrier coating systems (TBCs) depends on oxidation induced stresses, thermal mismatch between layers, shape of interface, inelastic time independent (plastic), and time dependent (creep) deformation. Moreover, pre-existing splats or voids in the ceramic coating create additional concentration of stresses. Such splats act as free traction planes (microcracks).

The oxidation induced stresses produce volume change [7; 8; 9; 17; 19; 44] as well as to a change of properties with increasing of the oxide layer. These stresses can be split into two parts, namely out of plane oxidation and lateral oxidation (lengthening). The oxidation process is governed by cation diffusion on the outer surface or anion diffusion which predominates oxidation at the metal/oxide interface [8; 9; 19]. Moreover, the growth of oxide is related to Al consumption from Bond Coat matrix which results in ß - depletion in the bond coat. This ß - depleted zone is more creep resistant [37]. The present chapter gives an overview over the different approaches to analytically and numerically study the multiple influencing parameters, as included in the open literature.

## 2.1 Analytical study

Analytical models of convex and concave asperities with assumption of three-concentric-circles and three phases, namely bond coat, *Thermally Grown Oxide* (TGO) and ceramic, were considered by Hsueh [27; 28]. Residual thermal stresses at the TGO/bond coat and the TGO/ceramic interface were presented as a function of TGO thickness. This thickness depends on the radius of BC/TGO interface (r=a) and TGO/TBC interface(r=b). It was shown that for a convex asperity residual stresses at the TGO/BC interface are tensile and increase with the thickness of the TGO. However, radial stresses at TGO/TBC interface are tensile when $\frac{b-a}{a} < 0.75$ and becomes compressive when $\frac{b-a}{a} > 0.75$. In the case of a concave asperity the radial stress at TGO/TBC interface is compressive, while the stress at the TGO/BC interface becomes less compressive with

an increase of the TGO thickness.

An analytical radial stress relation as a function of geometrical parameters of the bond coat roughness was obtained by Ahrens et al. 2002 [3]. It was clearly shown that the influence of interface curvature on stress field is not possible to obtain using a two-cylinders-model and that a bond coat peak cannot be modeled as a metallic inclusion in a ceramic matrix.

## 2.2 Numerical study

As analytical methods have failed to predict the stress development in the complex TBC system, numerical methods were used instead. Numerical studies based on an assumption of linearly temperature dependent material properties were done by Chang 1987 [12]. At this stage all materials were modeled as fully elastic. The driving forces of stress formation are a result of thermal mismatch (different thermal expansion coefficient) of the different layers. During cooling from high temperature to ambient temperature a concentration of radial tensile stresses at the tip of the asperity has been found [12]. It was pointed out that these stresses can easily initiate crack in the ceramic at the asperity. Moreover, the maximum shear stresses were obtained close to the TGO/TBC interface at the off-peak positions where failure has been observed in experiment.

It has been shown [12] that stresses related to oxidation strain have a significant effect on life time of the coating. These stresses increase with an increase of the TGO thickness and lead to stress transition from tension at the peak in the TBC layer to compression and from compression to tension at valleys, respectively. Such transition is directly related to the degradation mechanism of the BC/TBC interface by promoting cracks over the valley.

In addition the crack over the tip of the asperity has been studied. Its existence in the TBC layer redistributes the stresses around it. A cracking propagation scenario has been proposed. As the tensile stresses are concentrated at the peak in the TBC layer for a thin TGO, the crack could be initiated. Moreover, due to transition of compressive stresses to tensile at the valley, the crack may propagate further above the valley as compressive stresses are not present [12].

Based on the assumption of a fully elastic behavior of the TBC system a parametric study was performed by Hsueh [28]. In addition the convex and concave asperities were considered as well as different shapes of BC/TBC interface. The study confirmed previous findings for the case of convex interface, that for thin TGO tensile stresses occupy the peak of the interface in the TBC layer. During thickening these tensile stresses decrease and switch to compression. However, for the case of concave asperity the results were different and the valley was reported to be occupied by compressive stresses. Moreover, it was reported that above the valley, tensile stresses are present for thick TGO. It was concluded that multiple asperities reduce stresses at the tip of interface in TBC layer. Based on a parametric study of interface roughness and

oxide scale thickness Ahresen and co-authors [3] claimed that the stress conversion which always appears in TBC's for a certain value of the TGO thickness is delayed by increasing the roughness amplitude.

However TBC systems are not pure elastic materials. The stress response is increasingly complex when plastic and visoplastic behavior is included. The complex geometry of real EB-PVD samples with assumption of nonlinear plastic response of the *Bond Coat* and *oxide* layers has been studied by Cheng [13]. In his study, it was shown that plastic strain concentrates near the region of highest interface curvature. Moreover, the stresses obtained in the elastic case were higher in comparison with the elastoplastic response. It then was concluded that elastic calculations overestimate stresses in TBC's. The largest stresses were found in the TGO layer. It was further pointed out that irregular interfaces also concentrate large local tensile stresses in radial direction in the TGO.

The viscoplastic response of substrate, BC and TBC on stress development was investigated by Freborg et al. [20]. It was shown that creep at high temperature in both BC and TBC causes radial tensile stresses at RT at the roughness peak and compressive stresses at the valley regions. However, the oxidation process acts contrary to creep causing an increase of tensile stresses at valleys and pushing peak region to compression. Moreover, it was pointed out that in some cases, the tensile stress region over the valleys is capable of sustaining crack growth by linking of early-generated cracks near peak region. It was further concluded that the process of crack generation linking and final spallation is a combined action of creep, oxidation and thermal cycling [20].

The influence of interface roughness and oxide film thickness considering inelastic material behavior on stress development has been discussed by Pindera et al. [40]. The variation of roughness profile was also studied under assumption fully without oxide layer. It was shown that an increase of the BC/TBC roughness amplitude results in an increase of stresses at the valley and smaller increase of stresses at the peak in this location. However, decreasing amplitude decreases the stresses at the valley and at the peak, respectively. Moreover, these studies confirmed the important role of oxide thickness on stress development. It was further suggested that changing the strength of the alumina layer would result in lower delamintation initiation susceptibility at the peak of the BC/TGO/TBC interface.

The oxidation process is governed by diffusion of oxygen and alumina atoms. Coupling of diffusion laws and stress development has been done by Busso et al. [9]. Additionally a sintering effect, which manifests as densification of the TBC layer and stiffness increase of the TBC layer was taken into consideration. Furthermore, the maximum tensile stress located at the off-peak in the TBC has been correlated with mesocrack nucleation. Busso proposed a life prediction model based on damage mechanism [10]. This model assumed that APS-TBC failure emerge by cleavage-type damage of the TBC and the fatigue damage is related to the evolution of microscopic damage parameter D which is in the range from 0 to 1 (D=1 represents full damage of the TBC). Damage equation depends on maximal radial tensile stresses and macroscopically average cleavage strength of the TBC. The coupling of damage law with a FE-unit cell model is related to calculation of maximum radial tensile stress as function

of cycle number. This damage law is limited to cyclic thermal loading, because in the case of continuous isothermal oxidation dD/dN=0. Moreover, this model of damage assumes that the maximal radial tensile stress of the TBC is a composition of maximal radial tensile stresses such as thermal, oxidation and sintering stresses. However, the creep behavior of the TBC has not been considered.

Inelastic behavior, such as plastic or viscoplastic, redistribute the stresses in TBC's, but may also change interface roughness and amplitude known as rumpling. Moreover, cycling loading results in accumulation of inelastic strains such as plastic and creep, called ratcheting. A component under cyclic loading condition can further go under shakedown. Two processes of shakedown are distinguished, namely, elastic and plastic. If the loading and unloading path after a few cycles becomes elastic such a process is call elastic shakedown. In the case, that after a few cycles the stress hysteresis does not move and does not change in size such a process is call plastic shakedown. Additionally, the reverse yielding can take place in case of low yielding criteria and is manifested by plastic deformation under unloading conditions.

A number of researches are focused on ratcheting and displacement instability during cycling oxidation [21; 22; 31; 32; 33; 34]. It was shown that ratcheting under cycling thermal loading conditions requires at least two materials with significant difference in thermal expansion coefficient [21]. Studies by He [21] shows that amplitude changes of the interface roughness require a growth strain, otherwise after 10 cycles the interface roughness amplitude remains unchanged. Moreover, when undulations are smaller than the ratio $a_c/L$( where: $a_c$ is a critical amplitude and $L$ is a wavelength) the interface geometry remains stable.

The geometrical interface instability was discussed in dependence of the yield strength of BC by Karlsson [31; 32; 33; 34]. An unstable deformation of the oxide was observed with soft bond coats where $\sigma_Y \leq 250$ MPa. In the case of larger $\sigma_Y^{BC}$ values no reverse yielding took place [31; 34]. Additionally it was reported that the plastic strain and imperfection amplitude decrease or stop after few cycles as effect of higher yielding limit of BC. Moreover, other effects which expand the ratcheting domain were found, namely, i) high thermal expansion temperature misfit between bond coat and substrate, ii) the BC temperature dependent yield strength (soft at high temperature, but strong at room temperature).

The TGO shape distortions are also coming from lengthening of the TGO layer. In the case of increasing the grown strain in lateral direction, convolutions at the imperfection periphery were found [32]. Interface shape changes were also found to depend on the imperfection profile. However, only invert shape change was predicted in the case of a convex imperfection. Additionally the curvature of the shape is thought to have an influence on stress development.

Depending on the grains size of the TGO creep processes can take place [42; 43; 44; 46]. The major changes were obtained in the TGO layer itself. After cooling to ambient temperature the localization of tensile stresses at the tip of asperity were reported [44]. Moreover, if the oxidation rate is fast compared to creep rate, large tensile stresses were obtained in the TBC and the BC. This can lead to crack formation at the TBC valleys and at the BC peaks. Some design considerations were drawn, such us, the suggestion

of a soft bond coat which relaxes the stresses at operation temperature. Additionally, the volumetric expansion of the TGO which is related to oxidation should further be as small as possible. This means that the oxidation rate should also be minimized. Studies by Bäcker [4] show that TGO and TBC creep is beneficial for the lifetime of TBC's as tensile radial stresses decrease in the TGO and TBC layers. Therefore critical thickness of the oxide layer when failure occurs shifts to higher values from $7\mu m$ to $10\mu m$.

Pre-existing free traction planes in TBC's such as voids, microcraks were studied [33] with introduction of a crack in to the TBC model. It was found that instability develops preferentially in zones where defects such as free traction planes exist.

Not only was the FE-method used to simulate stress development and preexisting cracks in the TBC, but also the higher-order theory for functionally graded materials [41]. A crack above the tip of asperity was considered. It was found that normal stresses are not sufficient to provide necessary crack-driving forces with increasing oxide film thickness. Additionally, it was shown that the concentration of stresses always appears at the crack tip in the case of the absence of oxide layer without consideration of actual bond coat microstructure. Considering the microstructure of the bond coat reduces radial stress field at the tip of crack above the peak of interface, but increases the shear stress field at the crack tip and provides the necessary crack driving forces. It was pointed out that increasing the TGO thickness further increases the shear stress field.

As the TGO thickness plays an important role on stress developments and on lifetime, the oxide scale thickness was correlated with the lifetime of TBC system by claiming existence of critical value of the TGO thickness when failure occurs. Not only a 2D geometry of the oxide layer has been considered. Jinnestrand et al. 2001 [30] focused on a 3D geometrical oxide shape. The work also confirmed the high impact of oxide thickness on stress field developments in the TBC system. Moreover, it was pointed out [17; 18] that particularly in TBC's with an irregular interface shape, the morphological parameter influences the critical thickness of the TGO layer. It was reported that the critical crack length is one of the parameters, which can be correlated to the time when spallation would occur. Such a critical value of 8 [mm] has been estimated by Vaßen at al. [51].

The researchers tend to take a simple mechanical approach, such as combining stress results and experimental data to predict lifetime [49]. Other life prediction methods are based on energy release rate and stress distribution trying to predict crack growth [23; 47]. A pre-existing crack above the peak in the TBC has been considered by Sfar [47]. It was found that energy release rate strongly depends on oxide growth modes (isotropic, anisotropic). Moreover, it was pointed out that BC creep does not influence the results of energy release rate in the oxidation phase. Only prominent changes have been obtained during cooling phase. However, in this work TBC creep has not been considered. It was reported by others [38; 52; 53], that energy release rate depends also on imperfection and crack length.

Simulation of TBC degradation based on a cohesive zone model was performed by Caliez et al. 2003 [11]. The crack has been placed between bond coat and oxide

layer. The model shows a decrease of mechanical properties at the BC/TGO interface via degradation. Moreover, it was pointed out that the energy release rate is a local parameter and depends on the assumption of a fixed ratio between amplitude and wavelength as well as on the assumption of a periodic unit cell.

As transition from compression to tension of the radial stress at the valley of the TBC occurs during cycling thermal oxidation and by that promotes crack propagation in the TBC. Therefore possible improvements were proposed [29; 39; 45]. It was suggested that the interface BC/TBC should have a flat shape. This will reduce radial stress across interface. Moreover it was suggested to create a creep-resistant bond coat which will reduce further interface roughness by preventing rumpling. Additionally it has been pointed out an elimination of the splat boundaries in APS TBC, would result in an increase of durability. The elimination of these splats could be reached by a new spray method described by Jadhav [29]. To improve the strain tolerance of TBC, an introduction of vertical cracks (perpendicular to BC/TBC interface) was suggested. Additionally it was pointed out that introducing oxygen vacancies (point defects) would reduce thermal conductivity as well as sintering kinetics.

# Methods

## 3.1 Introduction

A body subjected to external or internal loads, deformation process takes place. One distinguishes between elastic, plastic or viscous plastic deformation. Elastic deformation fully recovers after unloading and no additional stress is introduced into the body. To fully describe the process of deformation and its importance on FE-calculations, the terms of stress and strain definitions need to be defined.

### 3.1.1 Strain

Let us imagine the continuous body at time $t_n$ which occupies the space $\beta_n$. This state will be referred to in the following as reference configuration. After deformation at the time $t_{n+1}$ the body occupies the new space $\beta_{n+1}$ and is called current configuration. Taking the line element dX at the reference configuration under assumption that after deformation this element stays linear, the new line element can be expressed as the relation between both configurations $\beta_{n+1}$ and $\beta_n$ (Fig. 3.1):

$$dx = \frac{\partial x}{\partial X} dX \tag{3.1}$$

where $\frac{\partial x}{\partial X}$ is called deformation gradient and usually written as $F$, $dX$ is the linear element at reference configuration and $dx$ is the linear element at current configuration. Because the transformation is reversible, an inverse tensor $F$ exists. Thus Eq. (3.1) can be rewritten as.

$$dX = \mathbf{F^{-1}dx} \tag{3.2}$$

Taking in to account the length of the linear element at reference and current configuration respectively, the following relations are obtained:

$$ds^2 = dxdx \tag{3.3}$$

$$dS^2 = dXdX \tag{3.4}$$

Substituting equations (3.1) and (3.2) to (3.3), respectively (3.4) gives.

$$\begin{aligned} ds^2 &= FdXFdX \\ &= dXF^TFdX \end{aligned} \tag{3.5}$$

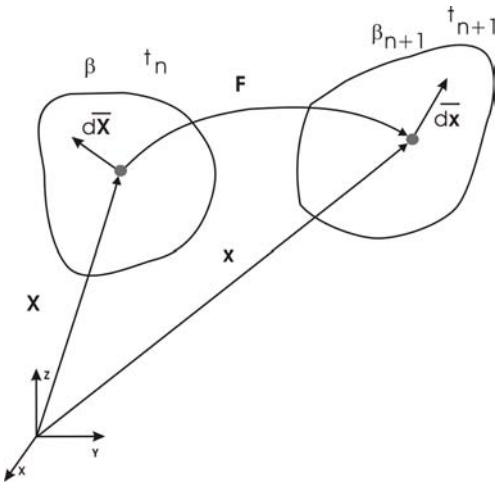


Figure 3.1: Total deformation gradient

$$\begin{aligned} dS^2 &= F^{-1}dxF^{-1}dx \\ &= dx\left(F^TF\right)^{-1}dx \end{aligned} \tag{3.6}$$

where $ds$ is the length of the linear element at the current configuration and $dS$ is the length of the linear element at the reference configuration.

To calculate the strain we need to know the difference in length between the linear elements $ds^2 - dS^2$. Taking in to account equations (3.5) and (3.6), the difference $ds^2 - dS^2$ can be expressed at reference (3.7) or current (3.8) configuration, respectively.

$$\begin{aligned} ds^2 - dS^2 &= dXF^TFdX - dXdX \\ &= dX\left(F^TF - 1\right)dX \end{aligned} \tag{3.7}$$

$$\begin{aligned} ds^2 - dS^2 &= dxdx - dx\left(F^TF\right)^{-1}dx \\ &= dx\left(1 - \left(F^TF\right)^{-1}\right)dx \end{aligned} \tag{3.8}$$

The expression in brackets can be written in the following way to represent Lagrange (3.9) and Euler (3.10) strain tensors.

$$E = \frac{1}{2}\left(F^TF - 1\right) \tag{3.9}$$

$$e = \frac{1}{2}\left(1 - \left(F^TF\right)^{-1}\right) \tag{3.10}$$

The strain tensor has in general 6 independent variables. The deformation field is described by three independent variables. Therefore, relations exist to constrain the

strain tensor. Those constrains are called consistency condition (3.11).

$$\varepsilon_{ij,kl} + \varepsilon_{kl,ij} - \varepsilon_{ik,jl} - \varepsilon_{jl,ik} = 0 \tag{3.11}$$

The deformation process is related to external or internal loads, but the solid body has to remain in equilibrium. This requires that two parts of a solid body, divided by any plane, have to be in equilibrium.

### 3.1.2 Stress

Let us assume a plane Π, dividing a solid body and take within a small area $\Delta A$ with a point P. On this area acts a force $\Delta F$ (Fig. 3.2). By taking a limit as follows:

$$\sigma = \lim_{\Delta A \to 0} \frac{\Delta F}{\Delta A} \tag{3.12}$$

the stress at point $P$ becomes defined. The stress vector ($T_i$) is acting on Π plane,

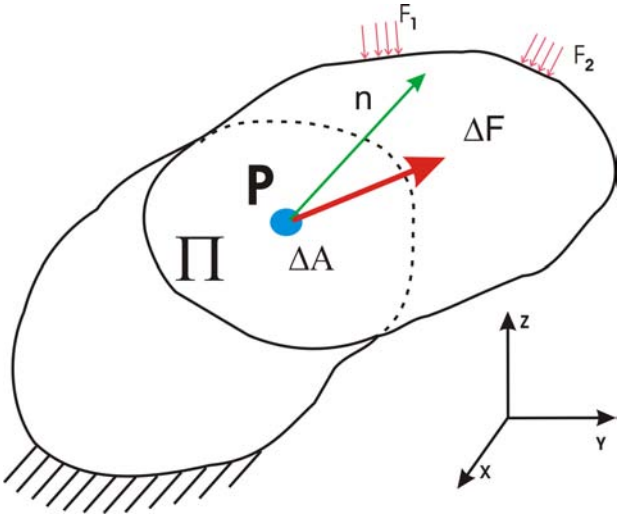


Figure 3.2: Stress at point P

relative to the (3.13) normal vector $n_i$ and the stress tensor ($\sigma_{ij}$).

$$T_i = \sigma_{ij} \cdot n_j \tag{3.13}$$

Stresses act at any point in solid bodies and have in general 9 independent values. In the no momentum theory these stresses are reduced to 6 independent variables and are equal in symmetry.

$$\sigma_{ij} = \sigma_{ji} \tag{3.14}$$

Moreover, the stresses act in a constitutive (3.15) relation with strain.

$$\sigma_{ij} = C_{ijkl}\varepsilon_{kl} \tag{3.15}$$

Where $C_{ijkl}$ is a 4 rank stiffness tensor.

### 3.1.3 Strain decomposition

Fig. 3.1 shows the total deformation gradient **F** between a reference and a current configuration. We can imagine the existence of an intermediate configuration, representing elastic, thermal, plastic, viscoplastic, oxidation induced, or other deformations.

Total strain is an additive composition of other strains coming from intermediate configurations (3.16). In its incremental form it can be written as(3.17).

$$\varepsilon^{tot} = \varepsilon^{el} + \varepsilon^{th} + \varepsilon^{pl} + \varepsilon^{cr} + \varepsilon^{ox} + ... \tag{3.16}$$

$$d\varepsilon^{tot} = d\varepsilon^{el} + d\varepsilon^{th} + d\varepsilon^{pl} + d\varepsilon^{cr} + d\varepsilon^{ox} + ... \tag{3.17}$$

Knowing total strain after loading, the elastic strain can be calculated if the other strain components are known.

#### 3.1.3.1 Thermal strain

Changing the temperature causes material to shrink or to expand. In the simplest case this is a proportional relation of the temperature decrease or rise. The proportional parameter is called coefficient of thermal expansion ($\alpha^{th}$). Thermal strains are defined by (3.18)

$$\Delta\varepsilon^{th}_{ij} = \alpha^{th}_{ij}\Delta T \cdot \delta_{ij} \tag{3.18}$$

where $\Delta T$ is the change in temperature.

**However a difference exists between the physical and the engineering thermal expansion coefficient** The physical definition of the thermal expansion coefficient is simply the temperature derivation operator over the thermal strain (3.19).

$$\alpha \equiv \frac{d\varepsilon_{th}}{dT} \tag{3.19}$$

To calculate thermal strain at any time the integration of Eq. (3.19) has to be preformed.

$$\varepsilon_{th} = \int_{T_0}^{T_1} \alpha dT \tag{3.20}$$

Using the definition of the secant operator, thermal strain can on the other hand be express in the following way (3.21).

$$\varepsilon_{th} \equiv \hat{\alpha} \cdot (T - T_{ref}) \tag{3.21}$$

Where $\hat{\alpha}$ is a engineering or secant thermal expansion coefficient, T is the current temperature and $T_{ref}$ is a temperature of the strain free state. In any experiment the measured values are thermal strain. The division of this strain by the difference between current and reference temperature defines the engineering coefficient. Such an approach is simpler, as the integration does not have to be performed.

#### 3.1.3.2 Plastic strain

Deformation involving energy dissipation with no time dependence is called plastic deformation. Due to energy dissipation the process of deformation is history or path dependent. In 1928 von Mises proposed a general mathematical approach of the constitutive equation for plasticity. He proposed that an existing plastic potential $Q(\sigma)$ and the plastic strain rate are represented by relation (3.22).

$$\dot{\varepsilon_{ij}^{pl}} = \dot{\lambda}\frac{\partial Q(\sigma_{ij})}{\partial \sigma_{ij}} \tag{3.22}$$

Where $\dot{\lambda}$ is a proportional and positive scalar factor. To determine this factor the yield criteria is used. This criterion describes the initial plastic surface. The general form of the yield function is

$$F(\sigma_{ij}) = 0 \tag{3.23}$$

In the case of isotropic material the yield depends on the stress invariant $J_1 = tr(\sigma)$, $J_2 = \frac{1}{2}\left(\sigma_{ii} \cdot \sigma_{kk} - \sigma_{ij} \cdot \sigma_{ij}\right)$ and $J_3 = det[\sigma_{ij}]$. For metallic materials the yield function is independent of hydrostatic pressure. So plastic yielding is only related to deviator stress. Following the Maxwell-Huber-Von Misses criterion we can express the yielding surface as function of the second invariant ($J_2'$) on the deviator stress ($S_{ij} = \sigma_{ij} - \frac{1}{3}\sigma_{kk}\delta_{ij}$). The stresses within the structure cannot exceed a critical value $\kappa$, otherwise plastic deformation takes place.

$$J_2' - \kappa^2 = 0 \quad for \quad yielding\ or\ plastic\ deformation \tag{3.24}$$

$$J_2' < \kappa^2 \quad for \quad elastic\ deformation \tag{3.25}$$

In the case the yield function is equal to the plastic potential the behavior is called associated plastic flow. Dissipative time dependent deformation is called creep or visco-plastic deformation.

#### 3.1.3.3 Creep strain

A large number of creep equations have been proposed to meet the experimental material response. The creep response has in general three different parts. The first part is primary creep, followed by a secondary and finally a tertiary part. To describe the material response, a new law covering primary and secondary part is proposed in the present work.

The creep strain rate following a general form (3.26) can be written as follows.

$$\dot{\varepsilon}^{cr} = f^{cr}(p, \hat{\sigma}, \varepsilon^{\hat{cr}}, t) \tag{3.26}$$

where:

- $\varepsilon^{\hat{cr}}$ is the uniaxial equivalent "creep" strain, conjugate to Mises or Hill equivalent stress
- $p$ is the equivalent pressure stress, $p = \frac{1}{3}\sigma_{ii}$
- $\hat{\sigma}$ is the equivalent deviatoric stress (Mises' or if anisotropic creep behavior is defined the Hill's definition).

In its general form, the creep law is written as

$$\dot{\varepsilon}_{cr} = A'\hat{\sigma}^{n'} e^{-\frac{\varepsilon\hat{cr}}{\varepsilon'}} + A''\hat{\sigma}^{n''} e^{-\frac{\varepsilon\hat{cr}}{\varepsilon''}} + A\hat{\sigma}^{n} \tag{3.27}$$

This law is a function of $\hat{\sigma}$, $\hat{\varepsilon}^{cr}$ and time (3.28)

$$\varepsilon_{cr} = f(\hat{\sigma}, \hat{\varepsilon}_{cr}, t) \tag{3.28}$$

To calculate the change in creep strain in a derived time increment Eq. (3.27) can be written in the form:

$$\Delta\varepsilon_{cr} = \left(A'\hat{\sigma}^{n'} e^{-\frac{\hat{\varepsilon}_{cr}}{\varepsilon'}} + A''\hat{\sigma}^{n''} e^{-\frac{\hat{\varepsilon}_{cr}}{\varepsilon''}} + A\hat{\sigma}^{n}\right)\Delta t \tag{3.29}$$

Additionally other derivations can be defined ( 3.30 to 3.32).

$$\frac{\partial\Delta\varepsilon_{cr}}{\partial\hat{\sigma}} = \left(A'n'\hat{\sigma}^{n'-1} e^{-\frac{\hat{\varepsilon}_{cr}}{\varepsilon'}} + A''n''\hat{\sigma}^{n''-1} e^{-\frac{\hat{\varepsilon}_{cr}}{\varepsilon''}} + An\hat{\sigma}^{n-1}\right)\Delta t \tag{3.30}$$

$$\frac{\partial\Delta\varepsilon_{cr}}{\partial\hat{\varepsilon}_{cr}} = \left(A'\hat{\sigma}^{n'} e^{-\frac{\hat{\varepsilon}_{cr}}{\varepsilon'}} \cdot \frac{-1}{\varepsilon'} + A''\hat{\sigma}^{n''} e^{-\frac{\hat{\varepsilon}_{cr}}{\varepsilon''}} \cdot \frac{-1}{\varepsilon''}\right)\Delta t \tag{3.31}$$

$$= -\left(\frac{A'\hat{\sigma}^{n'} e^{-\frac{\hat{\varepsilon}_{cr}}{\varepsilon'}}\cdot}{\varepsilon'} + \frac{A''\hat{\sigma}^{n''} e^{-\frac{\hat{\varepsilon}_{cr}}{\varepsilon''}}}{\varepsilon''}\right)\Delta t \tag{3.32}$$

Setting $A''$ in eq. (3.27) to 0 a reduce law (3.33) is obtained.

$$\dot{\varepsilon_{cr}} = A'\hat{\sigma}^{n'} e^{-\frac{\hat{\varepsilon_{cr}}}{\varepsilon'}} + A\hat{\sigma}^{n} \tag{3.33}$$

A reduce implementation has been choosen to avoid unnecessary numerical operation. The full set of equations for the user creep subroutine in HKS/ABAQUS is listed bellow (3.34,3.35 and 3.37)

$$\Delta\varepsilon_{cr} = \left(A'\hat{\sigma}^{n'} e^{-\frac{\hat{\varepsilon}_{cr}}{\varepsilon'}} + A\hat{\sigma}^{n}\right)\Delta t \tag{3.34}$$

$$\frac{\partial\Delta\varepsilon_{cr}}{\partial\hat{\sigma}} = \left(A'n'\hat{\sigma}^{n'-1} e^{-\frac{\hat{\varepsilon}_{cr}}{\varepsilon'}} + An\hat{\sigma}^{n-1}\right)\Delta t \tag{3.35}$$

$$\frac{\partial\Delta\varepsilon_{cr}}{\partial\hat{\varepsilon}_{cr}} = A'\hat{\sigma}^{n'} e^{-\frac{\hat{\varepsilon}_{cr}}{\varepsilon'}} \cdot \frac{-1}{\varepsilon'}\Delta t \tag{3.36}$$

$$= -\frac{A'\hat{\sigma}^{n'} e^{-\frac{\hat{\varepsilon}_{cr}}{\varepsilon'}}\cdot}{\varepsilon'}\Delta t \tag{3.37}$$

#### 3.1.3.4 Oxidation induced strain

During oxidation processes, a volume expansion of the oxide layer (TGO) takes place. Thus can be represented numerically in terms of swelling strain. The equation to formulate oxidation as swelling strain has been derived and implemented into HKS/ABAQUS, as explained by the following.

Oxidation kinetics has been identified in isothermal oxidation experiments and fitted to Eq.(3.38) by Echsler [15].

$$d^{ox} = \left( A_{ox} \cdot e^{-\frac{E_A}{R \cdot T}} \cdot t \right)^{n_{ox}} \tag{3.38}$$

The swelling strain used by the user subroutine is a true strain. Therefore the oxidation scale thickness of a defined time step is expressed as true strain (3.39)

$$\varepsilon^{ox} = \ln \left( \frac{d^{ox}_{tot}}{d^{ox}_{0}} \right) \tag{3.39}$$

where $d^{ox}_{tot}$ is the thickness at the end of the step and $d^{ox}_{0}$ is the thickness at the beginning. From equation (3.39) we can explicitly write the increment of oxidation strain as (3.41).

$$\Delta\varepsilon^{ox} = \ln \left( \frac{d^{ox}_{tot}}{d^{ox}_{0}} \right) - \ln \left( \frac{d^{ox}_{t}}{d^{ox}_{0}} \right) \tag{3.40}$$

$$= \ln \left( \frac{d^{ox}_{tot}}{d^{ox}_{t}} \right) \tag{3.41}$$

The total thickness of TGO can be expressed as (3.42).

$$d^{ox}_{tot} = d^{ox}_{t} + \Delta d^{ox} \tag{3.42}$$

where $d^{ox}_{t}$ is the thickness at the beginning of the previous step. Substituting equation (3.42) in to the (3.41) gives (3.44).

$$\Delta\varepsilon^{ox} = \ln \left( \frac{d^{ox}_{t} + \Delta d^{ox}}{d^{ox}_{t}} \right) \tag{3.43}$$

$$= \ln \left( 1 + \frac{\Delta d^{ox}}{d^{ox}_{t}} \right) \tag{3.44}$$

Let's express the thickness of TGO by oxidation strain, taking into account eq. (3.39).

$$d^{ox}_{t} = d^{ox}_{0} \cdot e^{\varepsilon^{ox}_{t}} \tag{3.45}$$

The increase of TGO thickness can be formulated explicitly from eq. (3.42).

$$\Delta d^{ox} = d^{ox}_{t=t_{end}} - d^{ox}_{t=t_{end}-\Delta t} \tag{3.46}$$

Substituting the TGO thicknesses in Eq. 3.46 at the end and the beginning of the time step by Eq. 3.38 the following relation is obtained.

$$\Delta d^{ox} = \left(A_{ox} \cdot e^{-\frac{E_A}{R \cdot T}} \cdot t_{end}\right)^{n_{ox}} - \left(A_{ox} \cdot e^{-\frac{E_A}{R \cdot T}} \cdot (t_{end} - \Delta t)\right)^{n_{ox}} \tag{3.47}$$

Finally substituting Eq. (3.47) and using Eq. (3.45) into Eq. (3.44) we can express an increment of oxidation strain in a form, suitable for the implementation into HKS/ABAQUS.

$$\Delta \varepsilon^{ox} = \ln\left(1 + \frac{\left(A_{ox} \cdot e^{-\frac{E_A}{R \cdot T}} \cdot t_{end}\right)^{n_{ox}} - \left(A_{ox} \cdot e^{-\frac{E_A}{R \cdot T}} \cdot (t_{end} - \Delta t)\right)^{n_{ox}}}{d_0^{ox} \cdot e^{\varepsilon_t^{ox}}}\right) \tag{3.48}$$

#### 3.1.3.5 Elastic strain

It has been shown that addictive decomposition of strain required to calculate at any step plastic, creep and oxidation strain in order to obtain elastic strain. Knowing all strain componets the stiffness tensor is calculated and stresses are obtained.

## 3.2 Governing equations of solid body deformation.

To describe mathematically the problem of solid body deformation the following equations have to be written.

$$\sigma_{ij,j} + p_i = 0 \tag{3.49}$$

$$\varepsilon_{ij} = \frac{1}{2}\left(u_{i,j} + u_{j,i} + u_{i,k}u_{j,k}\right) \tag{3.50}$$

$$\sigma_{ij} = C_{ijkl}\varepsilon_{kl} \tag{3.51}$$

$$\sigma_{ij} = \sigma_{ji} \tag{3.52}$$

$$\sigma_{ij}n_j = \hat{t}_i \tag{3.53}$$

$$u_i = \hat{u}_i \tag{3.54}$$

Equation (3.49) represents the equilibrium between solid and body loads. Additionally, a geometrical relation between displacement and strain (3.50) and the constitutive relation (3.51) are defined . Finally boundary conditions namely, traction forces (3.53) and displacements conditions (3.54) are applied at the surface.

**It is difficult to solve analytically such a mechanical problem when complex structures are involved.** Therefore, different numerical techniques have been developed in order to calculate the stress response of a structure on various loading conditions. The finite element method [14; 35; 48; 54; 55] (FEM) is very well established in science and engineering. The biggest advantage of this method is a symmetric and sparse stiffness matrix. Although unsymmetrical stiffness comes from unsymmetrical constitute laws, such as nonassociated plastic flow. The FE-method bases on the principle of minimum potential energy and it is a so-called weak formulation. The strong formulation relates to an approximation of partial differential equations.

### 3.2.1 Total potential principle for linear mechanics.

It has been shown in a number of textbooks [14; 35; 54; 55] that the total potential is represented by equation

$$J(u_i) = \int_V \left(\frac{1}{2}\sigma_{ij}\varepsilon_{ij} - p_i u_i\right) dV - \int_{\partial V_\sigma} \hat{t_i} u_i d(\partial V) \tag{3.55}$$

$$= \int_V \left(\frac{1}{2} C_{ijkl} u_{i,j} u_{k,l} - p_i u_i\right) dV - \int_{\partial V_\sigma} \hat{t_i} u_i d(\partial V) \tag{3.56}$$

where: $\sigma_{ij}\varepsilon_{ij}$ - strain energy, $p_i u_i$ - internal work, $\hat{t_i} u_i$ - external work.

Stationarity of the functional requires that.

$$\delta J = \frac{\partial J}{\partial u_i} du_i = 0 \tag{3.57}$$

$$\delta J = \int_V (C_{ijkl} u_{i,j} \delta u_{k,l} - p_i \delta u_i) dV - \int_{\partial V_\sigma} \hat{t_i} \delta u_i d(\partial V) \tag{3.58}$$

$$= \int_V \left[ \left(C_{ijkl} u_{i,j} \delta u_k\right)_{,l} - \left(C_{ijkl} u_{i,j}\right)_{,l} \delta u_k - p_i \delta u_i \right] dV \tag{3.59}$$

$$- \int_{\partial V_\sigma} \hat{t_i} \delta u_i d(\partial V)$$

$$= \int_V \underbrace{C_{ijkl} \cdot u_{i,j}}_{\sigma_{kl}} n_l \delta u_k dV - \int_V \left[ \underbrace{\left(C_{ijkl} u_{i,j}\right)}_{\sigma_{ij}}{}_{,l} + p_i \right] \delta u_i dV \tag{3.60}$$

$$- \int_{\partial V_\sigma} \hat{t_i} \delta u_i d(\partial V)$$

$$= \int_V \left(\sigma_{kl} n_l - \hat{t_i}\right) \delta u_k d(\partial V) - \int_V \left(\sigma_{ij,l} + p_i\right) \delta u_i dV \tag{3.61}$$

From equation (3.61) the traction forces and equilibrium equation have been obtained. To derive a final set of FE equations the displacement field approximation has to be defined. It is difficult to propose a general form of displacement field approximation in the body. Therefore, structures can be divided by small volumes, which are called elements. Every element (Fig. 3.3) has a number of nodes where the displacement field is approximated.

A small strain for an element in the three dimensions Cartesian coordinate system can be represented as:

$$\begin{Bmatrix} \varepsilon_x \\ \varepsilon_y \\ \varepsilon_z \\ \gamma_{xy} \\ \gamma_{yz} \\ \gamma_{zx} \end{Bmatrix} = \underbrace{\begin{bmatrix} \frac{\partial}{\partial x} & 0 & 0 \\ 0 & \frac{\partial}{\partial x} & 0 \\ 0 & 0 & \frac{\partial}{\partial x} \\ \frac{\partial}{y} & \frac{\partial}{\partial x} & 0 \\ 0 & \frac{\partial}{\partial z} & \frac{\partial}{\partial y} \\ \frac{\partial}{\partial z} & 0 & \frac{\partial}{\partial x} \end{bmatrix}}_{G} \begin{Bmatrix} u \\ v \\ w \end{Bmatrix} \tag{3.62}$$

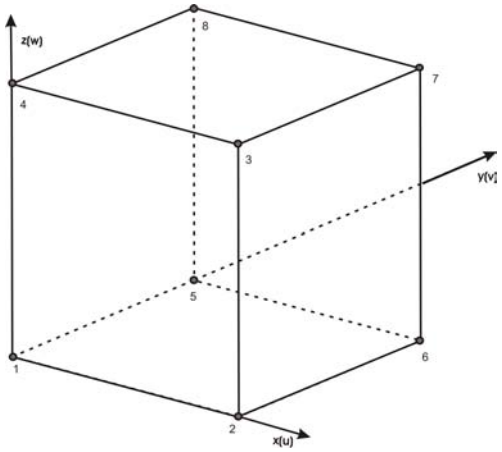


Figure 3.3: 8-node ”brick” element

where:

$$\mathbf{u} = \begin{Bmatrix} u \\ v \\ w \end{Bmatrix} = \begin{Bmatrix} \sum_{i=1}^{8} N_i q_i^x \\ \sum_{i=1}^{8} N_i q_i^y \\ \sum_{i=1}^{8} N_i q_i^z \end{Bmatrix} = \mathbf{Nq} \tag{3.63}$$

In the eq.( 3.63) the approximation was written for a three dimensional eight node element. Where $N_i$ is a shape function at node i and $q$ is the displacement at node i. Using an operator $G$ on function $u, v, w$ the strain matrix can be represented as:

$$\varepsilon = \underbrace{\begin{bmatrix} \frac{\partial N_1}{\partial x} & 0 & 0 & \frac{\partial N_2}{\partial x} & 0 & 0 & \dots \\ 0 & \frac{\partial N_1}{\partial x} & 0 & 0 & \frac{\partial N_2}{\partial x} & 0 & \dots \\ 0 & 0 & \frac{\partial N_1}{\partial x} & 0 & 0 & \frac{\partial N_2}{\partial x} & \dots \\ \frac{\partial N_1}{\partial x} & \frac{\partial N_1}{\partial y} & 0 & \frac{\partial N_2}{\partial x} & \frac{\partial N_2}{\partial y} & 0 & \dots \\ 0 & \frac{\partial N_1}{\partial z} & \frac{\partial N_1}{\partial y} & 0 & \frac{\partial N_2}{\partial z} & \frac{\partial N_2}{\partial y} & \dots \\ \frac{\partial N_1}{\partial z} & 0 & \frac{\partial N_1}{\partial x} & \frac{\partial N_2}{\partial z} & 0 & \frac{\partial N_2}{\partial x} & \dots \end{bmatrix}}_{\mathbf{B}} \cdot \mathbf{q} \tag{3.64}$$

$$\mathbf{q^T} = \{q_1^x, q_1^y, q_1^x, q_2^x, q_2^y, q_2^x, \dots, q_8^x, q_8^y, q_8^x\} \tag{3.65}$$

Substituting (3.64) and (3.63) into (3.55) gives (3.66). Additionally the additive of integration by elements has been taken in to account.

$$J(q) = \sum_{i=1}^{elements} \int_V \left( \frac{1}{2} \mathbf{q^t B^T C B q} - \mathbf{pNq} \right) dV - \sum_{i=1}^{elements} \int_{\partial V_\sigma} \hat{\mathbf{t}} \mathbf{N q} d(\partial V) \tag{3.66}$$

For a minimum of total potential energy the stiffness matrix is obtained:

$$\sum_{i=1}^{elements} \int_V (\mathbf{B^T C B}) dV \mathbf{q} = \sum_{i=1}^{elements} \int_V (\mathbf{pN}) dV + \sum_{i=1}^{elements} \int_{\partial V_\sigma} \hat{\mathbf{t}} \mathbf{N} d(\partial V) \tag{3.67}$$

where:

| | |
|---|---|
| $\mathbf{K} = \sum_{i=1}^{elements} \int_V (\mathbf{B^T C B}) dV$ | is the Stiffnes matrix |
| $\mathbf{F_B} = \sum_{i=1}^{elements} \int_V (\mathbf{pN}) dV$ | are body loads |
| $\mathbf{F}_\sigma = \sum_{i=1}^{elements} \int_{\partial V_\sigma} \hat{\mathbf{t}} \mathbf{N} d(\partial V)$ | are external loads |

Finally, equations of FEM can be written in the matrix -vector form (3.68).

$$\mathbf{K} \cdot \mathbf{q} = \mathbf{F_B} + \mathbf{F}_\sigma \tag{3.68}$$

FE generally represents an approximation of $C^0$ continuity of the displacement field. The definition of strain is related to the gradient deformation tensor $F$. Therefore, standards FE-method utilize discontinuity in strain and stress fields.

# Modeling approach and materials data

The present chapter gives a review of the methodology for modeling of an experimental setup with a thermal barrier coating system and the materials data. Some simplifications have been assumed in order to enable computation in reasonable time. However, to provide a realistic response the complexity of materials behavior such as nonlinear time dependent response has been considered. The local geometry of the BC/ TBC interface layer plays a major role. Therefore different interface geometries have been considered for the numerical study.

## 4.1 Geometry of specimen

The sample considered as experimental counterpart for the numerical simulation consists of a hollow cylinder. The real geometry is shown in Fig. 4.1. On the surface of the cylinder a bond coat was applied and on top of it the thermal barrier coating. Between those two coatings an alumina oxide layer grows during operation at high temperature. The TGO layer will referred to in the following as interface layer. The geometry of the interface is very complex. Sinusoidal, semicircular or other geometrical functions like bspline, NURBS, etc can approximate the undulations of the interface. The region of interest is at the middle part of the experimental test piece with a length of

Figure 4.1: Experimental TMF sample.

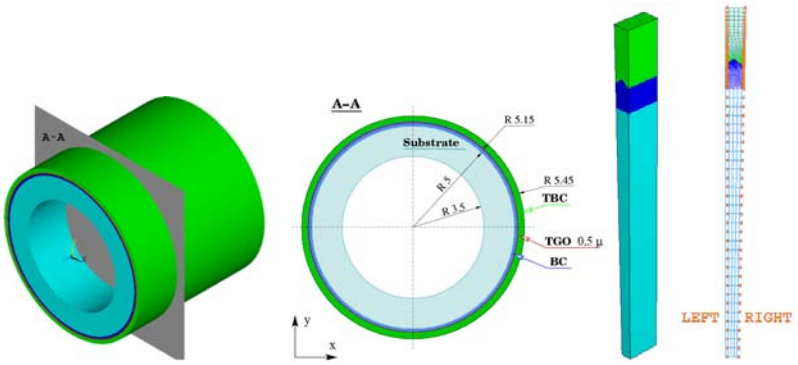


Figure 4.2: Schematic drawing of the specimen geometry which was used for the simulations.

20 mm. Fig. 4.2 shows a cross section and the geometrical dimensions. Specimens have been exposed at high temperature with a loading profile equivalent to operation conditions. The experimental setup is schematically shown in Fig. 4.3.

Four independent variables $\bar{X} = X(x, y, z, t)$ describe the process of deformation in the experimental system. Where $x$, $y$, $z$ are positions in Cartesian coordinate system and $t$ is the time variable. It can be concluded that a minimum of two dimensions are required, such as radial position and time. To describe the interface shape it is not possible by one variable in the Cartesian coordinate system. Therefore, in this thesis the 2D problem is not considered. A 3D problem has been chosen, where two variables are positions of a point in plane and the third one is time. A 4D problem could be considered, but it will increase the number of elements drastically. This happens, because the interface layer has to be modeled with a fine mesh to give a proper response of this layer.

## 4.2 Mesh

To generate a fine mesh on this layer, four elements over the thickness have been set. It has to be mentioned that the initial thickness of this layer is 0.5 $\mu m$ as it is shown in Fig. 4.2. The thickness of bond coat and thermal barrier coating is high compared to the interface layer (oxide).

As the experimental specimen is axis-symmetric it can be modeled in plane **A-A** with periodic shape shown in Fig. 4.4 using four nodes elements with general plane strain approximation and reduced integration (CPEG4R [1]). Amplitude and wavelength can parameterize this interface. By the choice of an analytical function like sinus, semicircle and ellipse the 4 different models have been generated. In Tab. 4.1

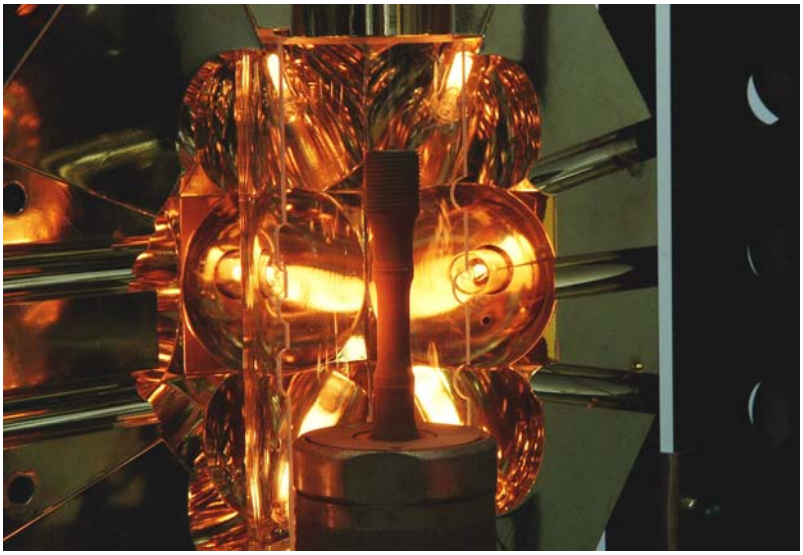

Figure 4.3: Experimental setup.

the parameterization is given. The mesh is shown in Figs. 4.4(a) - 4.4(d).

Reduced integration has been chosen, because the interface layer is under a high bending and elements are significantly elongated. With a combination of plastic and viscoplastic material behavior a locking[1] problem is generated. To avoid this one can use incompatible mode elements, but this only works when the corner angles of the elements are close to $90^o[deg]$. Reduced integration has other advantages. It requires less storage space than in full integration and the number of numerical operations during calculation is lower as well.

Table 4.1: Interface parameterization with an amplitude of 15 $\mu m$

| wavelength [$\mu m$] | sinusoidal | semicircle | ellipse |
|---|---|---|---|
| 60 | ♢ | ♢ | |
| 90 | ♢ | | ♢ |

## 4.3 Material data

Nonlinear behavior and large deformation are considered. The base material (CMSX-4) is mostly considered as a pure elastic material, all others as elastic, ideal plastic (Tab. 4.6

[1] the stiffness of an element is overestimated during numerical integration

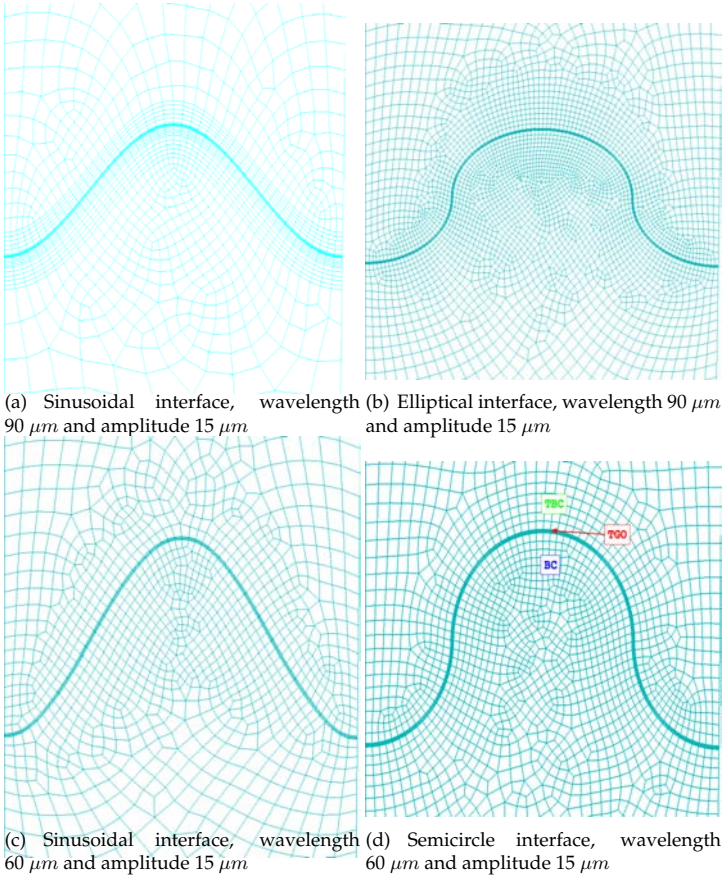


(a) Sinusoidal interface, wavelength 90 $\mu m$ and amplitude 15 $\mu m$

(b) Elliptical interface, wavelength 90 $\mu m$ and amplitude 15 $\mu m$

(c) Sinusoidal interface, wavelength 60 $\mu m$ and amplitude 15 $\mu m$

(d) Semicircle interface, wavelength 60 $\mu m$ and amplitude 15 $\mu m$

Figure 4.4: Segment of periodic structure

and Tab. 4.7) and viscous materials (including creep and stress relaxation). The material properties have been considered as temperature dependent and are listed in Tab. 4.2, Tab. 4.3, Tab. 4.4 and Tab. 4.5.

A temperature of $200^o\ C$ was selected as the value at which the TBC composite is initially stress free. It matches approximately with the process temperature for air plasma spraying. In the case of BC and TBC primary and secondary creep stages were taken into account (Tab. 4.9 and Tab. 4.10). The creep data were experimentally determined by compression creep tests with stand-alone coatings (TBC, BC) and shear deformation experiments on TBC composites [24; 25; 36; 37; 50]. The data were implemented using Eq. 3.33. For the TGO layer with grain size below 1 $\mu m$ secondary Norton creep (4.69) properties have been assumed (Tab. 4.11).

$$\dot{\varepsilon_{cr}} = A \cdot \sigma^n \tag{4.69}$$

Growing of the alumina scale at high temperature is simulated using the swelling option in ABAQUS. The oxidation process is considered to happen in the temperature range $950^o$ C to $1050^o$ C (Tab. 4.12). It is modeled as an orthotropic swelling strain of the TGO. Because the FE-Package Abaqus divides the orthotropic swelling strain by three, the values at the input file were scaled by the same factor. Two cases with and without oxidation in lateral direction have been studied. In the case of lateral oxidation mainly 5% of TGO thickness increase have been chosen. In the third direction (perpendicular to plane elements) the oxidation kinetics has always been set to zero.

## 4.4 Load and Boundary conditions

### 4.4.1 Thermal Loads

The load cycle consisted of thermal cycling and high temperature exposition (cyclic oxidation), which is represented in Fig. 4.5. It consisted of four steps. First, heating from $20^o$ C to $1050^o$ C in 103 s, followed by a dwell-time at $1050^o$ C for 7200 s. Cooling from $1050^o$ C to $20^o$ C took also 103 s. As a last step a holding time at low temperature ($20^o$ C) of 900s was introduced.

### 4.4.2 Displacement conditions

Regarding a cylindrical co-ordinate system, the nodes lying on the edges of the segment (Fig. 4.2: left, right) have been constrained under 2'nd degree of freedom (DOF). Constrain equations have been used additionally in order to gain a homogeneous[1] radial displacement at the right and left side of the selected segment, respectively. As general plain strain elements use extra node, all DOF in this additional node were constrained. This is equal to plain strain approximation. If the displacement in the direction of the thickness will be unconstrained the stress level would decrease due to a possible deformation in the 3'rd direction.

[1] periodic condition of the unit cell


Figure 4.5: Thermal cycle used in FE-simulation

Table 4.2: Elastic properties of **CMSX-4**

| $T[^oC]$ | E [GPa] | $\nu$ | $\hat{\alpha}[\frac{1}{^oC}]$ |
|---|---|---|---|
| 20 | 130.70 | 3.630E-01 | 1.17E-05 |
| 50 | 128.98 | 3.633E-01 | 1.18E-05 |
| 100 | 126.13 | 3.639E-01 | 1.19E-05 |
| 150 | 123.32 | 3.646E-01 | 1.19E-05 |
| 200 | 120.55 | 3.653E-01 | 1.20E-05 |
| 250 | 117.81 | 3.661E-01 | 1.21E-05 |
| 300 | 115.11 | 3.670E-01 | 1.22E-05 |
| 350 | 112.44 | 3.679E-01 | 1.23E-05 |
| 400 | 109.80 | 3.688E-01 | 1.24E-05 |
| 450 | 107.20 | 3.699E-01 | 1.25E-05 |
| 500 | 104.64 | 3.710E-01 | 1.25E-05 |
| 550 | 102.11 | 3.721E-01 | 1.26E-05 |
| 600 | 99.62 | 3.733E-01 | 1.27E-05 |
| 650 | 97.17 | 3.746E-01 | 1.28E-05 |
| 700 | 94.74 | 3.759E-01 | 1.30E-05 |
| 750 | 92.36 | 3.773E-01 | 1.31E-05 |
| 800 | 90.01 | 3.788E-01 | 1.32E-05 |
| 850 | 87.69 | 3.803E-01 | 1.33E-05 |
| 900 | 85.41 | 3.818E-01 | 1.34E-05 |
| 950 | 83.17 | 3.835E-01 | 1.35E-05 |
| 1000 | 80.96 | 3.852E-01 | 1.36E-05 |
| 1050 | 78.78 | 3.869E-01 | 1.38E-05 |
| 1100 | 76.64 | 3.887E-01 | 1.39E-05 |

Table 4.3: Elastic properties of **BC**

| $T[^oC]$ | E [MPa] | $\nu$ | $\hat{\alpha}[\frac{1}{^oC}]$ |
|---|---|---|---|
| 20 | 1.524E+05 | 3.11E-01 | 1.23E-05 |
| 50 | 1.511E+05 | 3.12E-01 | 1.26E-05 |
| 100 | 1.486E+05 | 3.15E-01 | 1.31E-05 |
| 150 | 1.459E+05 | 3.18E-01 | 1.34E-05 |
| 200 | 1.433E+05 | 3.20E-01 | 1.38E-05 |
| 250 | 1.411E+05 | 3.23E-01 | 1.40E-05 |
| 300 | 1.394E+05 | 3.25E-01 | 1.43E-05 |
| 350 | 1.381E+05 | 3.27E-01 | 1.45E-05 |
| 400 | 1.371E+05 | 3.30E-01 | 1.47E-05 |
| 450 | 1.364E+05 | 3.32E-01 | 1.49E-05 |
| 500 | 1.356E+05 | 3.34E-01 | 1.51E-05 |
| 550 | 1.347E+05 | 3.36E-01 | 1.52E-05 |
| 600 | 1.333E+05 | 3.38E-01 | 1.54E-05 |
| 650 | 1.311E+05 | 3.40E-01 | 1.57E-05 |
| 700 | 1.278E+05 | 3.42E-01 | 1.59E-05 |
| 750 | 1.233E+05 | 3.43E-01 | 1.62E-05 |
| 800 | 1.172E+05 | 3.45E-01 | 1.66E-05 |
| 850 | 1.094E+05 | 3.47E-01 | 1.70E-05 |
| 900 | 9.964E+04 | 3.48E-01 | 1.74E-05 |
| 950 | 8.791E+04 | 3.50E-01 | 1.80E-05 |
| 1000 | 7.416E+04 | 3.51E-01 | 1.86E-05 |
| 1050 | 5.849E+04 | 3.52E-01 | 1.94E-05 |
| 1100 | 4.107E+04 | 3.54E-01 | 2.02E-05 |

Table 4.4: Elastic properties of **TGO**

| $T[^oC]$ | E [MPa] | $\nu$ | $\hat{\alpha}[\frac{1}{^oC}]$ |
|---|---|---|---|
| 20 | 4.00E+05 | 0.23 | 7.13E-06 |
| 50 | | | 7.19E-06 |
| 100 | | | 7.28E-06 |
| 150 | | | 7.37E-06 |
| 200 | 3.90E+05 | 0.23 | 7.47E-06 |
| 250 | | | 7.56E-06 |
| 300 | | | 7.65E-06 |
| 350 | | | 7.74E-06 |
| 400 | 3.80E+05 | 0.24 | 7.82E-06 |
| 450 | | | 7.91E-06 |
| 500 | | | 7.99E-06 |
| 550 | | | 8.07E-06 |
| 600 | 3.70E+05 | 0.24 | 8.15E-06 |
| 650 | | | 8.23E-06 |
| 700 | | | 8.31E-06 |
| 750 | | | 8.39E-06 |
| 800 | 3.55E+05 | 0.25 | 8.46E-06 |
| 850 | | | 8.54E-06 |
| 900 | | | 8.61E-06 |
| 950 | | | 8.68E-06 |
| 1000 | 3.25E+05 | 0.25 | 8.75E-06 |
| 1050 | | | 8.82E-06 |
| 1100 | 3.20E+05 | 0.25 | 8.88E-06 |

Table 4.5: Elastic properties of **TBC**

| $T[^oC]$ | E [MPa] | $\nu$ | $\hat{\alpha}[\frac{1}{^oC}]$ |
|---|---|---|---|
| 20 | 17.5E+05 | 0.2 | 1.0149E-05 |
| 1100 | 11.23E+03 | 0.2 | 1.0344E-05 |

Table 4.6: Plastic properties of **BC**

| $T[^oC]$ | $\sigma^Y$ [MPa] |
|---|---|
| 20 | 868 |
| 500 | 807 |
| 600 | 562 |
| 700 | 321 |
| 750 | 265 |
| 850 | 117 |
| 950 | 66 |
| 1050 | 38 |

Table 4.7: Plastic properties of **TGO**

| $T[^oC]$ | $\sigma^Y$ [MPa] |
|---|---|
| 20 | 8000 |
| 500 | 8000 |
| 1000 | 300 |
| 1100 | 300 |

Table 4.8: **Ni-based Superalloy** Norton creep properties [40]

| $T[^oC]$ | A $[\frac{MPa^{-n}}{s}]$ | n |
|---|---|---|
| 10 | 4.85E-36 | 1 |
| 1200 | 2.25E-9 | 3 |

Table 4.9: **BC** creep properties [36; 37]

| $T[^oC]$ | $A'[\frac{MPa^{-n}}{s}]$ | $n'$ | $\varepsilon'_{cr}$ | A$[\frac{MPa^{-n}}{s}]$ | n |
|---|---|---|---|---|---|
| 750 | 1.25E-12 | 4.5 | 0.24 | 1.25E-14 | 4.5 |
| 850 | 1.40E-09 | 3.8 | 0.23 | 1.40E-11 | 3.8 |
| 950 | 2.30E-07 | 3.1 | 0.22 | 2.30E-09 | 3.1 |
| 1050 | 9.50E-06 | 2.55 | 0.21 | 9.50E-08 | 2.55 |

Table 4.10: **TBC** creep properties [24; 25; 50]

| $T[^oC]$ | $A'[\frac{MPa^{-n}}{s}]$ | $n'$ | $\varepsilon'_{cr}$ | A$[\frac{MPa^{-n}}{s}]$ | n |
|---|---|---|---|---|---|
| 750 | 2.20E-18 | 4.5 | 0.05 | 2.00E-22 | 4.5 |
| 850 | 2.00E-16 | 4.32 | 0.08 | 2.00E-20 | 4.32 |
| 950 | 9.00E-15 | 4.15 | 0.12 | 3.00E-18 | 4.15 |
| 1050 | 3.02E-13 | 3.98 | 0.18 | 3.77E-16 | 3.98 |
| 1150 | 4.80E-12 | 3.8 | 0.25 | 4.80E-14 | 3.8 |

Table 4.11: **TGO** Norton creep properties [43]

| $T[^oC]$ | A$[\frac{MPa^{-n}}{s}]$ | n |
|---|---|---|
| 750 | 7.3E-4 | 1 |
| 1050 | 7.3E-4 | 1 |

Table 4.12: Parameters for oxidation kinetic [15]

| $T[^oC]$ | $A^o$ | $n$ | $E_\alpha$ | R |
|---|---|---|---|---|
| 950 | 1.57E-15 | 0.33 | 18000 | 8.314 |
| 1000 | | 0.325 | | |
| 1050 | | 0.3225 | | |

Table 4.13: Cohesive **BC/TGO** zone properties of damage evolution energy type with mixed mode behavior with the Benzeggagh-Kenane fracture criterion power law ([1; 5; 6]) and the exponential function of softening

Maximal damage = 0.998

| Thickness of cohesive layer $[\mu m]$ | Penalty factor$[\frac{N}{mm}]$ | $\sigma^c[MPa]$ | $\tau^c[MPa]$ | $G_I^c[\frac{J}{m^2}]$ | $G_{II}^c[\frac{J}{m^2}]$ | B-K power factor |
|---|---|---|---|---|---|---|
| 0.0 | $10^8$ | 600 | 1200 | 20 | 40 | 1.45 |

# Results

In this chapter the investigation by successive and stepwise consideration of the parameters, continuous TGO growth, lateral TGO growth, BC ideal plastic, TGO ideal plastic, BC creep, TBC creep and TGO creep are presented. All presented results comprise the stress values at room temperature after 1st, 51st, 101st and 161st cycle and are radial stresses. In all studied cases under thermal cycling with dwell-time the formation of aluminum oxide was considered. The thickness increased continuously (except the parametric study) at high temperature following the experimentally determined kinetics up to 5.7 $\mu m$. This process considerably increased the local stresses at the interface region. Additionally a long calculation consisting of 621 cycles has been simulated resulting in 8.6 $\mu m$ of TGO thickness.

## 5.1 Basic influence of material properties on stress response and stress evolution

Here, systematic studies of the influence of different material properties are presented and are itemized with capital latin letters as shown in Tab. 5.1.

### 5.1.1 Influence of TGO growth stresses (case A)

High temperature diffusion of aluminum together with diffusion of oxygen to the BC/TBC interface results in the formation of an oxide-layer (TGO). The formation of alumina ($Al_2O_3$) involves an expansion of the crystallographic volume [7]. This volume change contributes to the stress development in TBCs.

Moreover, the layers in TBCs have different material properties. The interactions of adjacent layers introduce local stresses. The stress levels and its field distribution are a function of TGO thickness.

#### 5.1.1.1 Elastic calculation with parametric TGO thickness values

When the system is purely elastic and oxidation is taken into account using different, but not time dependent thickness values, stress response is independent of time. The stress state at RT, shown in Fig. 5.1 is thus determined by mismatch stresses after cooling from a temperature where the system is stress free ($200^oC$) to ambient temperature ($20^oC$). The stress field of a sinusoidal interface with a TGO thickness of

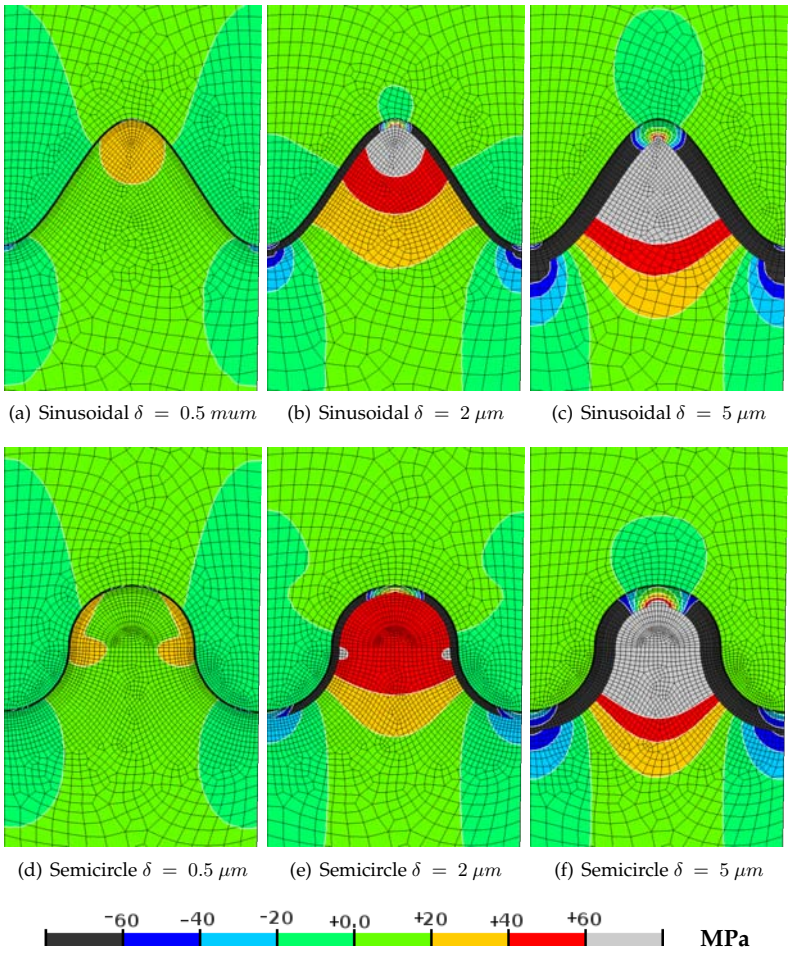


(a) Sinusoidal $\delta = 0.5\ mum$ (b) Sinusoidal $\delta = 2\ \mu m$ (c) Sinusoidal $\delta = 5\ \mu m$

(d) Semicircle $\delta = 0.5\ \mu m$ (e) Semicircle $\delta = 2\ \mu m$ (f) Semicircle $\delta = 5\ \mu m$

Figure 5.1: Radial stress distribution at the interface at room temperature. Fully elastic simulations with 3 different TGO thickness values ($\delta$) and two different shapes of the interface. All stresses are in MPa.

Table 5.1: Assignment of different inelastic material properties used for different FE simulations.

| Case | Creep | Plastic | Comments |
|---|---|---|---|
| A | | | Parametric studies of TGO thickness values |
| B | | | Out-of-plane continuous oxidation |
| C | | | Out-of-plane continuous oxidation including 5% of lateral oxidation |
| D | | BC | Out-of-plane continuous oxidation including 5% of lateral oxidation |
| E | | TGO | Out-of-plane continuous oxidation including 5% of lateral oxidation |
| F | | BC and TGO | Out-of-plane continuous oxidation including 5% of lateral oxidation |
| G | BC | TGO | Out-of-plane continuous oxidation including 5% of lateral oxidation |
| H | BC | BC and TGO | Out-of-plane continuous oxidation including 5% of lateral oxidation |
| I | TBC | BC and TGO | Out-of-plane continuous oxidation including 5% of lateral oxidation |
| J | BC and TBC | BC and TGO | Out-of-plane continuous oxidation including 5% of lateral oxidation (Reference case) |

$0.5\mu m$ is shown in Fig. 5.1(a) . The stress response with a TGO thickness of $2\mu m$ is presented in Fig. 5.1(b), and with $5\mu m$ in Fig. 5.1(c). The stress response with 3 different TGO thickness values was also performed on a model with semicircle interface (Figs. 5.1(d) - 5.1(f)). To better visualize the local stress distribution in the TBC, three paths have been chosen along which radial stresses would be shown in more detail (Fig. 5.3, Fig. 5.4 and Fig. 5.5). The locations of the paths (one in TBC, one in TGO and one in BC) are shown schematically in Fig. 5.2.

Fig. 5.3 shows the stress distribution along the BC path. The left part presents results for the sinusoidal interface, while in the right part results for the semicircle interface are presented, for all three different TGO thickness values. Comparing these stresses one can see that the absolute values are higher for the sinusoidal case. The radial stress distribution along the TGO path is presented in Fig. 5.4 and Fig. 5.5 gives the radial stresses along the TBC path respectively. The stress values in the TBC path at the peak (Fig. 5.5 left) decreased faster in case of sinusoidal interface than for the semicircle shape (Fig. 5.5 right). The parametric study confirmed previous findings, that TGO growth acts as a driving force of stress transition at valleys of TBC from compressive to tensile (Fig. 5.5) and from tensile to compressive above the peak asperity in the TBC. However, the transition from compressive to tensile stresses in the valley region occurs at a smaller TGO thickness for the semicircle shape compared to the sinusoidal shape. Moreover, the tensile stresses are generally smaller for the semicircle shape. In contrast to the valley region, above asperity peaks the stresses

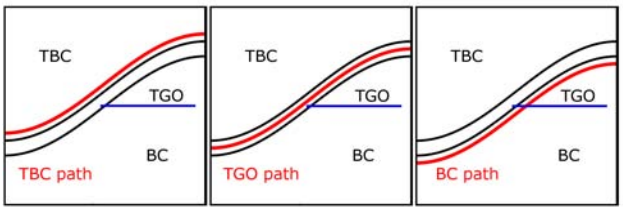


Figure 5.2: Path lines for radial stresses visualization.

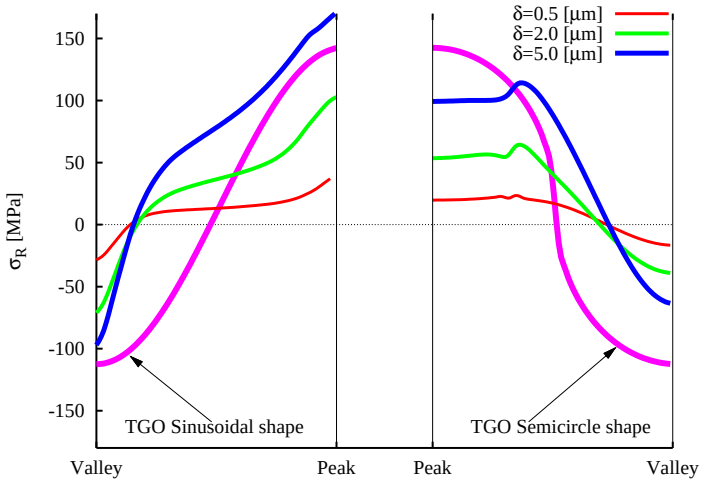


Figure 5.3: Radial Stress distribution along BC path from valley to the peak of the TGO interface with three different TGO thickness values and two diverse shapes of the interface BC/TBC.

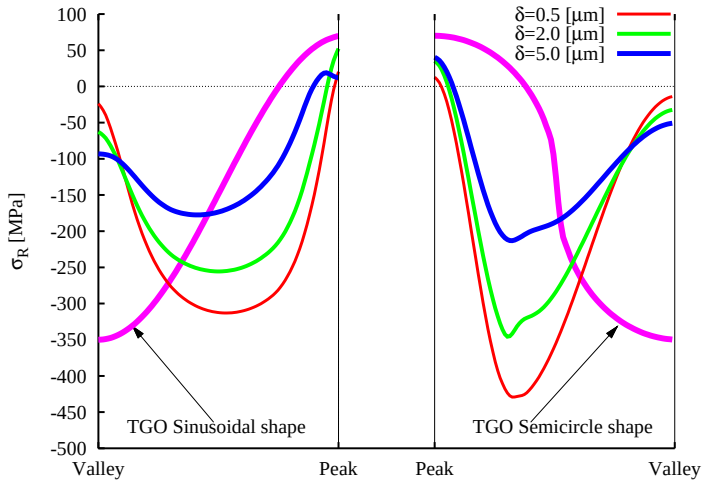


Figure 5.4: Radial Stress distribution along TGO path from valley to the peak of the TGO interface with three different TGO thickness values and two diverse shapes of the interface BC/TBC.

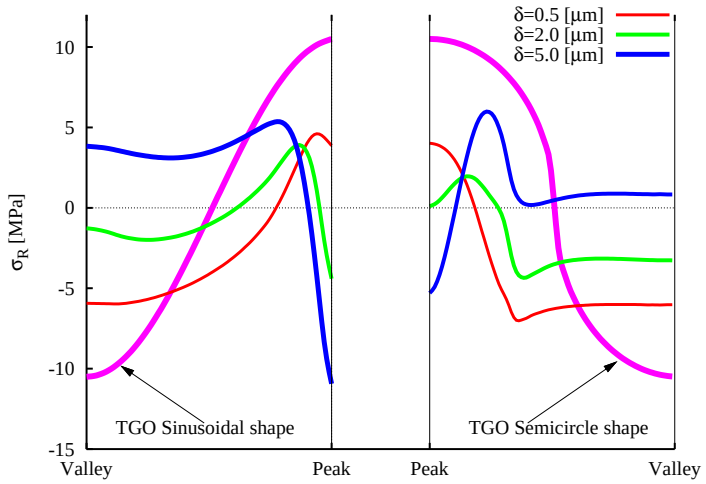


Figure 5.5: Radial Stress distribution along TBC path from valley to the peak of the TGO interface with three different TGO thickness values and two diverse shapes of the interface BC/TBC.

change from tensile to compressive when the TGO thickness is changed from 0.5 $\mu m$ to 5 $\mu m$. The result is also in agreement with early published results [12]. For the reason of a more severe stress state, the calculations in the following chapters will be limited to the sinusoidal interface. The maximum stresses for different thickness values are located at the peak of BC ( Fig. 5.1 and Fig. 5.3).

#### 5.1.1.2 Elastic calculation with continuous TGO growth without lateral oxidation (case B)

Oxidation is an irreversible process governed by temperature and time. In the following; thermal cycling is simulated as described in chapter 4.4.1 and TGO growth is introduced according to chapter 3.1.3.4. Thickening of the TGO layer introduces very high tensile and compressive stresses in TBCs. In Fig. 5.6 one can notice that an continuous increase of the TGO thickness is associated with a rearrangement of the stress field in TBCs in comparison with the parametric study (Fig. 5.1). In order to better follow the stress development, the limits of stress zones were defined, one in black under compression and one in gray tone showing tensile zone. Only the areas of moderate stresses between -60 and +60 MPa are colored. Here, the developments of compressive stress zones have been observed at the peak region of BC. This compressive stress zone was formed at an early stage of thermal cycling (Fig. 5.6(a)) with stresses values below -60 MPa. Additionally at the valleys of BC two small compressive stress zones were formed (Fig. 5.6(a)). An enlargement of this compressive zone at the peak in BC has been observed during 100 cycles (Figs. 5.6(b) - 5.6(c)). Later in the last 60 cycles, this stress zone has again decreased (Figs. 5.6(d)). Within the TBC, a tensile zone was present already after the 1st cycle (Figs. 5.6(a)). It was located above the compressive zone peak in the TBC. The valleys were under compression (Fig. 5.6(a)). As time increased the compressive and tensile zones in TBC were getting bigger (Figs. 5.6(b) - 5.6(d)). In other words, the areas of stresses between 60 MPa and -60 MPa became very narrow, 5 $\mu m$ and even less. Therefore, large stress gradients exist. Within the TGO, the oxidation process introduces a large increase of volume. As a response, the TGO layer was exposed to tensile stresses from middle part to almost peak region (Fig. 5.6(d)). The remaining parts of TGO were under compressive stresses Fig. 5.6. After 161 cycles a maximal tensile stress of 27890 MPa was located in the TGO layer at an off-peak region. Maximal compressive stress of -31080 MPa was found within the TGO layer as indicated in Fig. 5.6.

#### 5.1.1.3 Elastic calculation with continuous TGO growth with lateral growth (case C)

In the last section only an increase of TGO volume normal to the interface was considered. Here, the influence of lateral oxidation on the stress response is studied additionally. A length increase of 5% of the thickness increase was taken into account. All other parameters remained unchanged. Comparing Fig. 5.7 with Fig. 5.6 a change of the stress zones is indicated.

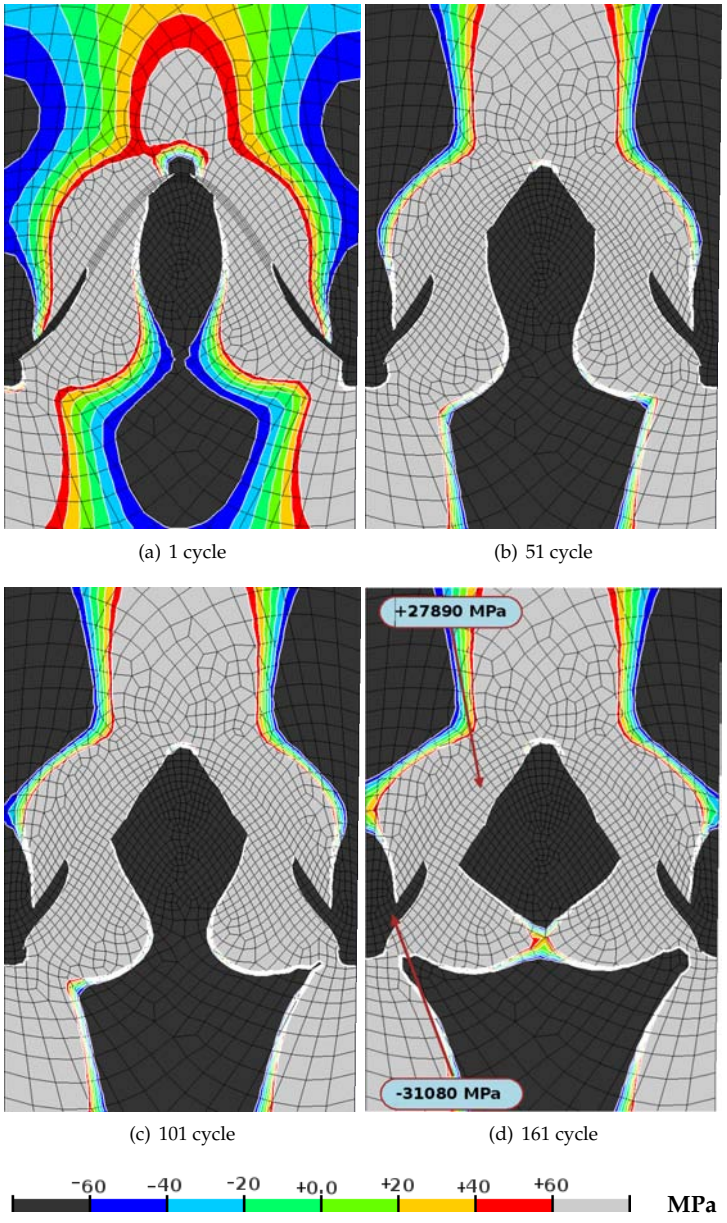


(a) 1 cycle (b) 51 cycle

(c) 101 cycle (d) 161 cycle

Figure 5.6: Development of radial stress distribution at the interface with continuous oxidation after cooling to RT at selected cycle numbers. The TGO thickness increased from $0.5\mu m$ at the first cycle to $5.7\mu m$ after 161 cycles. All stresses are displayed in MPa.

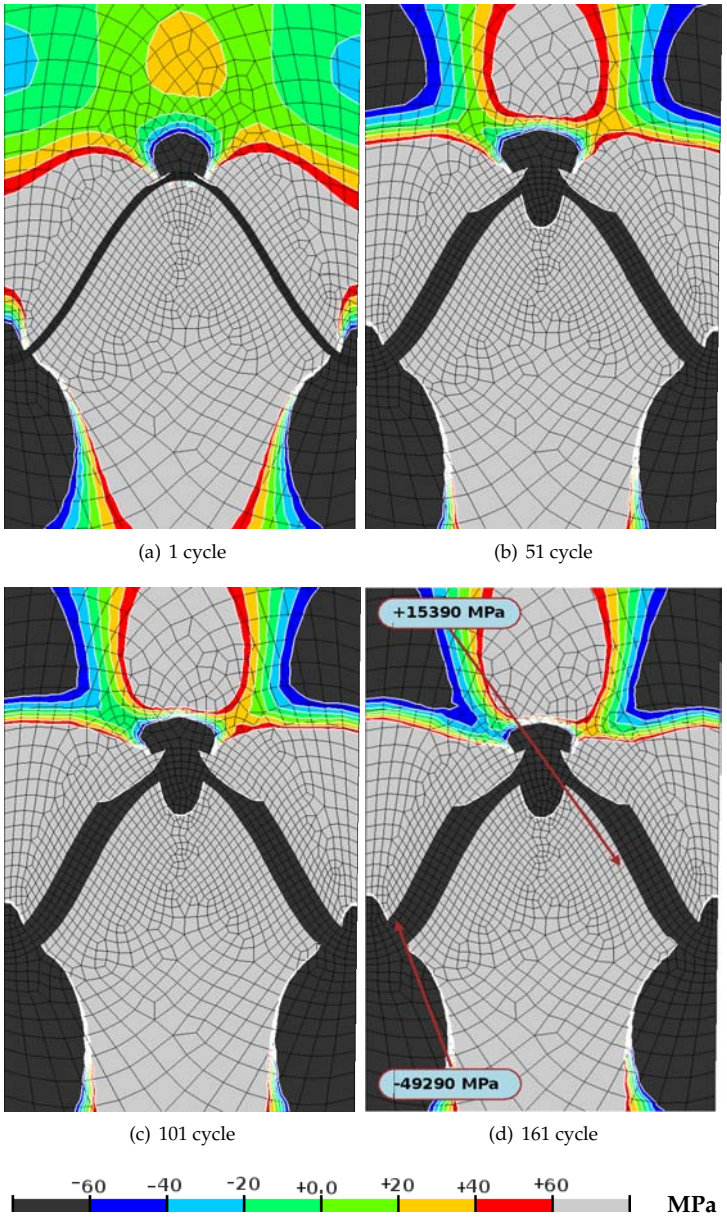


(a) 1 cycle (b) 51 cycle

(c) 101 cycle (d) 161 cycle

Figure 5.7: Radial stress distribution after cooling to RT at the interface with continuous oxidation, considering additionally (5%) lateral oxidation. The TGO thickness increased from $0.5\mu m$ at the first cycle to $5.7\mu m$ after 161 cycles. All stresses are in MPa.

After the first cycle a tensile stress zone was localized at the peak of the bond coat (Fig. 5.7(a)). However the valleys were occupied by compressive stresses Fig. 5.7(a). After the 51st cycle the tensile stresses at the peak of BC switched to compressive stresses Fig. 5.7(b). During cycling the compressive and tensile stress values increased. Moreover large stress gradients were formed.

One can note that the TGO layer was almost completely under compressive stresses, after the first cycle Fig. 5.7(a). However, very small off-peak regions had small tensile zones. The consequence of thickening and lengthening of oxide layer was an expansion of these tensile zones at off-peak regions Figs. 5.7(b) - 5.7(d).

The off-peak and above valley regions within the TBC were under tensile stresses revealing continuous tensile paths to the boundaries of the unit cell. Moreover five compressive stress zones were obtained in the TBC, namely at valleys, at the peak region and above the tensile zones at valleys Fig. 5.7(a). Major changes during cycling in the TBC layer were found above the peak region and above valleys. Above the peak in TBC a tensile zone was created (Fig. 5.7(b)). During the following 101 cycles all local stress zones were expanded, resulting in large stress gradients (Fig. 5.7(d)).

The increase of the TGO length introduced a continuous tensile path into the TBC layer from off-peak region to the boundaries of the unit cell Fig. 5.7(d). The presence of tensile stresses across the thickness of the TGO layer was not observed. Only two tensile zones were obtained at off-peak regions (Fig. 5.7(d)).

Major changes can be noted in the BC layer. There, the BC peak was under tensile stresses except the small tip region (Fig. 5.7(d)). In the case without lateral oxidation the peak was fully under compressive stresses (Fig. 5.6(d)). Moreover, lateral oxidation slightly increased the amplitude of the interface profile.

Based on the parametric study in comparison with continuous (with and without lateral) oxidation we can conclude that parametric study does not reflect the behavior of a real structure under continuous oxidation conditions. Moreover, the two cases with continuous oxidation lead principally to unrealistically high stresses in all three materials. However it was shown that not only is continuous out-of-plane oxidation important, but also lateral oxidation plays an important role and can not be neglected.

### 5.1.2 Influence of BC plasticity on elastic TBCs including continuous oxidation (case D)

As shown above, an elastic TBC system would generate huge and unrealistic stresses in BC, TGO and TBC. As these high stresses would lead to an immediate failure of the component, the structure has to somehow decrease them, for instance by plastic deformation. As a first non fully elastic calculation, only BC plasticity was considered, as described in chapter 4.3. All other parameters remained unchanged.

In Fig. 5.8 the stresses in radial direction are shown in the vicinity of the oxide layer (TGO). The stresses have been redistributed due to the plastic deformation of BC. We can notice that the maximum tensile stress increased compared to 5.1.1.3 (elastic case) but the maximum compressive stress decreased. In both cases the values are indicated in Fig. 5.7(d) and Fig. 5.8(d). The maximum tensile stress moved from the middle region in the BC to an off-peak region of the TGO close to the TBC layer. The minimum stress did not move to a different layer but shifted to the off-peak region close to the BC layer. Major changes were obtained in the BC layer. A tensile stress zone was located in the BC at the tip of asperity. The valleys of BC were occupied by compressive stresses (Fig. 5.8(a)). The evolution of the stress field in BC during cycling is shown in Fig. 5.8. The tensile stresses zone with stresses above 60 MPa expanded slightly in time. Moreover the compressive stress zone also expanded. However the stress gradients in BC were significantly smaller than in the previous calculation.

The TGO layer has developed tensile zones at off-valley regions close to the BC and at off-peak regions close to the TBC. Other parts of TGO were under compressive stresses (Fig. 5.8). The plastic deformation of the BC influenced also stresses in the TBC layer. The valleys in TBC at the beginning were occupied by tensile stresses. Only the peak of the TBC was under compression (Fig. 5.8(a)). However during cycling two compressive stress zones developed at valleys as shown in Fig. 5.8(b). Fig. 5.8(d) shows the distribution of radial stresses after the 161st cycle which indicates a further expansion of the tensile and compressive zones in TBC. This expansion, like in previous cases, created huge stress gradients.

The concentration of tensile stresses at the tip of the BC due to its plastic behavior reflects the results of experimental investigations, that the failure crack path is located partly in the TGO and partly in the TBC. Moreover, the stress conversion from tensile to compressive at the tip of the BC was obtained in the purely elastic case, but in the case of BC plastic behavior it was not observed (Fig. 5.7(d)). Further, the continuous tensile path in TBC from off-peak to the boundary of the unit cell was more pronounced and included a larger area (Fig 5.8(d)) than in the elastic case (Fig 5.7(d)).

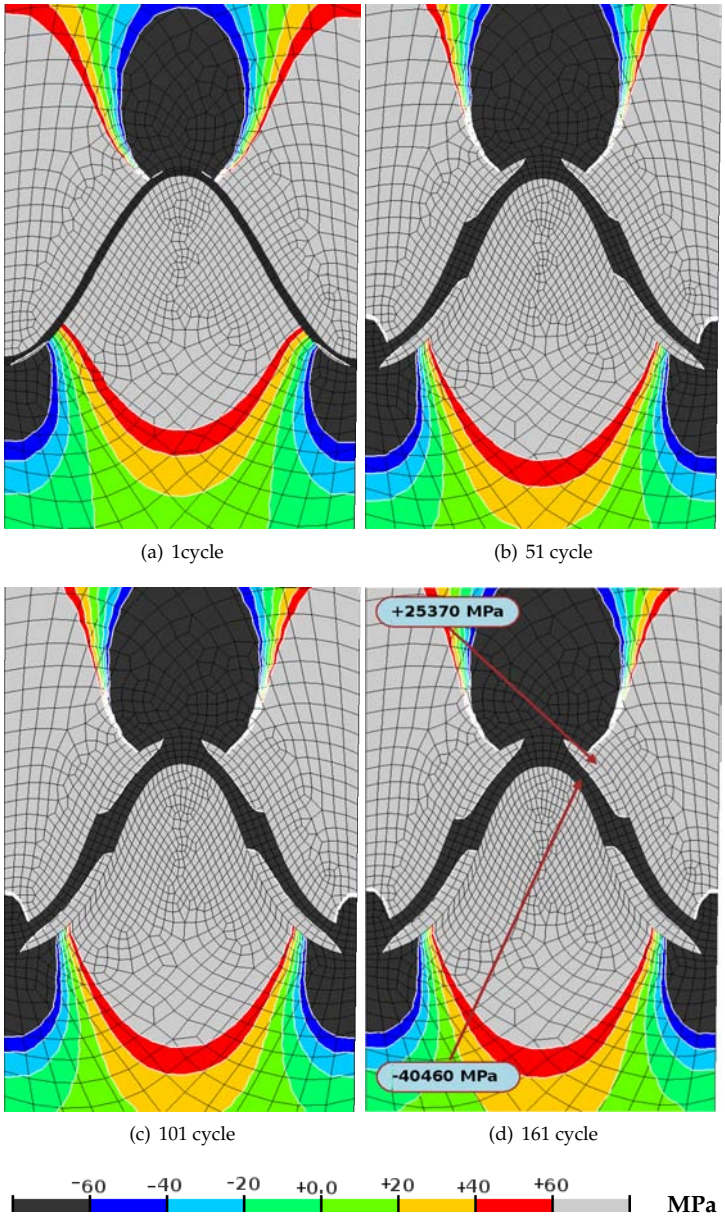


(a) 1cycle (b) 51 cycle

(c) 101 cycle (d) 161 cycle

Figure 5.8: Radial stress distribution at the interface with continuous oxidation, including 5% lateral oxidation and BC plasticity.

### 5.1.3 Influence of TGO plasticity on elastic TBCs including continuous oxidation (case E)

As the oxide layer is growing, its material properties have presumably a bigger impact on stress development in TBCs. Ideal plastic behavior of the oxide was assumed. All other materials were purely elastic and the remaining parameters were identical with previous calculations. As the growing oxide introduced huge stresses plastic deformation took place rather early. In Fig. 5.9 the contour plot of radial stresses is shown. In the TBC layer tensile stresses were present at valleys and above the peak. These tensile zones were separated by compressive zones located above the valleys (from boundaries of the unit cell to off-peak regions Figs. 5.9(b) - 5.9(d)).

After 1st cycle (Fig. 5.9(a)) mostly compressive stresses were obtained in the TGO layer. Only peak and valleys were under tensile stresses. During thermal cycling this very small tensile zone at the peak of the TGO expanded over the peak region (Fig. 5.9(d)). Development of tensile zones at valleys of the TGO close to TBC were observed in the horizontal direction (Figs. 5.9(b) - 5.9(d)). At 101st cycle they created a continuous paths across the TGO thickness. The redistribution of stresses in the TGO causes a stress concentration at the peak of the BC. The valleys of BC were occupied by a compressive zone Fig. 5.9(c).

Considering plastic behavior of TGO, the maximum stress values were below 5.4 GPa and much smaller than in all previous calculations. Moreover the areas occupied by these tensile stress zones decreased.

### 5.1.4 Influence of BC and TGO plasticity (case F)

A new simulation has been carried out to check the influence of the BC and TGO plastic behavior on stress development in TBCs. The TBC was fully elastic and also all other parameters remained unchanged.

The stresses decreased significantly in comparison with the previous calculations. The maximum tensile stress was located at the peak of BC (see Fig. 5.10), just below the maximum compressive stress (-2.5 GPa) inside the TGO.

After the first cycle tensile stresses were obtained in TBC at off-valley and off-peak regions (Fig. 5.10(a)). Over the next 50 cycles the tensile zones were extended. Further cycling resulted in the creation of small new tensile zones next to the bottom part at the valleys (Fig. 5.10(d)). Additionally small compressive stress zones were obtained after the first cycle at valleys and the peak of TBC (Fig. 5.10(a)). These compressive zones increased during cycling up to the 101st cycle (Fig. 5.10(c)). Then the compressive zones in the valley decreased while the compressive zone at peak increased (Fig. 5.10(d)).

Within the TGO layer a small tensile zone was created at the peak (Fig. 5.10(a)) during the first cycle. All other parts of the TGO were under compressive stresses below 60 MPa. After the 51st cycle (Fig. 5.10(b)) the whole TGO was subjected to compressive stresses. After another 111 cycles, two small tensile zones at off-peak regions of the TGO were obtained (Fig. 5.10(d)). In the BC (Fig. 5.10(a)) tensile stresses were concentrated at the peak during the first cycle. Compressive stress zones were

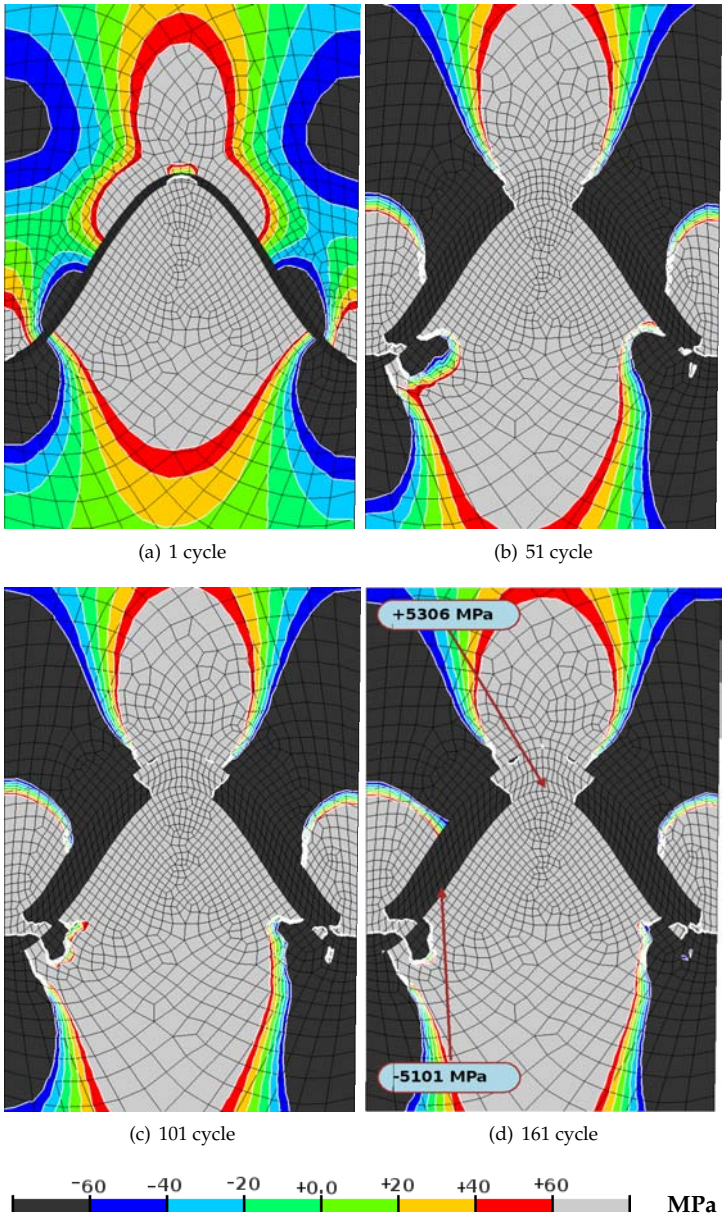


Figure 5.9: Radial stress distribution at the interface with continuous oxidation, including 5% of lateral oxidation. The TGO is modeled as ideal plastic. All other materials are purely elastic.

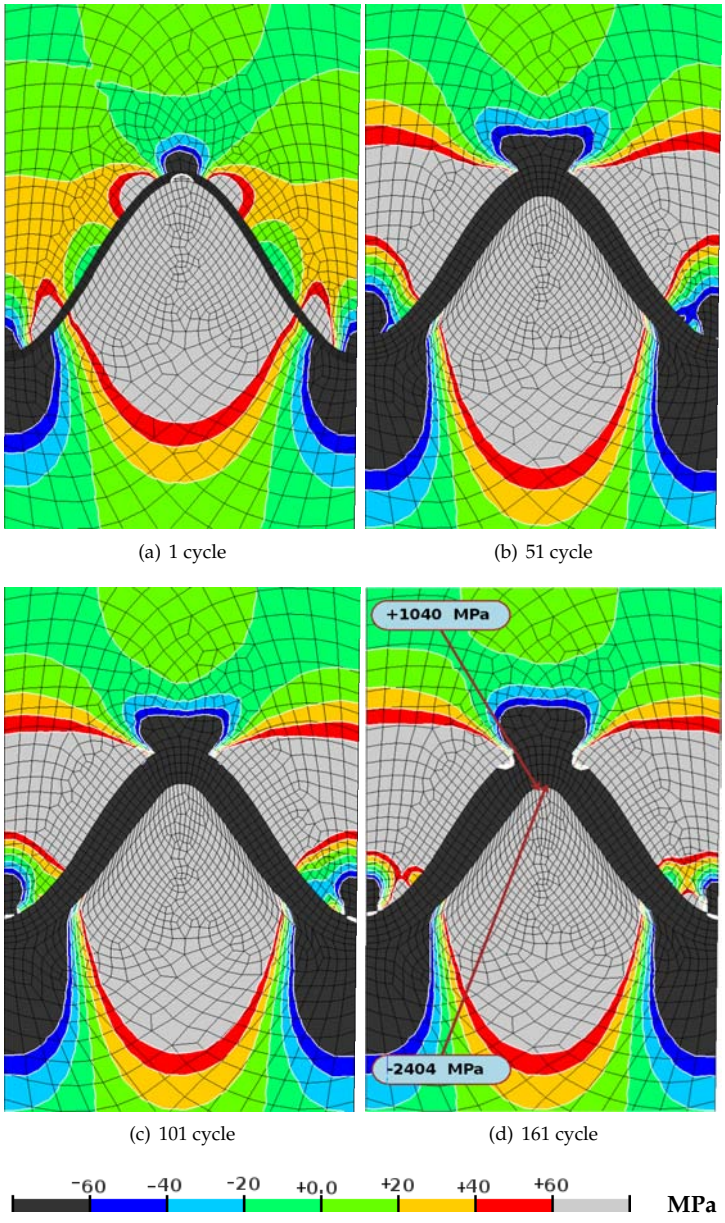


(a) 1 cycle (b) 51 cycle

(c) 101 cycle (d) 161 cycle

Figure 5.10: Radial stress distribution with continuous oxidation and plastic behavior of BC and TGO.

obtained at valleys. During cycling the tensile zone expanded (Fig. 5.10(b) - 5.10(a)) and the compressive zones increased (Fig. 5.10(d)).

Fig. 5.10 further shows a geometrical instability in the TGO layer due to strong plastic deformation of BC and the TGO layer. The deformed oxide layer became thicker at the peak Fig. 5.10(d). Moreover, the shape of TGO layer was no longer perfectly sinusoidal. As a result, the tensile and compressive stresses decreased in comparison with the previous cases.

### 5.1.5 Influence of BC creep

In the previous calculations time independent stress redistribution was studied for the TGO and the BC. However, at high temperature creep relaxation takes place. Creep relaxation and plastic deformation involve different mechanisms of deformations such as the movement of dislocations and deformation on slip planes. Therefore, results obtained by simulating only plastic response of the BC might not be sufficient to obtain a real response of the TBCs under thermal cycling loading with dwell time at hot temperature. Thus, the influence of BC creep on stress field development will be described in the following. The time dependent creep properties were implemented, as mentioned in section 3.1.3.3.

#### 5.1.5.1 Influence of the BC creep behavior and TGO plastic behavior on stress development in TBCs including continuous oxidation (case G)

Fig. 5.11 shows the stress distribution in radial direction at the end of the 1st, 51st, 101st and 161st cycle. Because stress redistribution via creep relaxation takes place even at low stresses a lower stress level was generally obtained.

Tensile stresses developed within the TBC after the first cycle at off-valley regions and at off-peak regions Fig. 5.11(a). However the valleys, middle parts and the peak were occupied by compressive stresses. These separate tensile zones at off-valley and at off-peak on the left and right side have joined and formed two tensile zones located at the left and right side from off-peak to the boundary of the unit cell (Figs. 5.11(c) - 5.11(d)). At the valleys these compressive stresses in the TBC have increased. Additionally, the compressive stress zone at the peak of TBC expanded. However, at 51st cycle a tensile zone above the peak has been obtained in the TBC layer Fig. 5.11(b). Tensile stresses at this zone first increased Fig. 5.11(c), but than decreased again Fig. 5.11(d).

Within the TGO layer (Fig. 5.11(a)) tensile stresses have occupied the peak of asperity already after the first cycle. This tensile zone decreased in size and switched fully to compressive (Fig. 5.11(b)). Instead two small tensile zones were formed after the 161 cycles at off-peak positions (Fig. 5.11(d)). All other parts of the TGO remained under compression.

As it was seen before in the cases of: 5.1.2, 5.1.3, and 5.1.4, the tensile stresses in the BC were concentrated at the peak of the asperity (Fig. 5.11). Also the stress zones

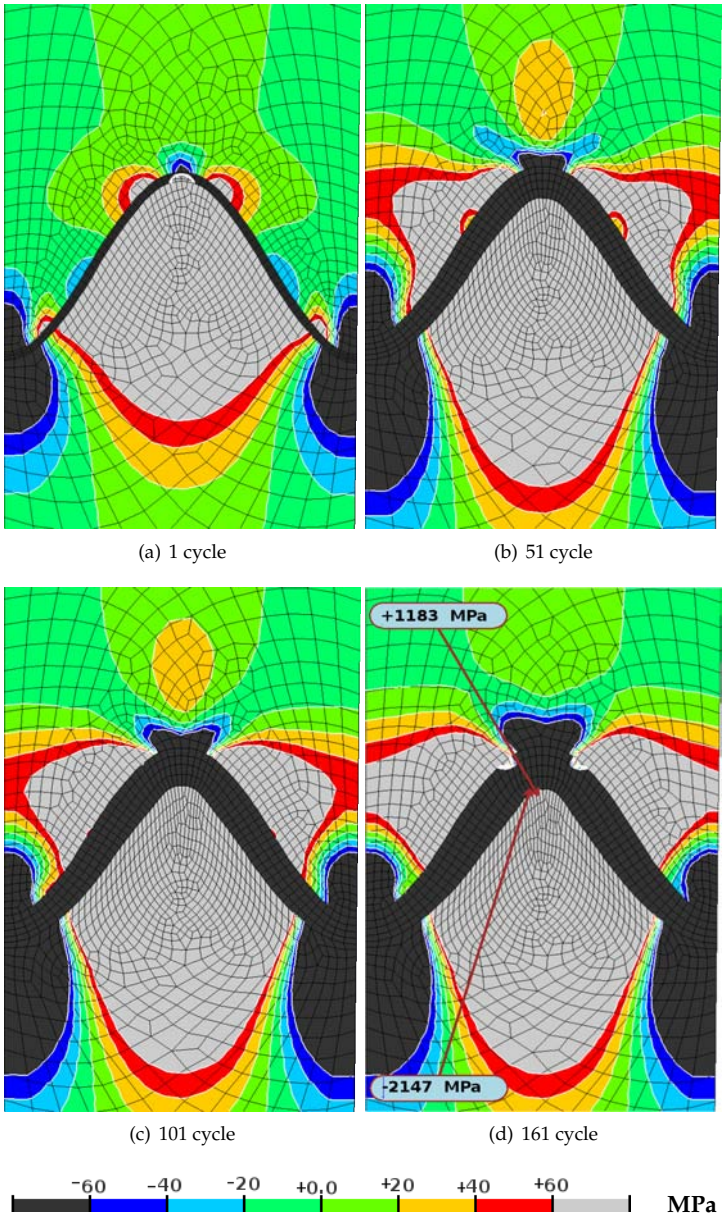


(a) 1 cycle (b) 51 cycle

(c) 101 cycle (d) 161 cycle

Figure 5.11: Radial stress distribution with continuous oxidation, considering a BC creep behavior, TGO plasticity and a fully elastic TBC.

at valleys were compressive. Moreover, the areas occupied by the stresses below -60 MPa were enlarged during cycling (Figs. 5.11(a) - 5.11(d)). The maximum tensile and compressive stresses were found at the peak of the asperity in the BC and at the peak of asperity in TGO, respectively (Fig. 5.11(d)). Additionally, geometrical instabilities were obtained as in all cases with plastic deformation of TGO (formation of inhomogeneous TGO thickness, deviations from sinusoidal shape, decrease of amplitude).

Comparing the results of BC plastic behavior with BC creep behavior one can see that the tensile stress zones in TBC over the valleys were developing slower in the case of BC creep than in the case of BC plastic behavior.

#### 5.1.5.2 Influence of visco-plastic BC behavior and TGO plastic behavior on stress development in TBCs including continuous oxidation (case H)

The combined effect of creep and plastic response of BC with consideration of plastic behavior of TGO was simulated. The implementation of creep and plastic properties of the BC is described in chapter 3.2.1. Because two deformation mechanisms are involved (creep and plastic) it was expected that the level of the developed stresses would further decrease. The obtained results are shown in Fig. 5.12.

After the 1st cycle tensile zones in the TBC were obtained at four locations. During further cycling, higher tensile stresses and larger tensile zones developed (Fig. 5.12(b)). Moreover, the off-valley zones joined with the zone at off-peak regions and formed a single tensile zone over the valley from off-peak to the boundary of the unit cell (Fig. 5.12(c)). However at valleys and above the peak compressive stress zones were present (Fig. 5.12).

A concentration of tensile stresses was observed in the TGO layer, after the 1st cycle at the peak region. Other parts of TGO were in a compressive mode Fig. 5.12(a). The tensile stresses at the peak region of TGO decreased and switched to compressive during the next 50 cycles (Fig. 5.12(b)). Instead at off-peak regions in TGO, small tensile zones were created Fig. 5.12(c). These tensile zones increased (Fig. 5.12(d)) in size during cycling.

The relaxation and plastic deformation of BC concentrates the tensile stresses at the peak of BC (Fig. 5.12(a)). The valleys of BC are occupied by compressive stresses. The stress values in these three zones (two compressive and one tensile zone) also increased during cycling Fig. 5.12(d).

Based on these results one can conclude that time dependent deformation of the BC should be always considered in an FE-model. Otherwise the behavior of bond coat at high temperature would not be properly reproduced. However, one can expect an additional mechanism involved in stress redistribution which is the irreversible deformation of the TBC. Thus the following calculations will assume TBC creep.

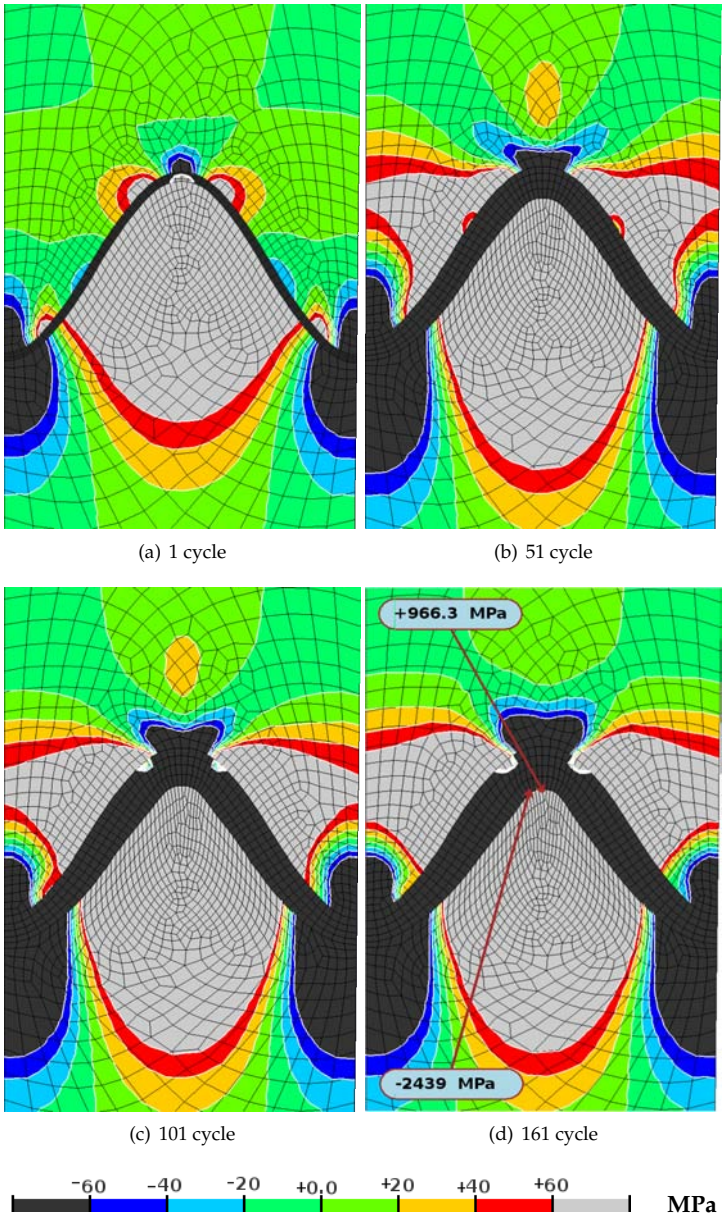


(a) 1 cycle (b) 51 cycle

(c) 101 cycle (d) 161 cycle

Figure 5.12: Radial stress distribution with continuous oxidation, with a combined elasto-plastic and creep response of BC. The TGO was modeled as elasto-ideal plastic. Other parameters remained as in the previous calculations.

### 5.1.6 Influence of TBC creep

It was shown in the previous calculations that BC and TGO are able to redistribute the stresses via plastic and viscous deformation. The TBC was at each time considered as fully elastic. However it was shown [24; 25] that the TBC is able to undergo a time dependent irreversible deformation. Thus, in the following creep behavior of the TBC is considered as described in chapter 2.2.

#### 5.1.6.1 Influence of the BC and TGO plastic behavior with consideration of TBC creep behavior on stress development in TBCs including continuous oxidation (case I)

In a first simulation with TBC creep behavior, BC and TGO are implemented as plastic materials. Others parameters of the simulation remain identical with the previous ones.

Fig. 5.13 shows the radial stress distribution and its development over time. At the end of the first cycle (Fig. 5.13(a)), tensile stresses were concentrated at the peak of asperity in BC. The valleys of asperity in BC were under compressive stresses Fig. 5.13(a). During cycling high tensile (grey) and compressive (black) stresses in BC were increased and occupied bigger areas in the vicinity of asperity. These stresses created large stress gradients (Fig. 5.13(d)).

However, a close inspection of the stress distribution after the first cycle (Fig. 5.13(a)) shows that tensile stresses were formed at off-peak regions in the TBC. The valleys in TBC were under compressive stresses (Fig. 5.13(a)). At the peak of asperity compressive stresses were present. During cycling the off-peak tensile zones expanded and the stress values increased. However, compressive stresses at valleys and at the peak of asperity were decreasing during cycling, but were still present at valleys and at the peak after 161 cycles.

In the TGO layer tensile stresses were concentrated at the peak after the first cycle (Fig. 5.13(a)). During the next 50 cycles this tensile zone decreased as the values of stresses did (Fig. 5.13(b)). Additionally at off-peak regions small tensile zones were created (Fig. 5.13(c)). Further thickening of the TGO layer with plastic redistribution of stresses and TBC relaxation decreased the tensile zone at the peak. Finally this zone switched to compressive Fig. 5.13(c), while the tensile stress zone at off-peak regions increased in size and in stress value.

The TBCs benefit from stress relaxation via creep in the TBC layer. The maximum stress in the TBC remained at the present simulation indeed below 100 MPa (Fig. 5.13(d)). However lateral tensile paths still existed and were located over the valleys within the TBC layer.

In the case of TGO plastic behavior (5.1.3) and in the case of combined BC and TGO plastic behavior (5.1.4) geometrical instabilities of the oxide layer (interface) were obtained. By including TBC creep, thus relaxing the stresses, these geometrical instabilities turned out to be stabilized.

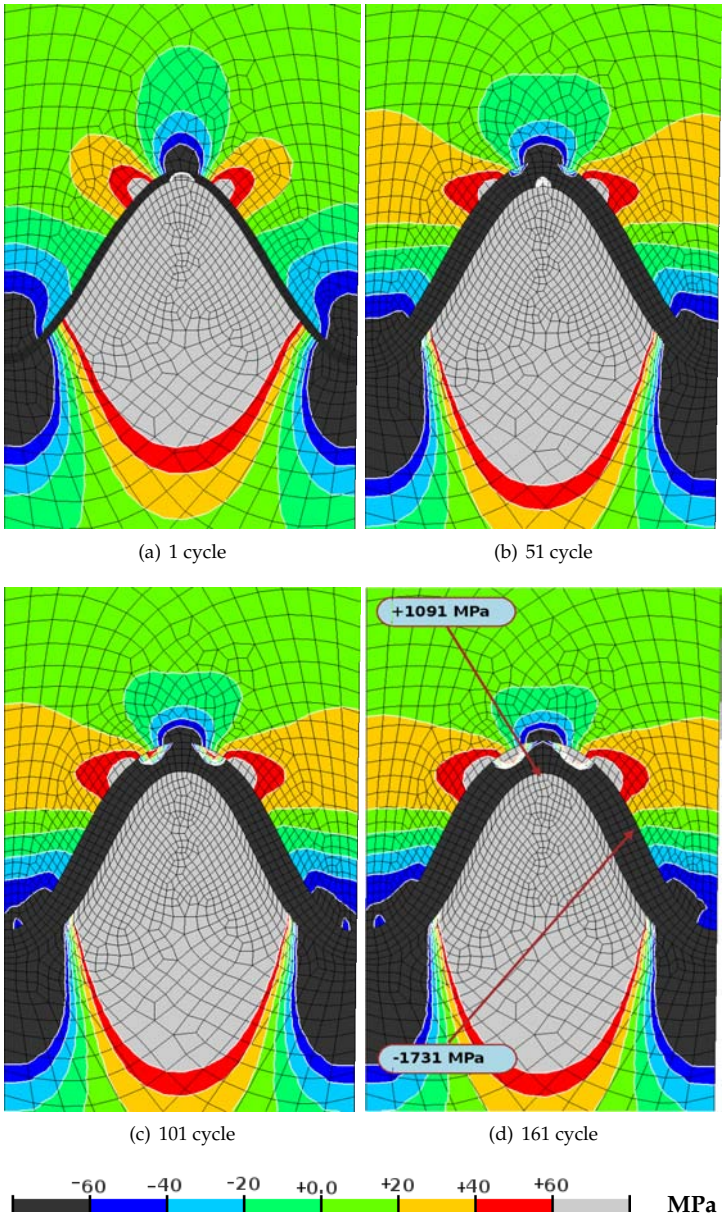


(a) 1 cycle (b) 51 cycle

(c) 101 cycle (d) 161 cycle

Figure 5.13: Radial stress distribution with continuous oxidation and plastic behavior of BC and TGO. The TBC was modeled as creep.

#### 5.1.6.2 Influence of the BC and TGO plastic behavior with consideration of BC and TBC creep behavior on stress development in TBCs including continuous oxidation (Reference case also referred as J or roman number I)

In the following simulation BC and TBC can relax stresses via creep and additionally BC and TGO redistribute stresses via plastic deformation. The influence of realistic material data set for CMSX - 4, bond coat, thermally growth oxide and thermal barrier coating on the stress development during thermal cyclic loading was studied here. Similar to the last section a concentration of tensile stresses at the peak in the BC was obtained (Fig. 5.14(a)). The valleys of BC were under compression. Thickening of the TGO increased tensile and compressive stresses in the BC. Additionally the zones occupied by tensile and compressive stresses were expanded and created large stress gradients (Figs. 5.14(b) - 5.14(d)).

The stress development in TBC was almost similar to the previous case (5.1.6.1). However the tensile zone at the peak in the TGO decreased faster and switched already at the 51st cycle completely to compressive (Fig. 5.14(b)). But the tensile zones at off-peak regions in TBC were developing faster and the stresses became larger Fig. 5.14(d) compared to Fig. 5.13(d) (5.1.6.1).

The stresses in the TGO relaxed further than in the case studied above (5.1.6.1). The tensile stresses at off-peak regions in TGO were smaller Fig. 5.14(d) compared to those without BC creep relaxation Fig. 5.13(d). Moreover the maximal tensile stress were below 1 GPa and compressive are above -1.6 GPa after 161 cycles.

Considering the influence of TBC creep on stress development in comparison with only plastic behavior of the BC and TGO (5.1.4) one can see a benefit from stress relaxation Fig. 5.14(d). This was manifested by generally lower maximum radial tensile stress, and particularly in the TBC they were below 80 MPa. Additionally geometrical instabilities of the oxide layer were stabilized.

Stress field distribution obtained under consideration of BC visco-plastic behavior and TGO plastic behavior compared to only plastic behavior of the BC and TGO showed both a similar stress field distribution in the vicinity of asperity. However, the maximum radial tensile stress values were lower in the case of BC visco-plastic behavior. In both studies geometrical instabilities of the TGO were observed.

Based on obtained results one can conclude that continuous oxidation has a strong influence on stress field development. The plastic behavior of TGO was the second important parameter, which influenced strongly stresses in TBCs. The TBC creep is to be a third important parameter that influences the stress development, as it was shown that BC creep reduced further the maximal stress values in the TBCs. Therefore, it can be concluded that a realistic reliably data of: BC and TBC creep behavior, BC and TGO plastic behavior, as well as continuos oxidation is required to model properly the TBC system and in following such a data set would be referred as a realistic model of TBCs or reference case.

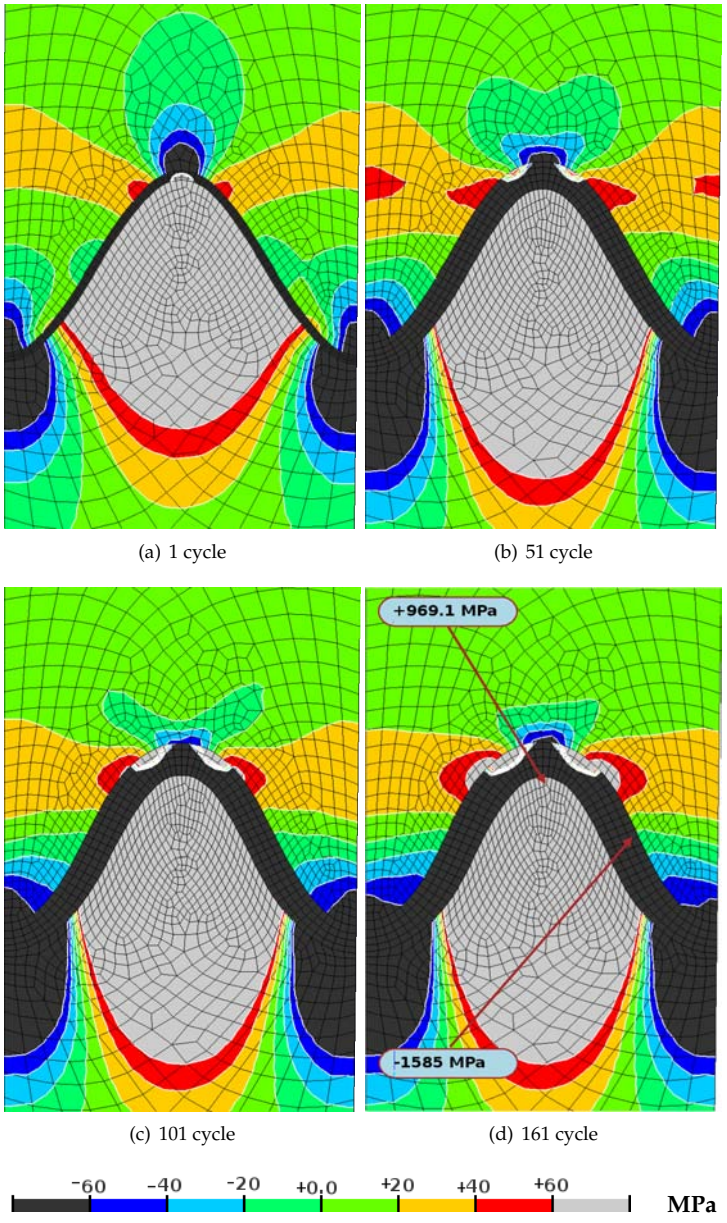


(a) 1 cycle (b) 51 cycle

(c) 101 cycle (d) 161 cycle

Figure 5.14: Radial stress distribution with continuous oxidation, with a combined elasto-plastic and creep response of BC and TBC creep behavior. The TGO was modeled as perfect plastic. Other parameters remained unchanged as in the previous calculations.

### 5.1.7 Stress development during the first two cycles

Many authors have reported ongoing crack propagation in some cases up to failure after cooling down to ambient temperature [50]. As tensile stresses can be seen as driving force for crack propagation the results presented hereafter concentrate on the stress distribution within TBCs during the first two cycles.

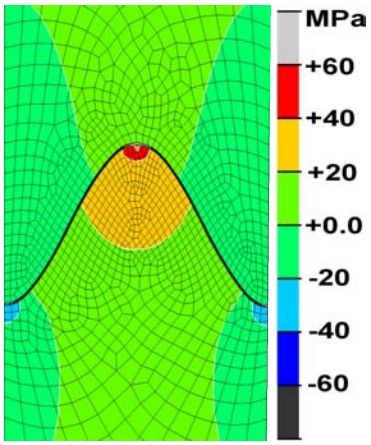


Figure 5.15: Radial stress distribution after cooling to RT from the stress free temperature, considering elasto-plastic and creep response of BC and TBC creep behavior. The TGO was modeled as perfect plastic.

However, a complex process is responsible for the stress evolution, namely oxide growth as well as thermal mismatch and the mechanical behavior of the different layers. For better understanding the stress development during cycling the present section focuses on how stresses evolve during heating, dwell time at high temperature, and cooling to RT. The thermal cycle is described in detail in chapter 3.2.1. It has to be noted that the simulation is started at $200^oC$, where the complete TBCs are stress free. Than it is cooled down to RT before thermal cycling starts. The corresponding stress state is shown in Fig. 5.15. The BC exhibits combined elasto-plastic and creep response, however the TBC was only considered to undergo creep deformation, whereas the TGO is modeled as elasto-perfectly plastic material. The implementation of the material properties is described to chapter 3.2.1.

Fig. 5.16 and Fig. 5.17 show the stress distribution at 1st and 2'nd cycle, respectively. Each time six results are presented at different steps, namely, after heating to $750^oC$ and to $1050^oC$, at the end of the 2h dwell time at $1050^oC$, after cooling to $750^oC$ and to RT, and at the end of the holding time at RT. The stress evaluation is by the following discussed separately, layer per layer, starting with the TBC.

After cooling from the stress free state to ambient temperature, small tensile stresses were obtained at the peak, whereas the valleys were under compression (Fig. 5.15). During heating stresses first decreased as they reached the initially stress free temperature of $200^oC$. At $750^oC$ the peak was occupied by compressive and the valleys by tensile stresses. As the TBC can relax stresses in the temperature range between $750^oC$ to $1150^oC$ via creep, further heating to $1050^oC$ resulted in a decrease of the tensile zones at valleys. At the end of the dwell time at high temperature, as oxidation is the driving force for stress development, more important tensile stress zones were

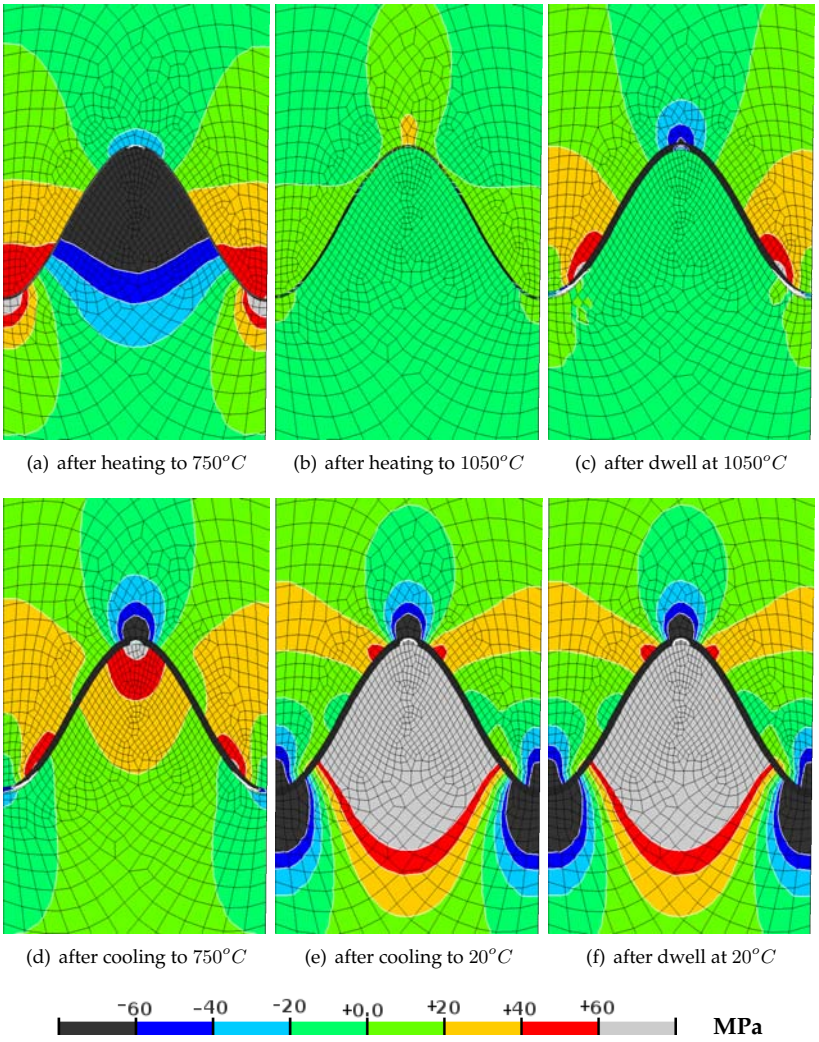


(a) after heating to $750^oC$ (b) after heating to $1050^oC$ (c) after dwell at $1050^oC$

(d) after cooling to $750^oC$ (e) after cooling to $20^oC$ (f) after dwell at $20^oC$

Figure 5.16: Radial stress distribution at different steps during the 1st cycle. All stresses are in MPa.

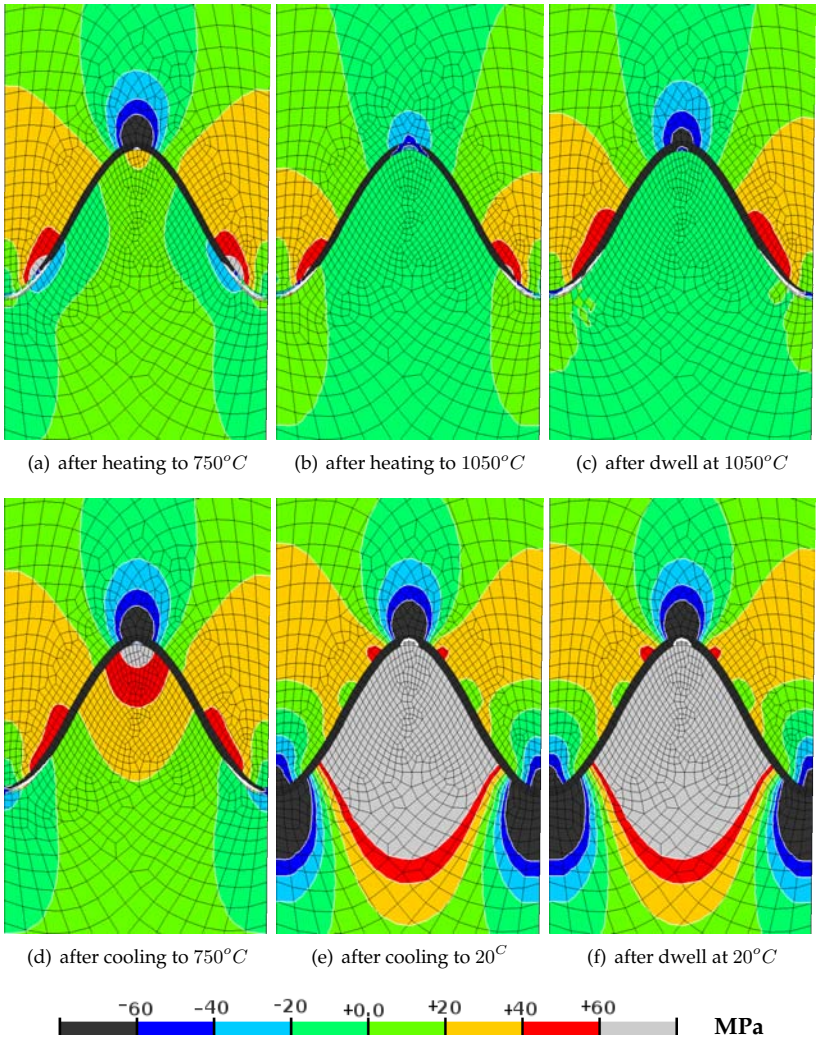


Figure 5.17: Radial stress distribution at different steps during the 2'nd cycle. All stresses are in MPa.

again obtained at valleys. During heating also the compressive stresses at the peak decreased and switched its sign to tensile as the oxidation rate is higher than creep relaxation rates. By that stress development is dominated. During dwell time at high temperature the bond coat oxidation led to compressive stresses at the peak in the TBC. During subsequent cooling to $750^oC$ the compressive stresses at the peak further increased. At the bottom of the valleys it also came to compressive stresses. Only off-valley regions were under tensile stresses. Further cooling to RT slightly decreased the compressive stresses at the peak. Whereas the valleys were now under larger compressive stresses. The tensile stresses at off-valleys also decreased. In the mean time lateral tensile zones were obtained at off-peak positions. The dwell time at RT did not influence the stress distribution as creep and oxidation are not acting at low temperature. During re-heating to $750^oC$ in the second cycle the tensile stresses at off-valleys became bigger. The bottom parts of the valleys and the peak were again occupied by compressive stresses. Further temperature increase resulted in a relaxation of stresses as for the first cycle. During the dwell time at high temperature the tensile and compressive stresses at the peak and the valleys increased, because the influence of TGO growth was stronger than stress relaxation. Cooling to $750^oC$ further increased the stresses. After cooling down to RT, mainly the build-up of a compressive zone at the bottom of the valley was observed, as for the first cycle. Also the shift to off-peak positions of the tensile zone took again place. Generally the distribution of stresses were not very different during the second cycle. However, the stress values have become more important.

The stress development during the first two cycles in the *Thermally Grown Oxide* is as follows. After cooling from the stress free state ($200^oC$) to RT only a small area of the peak is occupied by tensile stresses. All other parts are under compression. During heating to $750^oC$ the stresses switched from tensile to compressive and vice versa. Further heating resulted in decrease of tensile zones in the TGO. As oxidation dominates the stress development in the TGO layer during the dwell time at high temperature tensile stresses decreased and only remained at off-valleys close to the BC layer. Cooling down to $750^oC$ further decreased tensile stresses at off-valleys. However, a small tensile region was obtained at the peak next to the BC layer. This tensile region slightly increased in size to the end of the cycle. At the same time the tensile stress region at the valley switched to compression. Re-heating in the second cycle resulted in diminishing the tensile stresses at the peak. As for the previous cycle tensile zones were obtained at the off-valleys close to the BC. During dwell time at high temperature the tensile zones at off-valleys slightly increased, whereas at the peak the compressive stresses decreased. During cooling the compressive stresses at peak again switched to tensile and the tensile stresses at valleys disappeared. During dwell time at RT no changes were observed as the stress level is below the criterion of plastic deformation and time-dependent deformation was not consider below $750^oC$.

The present paragraph describes the stress development during the first two cycles in the *Bond Coat*. After cooling from the stress free state to RT, tensile stresses were concentrated at the peak of the BC, whereas its valleys were under compression. The remaining BC is nearly stress-free. During heating to $750^oC$, tensile and compressive

stresses switched their sign. With further heating to $1050^oC$ the stress level decreased in a way that the whole BC remained practically stress-free (above -20 MPa and below +20 MPa) during the high temperature dwell time. This happened due to fast relaxation rates in the BC at these temperatures. The dwell time at high temperature further decreased the stresses in the BC. However, during cooling to $750^oC$ stresses again increased and switched to tensile at the peak and to compression at valleys. With further cooling to RT these two stress zones largely increased in size.

Re-heating to $750^oC$ results in decreasing of tensile and compressive stresses at peak and valleys. Nevertheless, two small tensile zones (below 20 MPa) at valleys close to TGO were obtained. Also compressive zones were present below these tensile zones. Additionally at the peak and below the peak a tensile zone was present. With further heating to high temperature stress field distribution and stress values in the BC became similar to the first cycle. As the stress distribution at high temperatures before cooling down was similar to the first cycle, also the stress evolution during cooling down was similar.

In this chapter the stress development during the first two cycles was described in details. It was shown that high tensile stresses were also present at high temperature mainly at off-peaks of the TBC and also partially at the off-valley regions of the TGO. The cracking scenario can be proposed as at ambient temperature the radial tensile stresses concentrated at the peak in the BC and partially in the TGO already during the first and second cycles. Such distribution suggested possible crack formation at the peak within TGO and at the BC/TGO interface. However, as it was shown in the previous simulation (full simulation of 161 cycles) that the tensile zone at the peak within TGO decreased during cycling. This evidence indicated that such micro-crack formation would be stopped within less than 50 cycles due to the stress conversion from tension to compression. Contrary to this stress conversion at off-peak regions within TGO instead compressive stresses tensile were obtained. Additionally in the TBC the presence of more important radial tensile stresses above valley regions were obtained. These tensile zones could be correlated with crack formation within the TBC above valley regions and further propagation into TGO at off-peak regions. Finally it can be expected that a crack from off-peak would link with micro-cracks at peak in the TGO and spallation in TBCs could occur.

The presence of residual stresses at high temperature emphasizes the important role of selecting a stress free state temperature. Moreover, it proved that high temperature which was chosen by others of stress free state can give rise to misinterpretations. Here the temperature of $200^oC$ equivalent to the sample temperature during the coating spray process was properly selected for our simulations.

## 5.2 Variation of Material properties and interface shape

In chapter 5.1.6.2 we defined a reference case, which consists of a simulation up to 161 cycles and considers the most realistic available material properties of the involved materials, including oxidation growing. However the material properties are still subject of discussion, and even a realistic data set must not necessarily reflect the stress response under real conditions. As a result of these reflections the following chapter studies different variations of material properties as well as shape (Tab. 5.2) and crack formation and shows the respective influences on stress development in TBCs.

Table 5.2: The assignment of different variation of material properties and shapes based on the reference case (**I**).

| Case | Layer/Interface | Variation | Properties |
|---|---|---|---|
| **II** | BC | A 50% higher | thermal expansion coefficient |
| **III** | BC | A 50% lower | thermal expansion coefficient |
| **IV** | TBC | A 50% higher | thermal expansion coefficient |
| **V** | TBC | A 50% lower | thermal expansion coefficient |
| **VI** | CMSX-4 | A 50% higher | thermal expansion coefficient |
| **VII** | CMSX-4 | A 50% lower | thermal expansion coefficient |
| **VIII** | TBC | A 50% higher | Young's Modulus |
| **IX** | TBC | A 50% lower | Young's Modulus |
| **X** | BC | A 1000 times higher | creep rate |
| **XI** | BC | A 1000 times lower | creep rate |
| **XII** | TBC | A 1000 times higher | creep rate |
| **XIII** | TBC | A 1000 times lower | creep rate |
| **XIV** | TGO | | creep without plasticity |
| **XV** | TGO | | creep |
| **XVI** | CMSX-4 | | creep |
| **XVII** | TGO | 0% | lateral oxidation |
| **XVIII** | TGO | 20% | lateral oxidation |
| **XIX** | sinusoidal | $30\mu m$ | amplitude |
| **XX** | sinusoidal | $30\mu m$ | wavelength |
| **XXI** | sinusoidal | $90\mu m$ | wavelength |
| **XXII** | semicircle | | |
| **XXIII** | semiellips | $90\mu m$ | wavelength |

### 5.2.1 Influence of Thermal expansion coefficient

As simulations were performed for cyclic thermal loading with a dwell time of 2 h at $1050^oC$, the thermal expansion coefficient influences the stress response. The possible impact on stress development in TBCs by extreme increase or decrease of thermal expansion coefficient in TBC, BC and base material is studied in this section. All other parameters of the following simulations remain as in the reference case.

#### 5.2.1.1 Influence of a 50% higher thermal expansion coefficient in BC.

By considering a thermal expansion coefficient increase of a 50% for the BC, a stress field as shown in Fig. 5.18 has been obtained each after selected number of cycles at RT. At off-peak regions in TBC tensile zones were present, which formed a continuous tensile path from off-peak to unit cell boundary. Peak and valleys of this layer were under compression. Moreover, the TGO layer was also under compression, except the peak region. Additionally compressive stress zones were obtained at valleys of asperity in BC. The peak of BC was under tensile mode and stresses were concentrated there. In the next 50 cycles (Fig. 5.18(b)) tensile stress zones at off-peak regions in the TBC increased. Additionally, the compressive stress zones at valleys and at the peak of asperity in TBC have also increased. Such expansions of tensile and compressive zones created large stress gradients. After 51st cycle the tensile stress zone at peak of asperity in TGO has diminished. Instead, the two small tensile stress zones at off-peak regions were obtained. Other areas of TGO were under compression. Generally, the values of tensile and compressive stresses were increased in the TGO. The tensile stress zones at 161st cycle at off-peak is shown in Fig. 5.18(d). During cycling the compressive zones at the valleys in TBC expanded and the values of compressive stresses increased (Fig. 5.18(b) - 5.18(d)). Additionally the values of tensile and compressive stresses in BC have increased during time. The maximum tensile stress of 1547 MPa was found at peak of asperity in BC close to the oxide layer. The maximum compressive stress of -2414 MPa was found at the middle region in TGO (Fig. 5.18(d)).

A variation of the thermal expansion coefficient of the bond coat by an increase of 50% results in higher tensile and compressive stresses in TBCs. Moreover the tensile zones in TBC layer at off-peak regions occupy bigger areas and the tensile stress values are higher than in the reference case. Additionally the compressive stress zones (below -60 MPa) at the valley of asperity in the TBC were bigger.

#### 5.2.1.2 Influence of a 50% lower thermal expansion coefficient in BC.

Consequently with the previous case, a negative variation of a 50% lower thermal expansion coefficient is studied here. Fig. 5.19 shows the stress state at four selected cycles.

In the TBC a concentration of tensile stresses was obtained after the first cycle (Fig. 5.19(a)) from off-valley regions to the valleys. At the peak position compressive stresses were found. During cycling these tensile and compressive stresses were decreasing (Figs. 5.19(b) - 5.19(d)). Aftr the last cycle (161st) a tensile zone was present at the valley, but the stress level was below 100 MPa.

The TGO layer was after the 1st cycle under compressive stresses. Thickening of the TGO layer created within the TGO tensile stress zones at off-peak regions close to the TBC, at off-valley regions next to the BC and at the middle parts next to the BC. As a result of further cycling these tensile zones expanded (Fig. 5.19(d)). The maximum tensile stress of 331.7 MPa was localized at off-peak in TGO as indicated in Fig. 5.19(d).

The stress development in BC after the 1st cycle was different than in the case with-

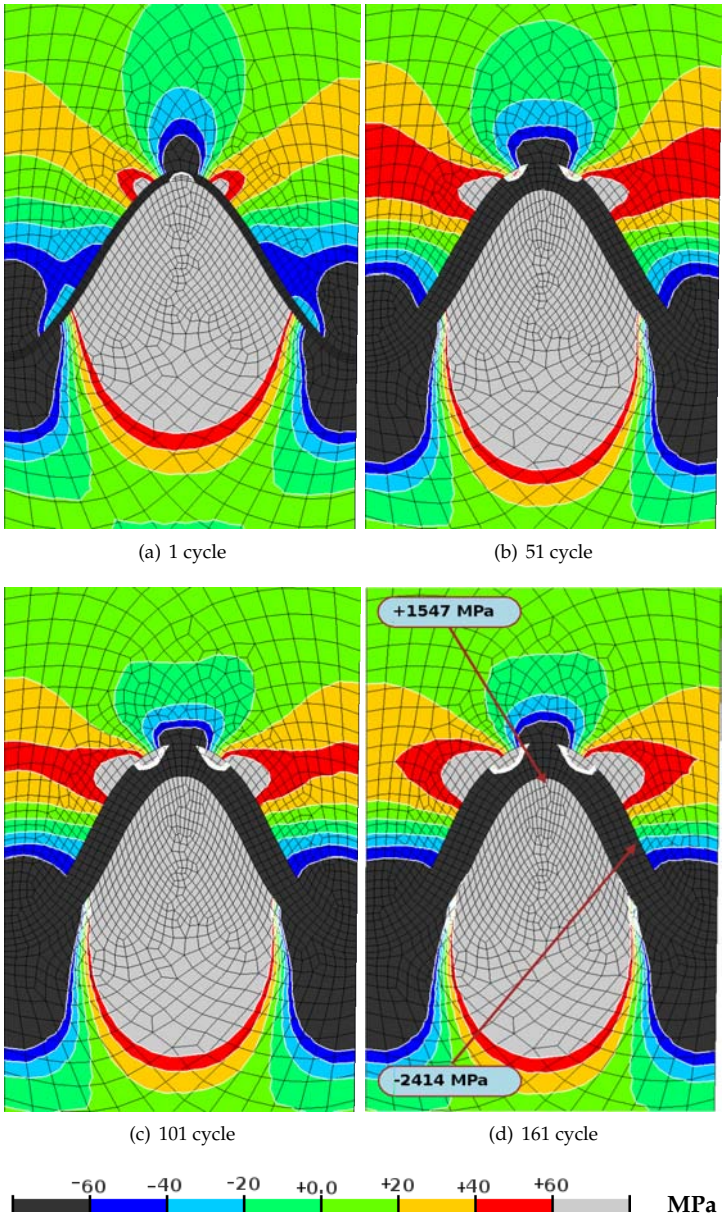


(a) 1 cycle (b) 51 cycle

(c) 101 cycle (d) 161 cycle

Figure 5.18: Radial stress distribution with consideration of a 50% higher thermal expansion coefficient for the BC has been considered. Other parameters remained as in the reference case.

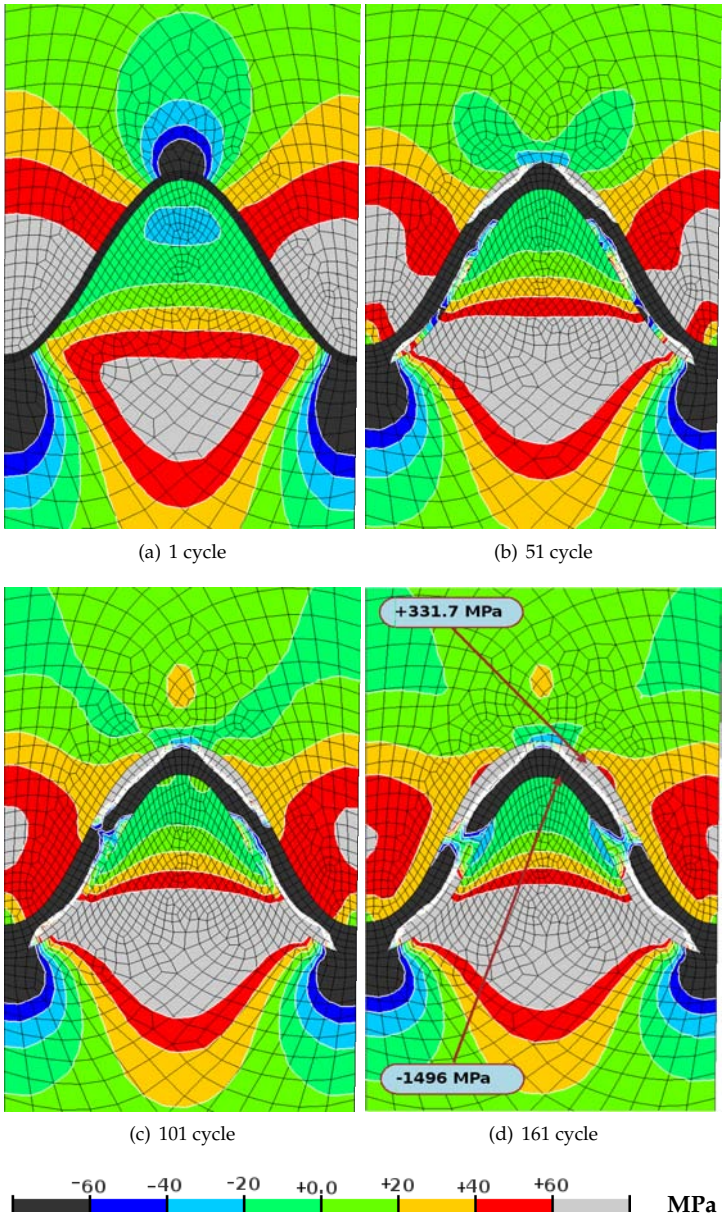


(a) 1 cycle (b) 51 cycle

(c) 101 cycle (d) 161 cycle

Figure 5.19: Radial stress distribution with a 50% lower thermal expansion coefficient for the BC. Other parameters remained as in the reference calculations.

out modification 5.1.6.2. The peak at the BC was occupied by compressive stresses, but a tensile stress zone was located under the peak Fig. 5.19(a). The valleys were occupied by compressive stresses. During cycling the compressive stresses at the peak decreased.

The tensile stresses located under the peak increased and created a continuous lateral stress zone from off-valley within the TGO, under the peak in the BC to off-valley within the TGO (Figs. 5.19(b) - 5.19(a)). Although the tensile stresses were generally very low such a stress distribution could suggest that a possible crack would be created within the BC under the peak with consideration of lower thermal expansion coefficient for the BC. However, such a crack scenario has hardly been observed under operational or experimental conditions.

#### 5.2.1.3 Influence of a 50% higher thermal expansion coefficient of the TBC

In the previous chapters the studies of increase and decrease of the TEC of BC were presented. Here the influence of an increase of the TEC on stress development in the TBC is shown in Fig. 5.20.

This increase of the TEC in the top layer effected mostly the stress distribution within the TBC layer itself. In the TBC major changes occurred in the vicinity of the interface. The radial tensile stresses within TBC increased and occupied fully the valleys in comparison with the reference case. Contrary to the reference case these stresses were higher in the TBC. During cycling the tensile stresses at off-valleys increased Fig. 5.20(b). Additionally the compressive stresses above the peak in the TBC extended (Figs. 5.20(a) - 5.20(d)).

In the BC and the TGO (Fig. 5.20(a)) stress response was only slightly affected in comparison with the reference case. A maximum tensile stress of 947 MPa was obtained at the peak in the BC next to the TGO layer and was slightly lower than in the case without modification (reference case). However the maximal compressive stresses increased about 120MPa in comparison with the reference case. This study showed the tendency of stress development in TBCs due to an increase of the TEC in the TBC. It was shown that higher TEC of the TBC resulted in higher tensile stresses at the valley regions in the TBC. This suggests that an increased of the thermal expansion coefficient in the ceramic layer should be avoided.

#### 5.2.1.4 Influence of a 50% lower thermal expansion coefficient of the TBC

With a negative modification of 50%, the TEC of TBC becomes smaller than the TEC of the TGO. The biggest differences compared to previous cases were found in the TBC layer as it is directly effected by the modified material properties. After the first cycle the valleys in the TBC were occupied by compressive stresses in both modified and unmodified cases. However, in the modified case the tensile zones at the valley regions occupied larger areas. Additionally at off-peak regions the tensile zones were smaller (Fig. 5.21(a)). During the next 50 cycles the tensile zones at off-peak regions decreased. In contrast to the reference case tensile stresses were formed at above the peak rough-

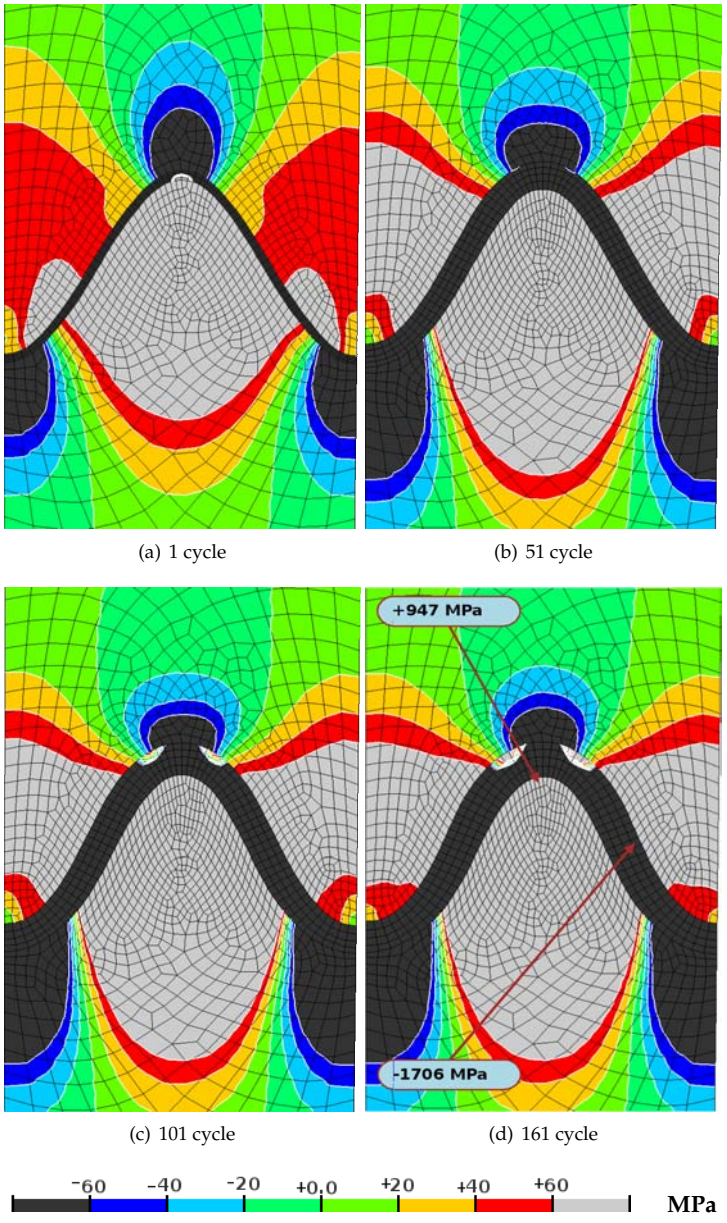


(a) 1 cycle (b) 51 cycle

(c) 101 cycle (d) 161 cycle

Figure 5.20: Development of radial stresses in the vicinity of asperity with consideration of a 50% higher thermal expansion coefficient of the TBC. Other parameters remained as in the reference case.

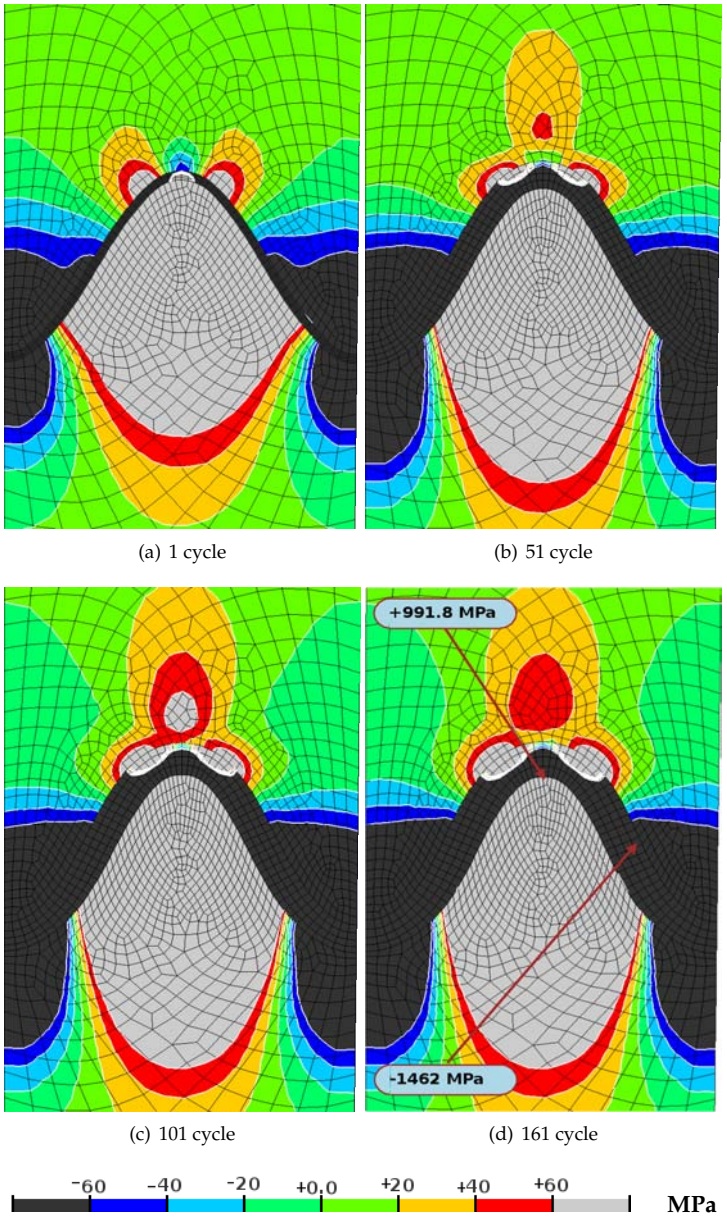


(a) 1 cycle (b) 51 cycle

(c) 101 cycle (d) 161 cycle

Figure 5.21: Radial stress distribution at selected number of cycles, including a 50% lower thermal expansion coefficient of the TBC. Other parameters remained unchanged as in the unmodified state.

ness. These three zones joined and created a tensile region at the peak from off-peak to off-peak in the TBC. This zone fused with the off-peak tensile zones of the TGO (Fig. 5.21(b)). With further cycling these tensile zones have expanded (Fig. 5.21(b) - 5.21(d)) and the values of tensile stresses have slightly increased (Fig. 5.21(d)). Moreover, the compressive stress values at valleys have increased. The maximum tensile stress of 992 MPa was slightly higher than in the unmodified case.

The stress development in the BC and TGO was only marginally affected by the modification of the TEC of the TBC compared to the reference case.

#### 5.2.1.5 Influence of a 50% higher thermal expansion coefficient of the CMSX-4

As not only the areas close to the interface might influence the stress response the increase of thermal expansion coefficient in the base material has been considered. The stress developments in the BC and TGO were similar to the unmodified state. However, the maximum tensile stress of 805.1 MPa obtained at the peak of asperity in the BC was lower than in the unmodified case. The maximum compressive stress of -1672 MPa was obtained at the off-peak region in TGO next to the BC layer (Fig. 5.22(d)). Both maximum stress values were lower in comparison with the unmodified state.

Comparing stress distribution obtained after the first cycle in the TBC with the reference case it can be seen that the tensile zones occupied larger areas at the valley region due to an increase of the TEC in the base material. Besides the tensile stresses obtained above the peak, the lateral tensile stress zones were larger and stress values were bigger within these zones in comparison with the reference case (Fig. 5.22(d)).

#### 5.2.1.6 Influence of a 50% lower thermal expansion coefficient of the CMSX - 4

In the following the influence of a decreased thermal expansion coefficient of the base material is described, and shown in Fig. 5.23

The stress development in the BC was similar as in the reference case. However, the areas occupied by higher tensile and compressive stresses in the BC were smaller in compression with the reference case. The maximum tensile stress of 1001 MPa was obtained at the peak of asperity in the BC next to the TGO. This stress was higher than for the unmodified case. Also the maximum compressive stresses increased and a value of -1651 MPa was obtained as indicated in Fig. 5.23(d).

In the case of the TGO layer the stress development was slightly different compared to the unmodified case. Particularly the off-valley regions close to the BC developed low compressive stresses during cycling (Fig. 5.23(d)). The TBC was the most affected layer by decreasing the TEC of the base material. Fig. 5.23 shows a low tensile stress level in the TBC above valley regions. As in the reference case the valley regions and the peak were occupied by compressive stresses. During cycling more important tensile stresses were formed above valleys (from off-peak to the boundary of the unit cell Fig.5.23(b)). Further cycling resulted in decrease of these more important stresses. Instead, at off-peak regions tensile stresses below 20 MPa were formed. As in the reference case these stresses created a continuous tensile path above valley

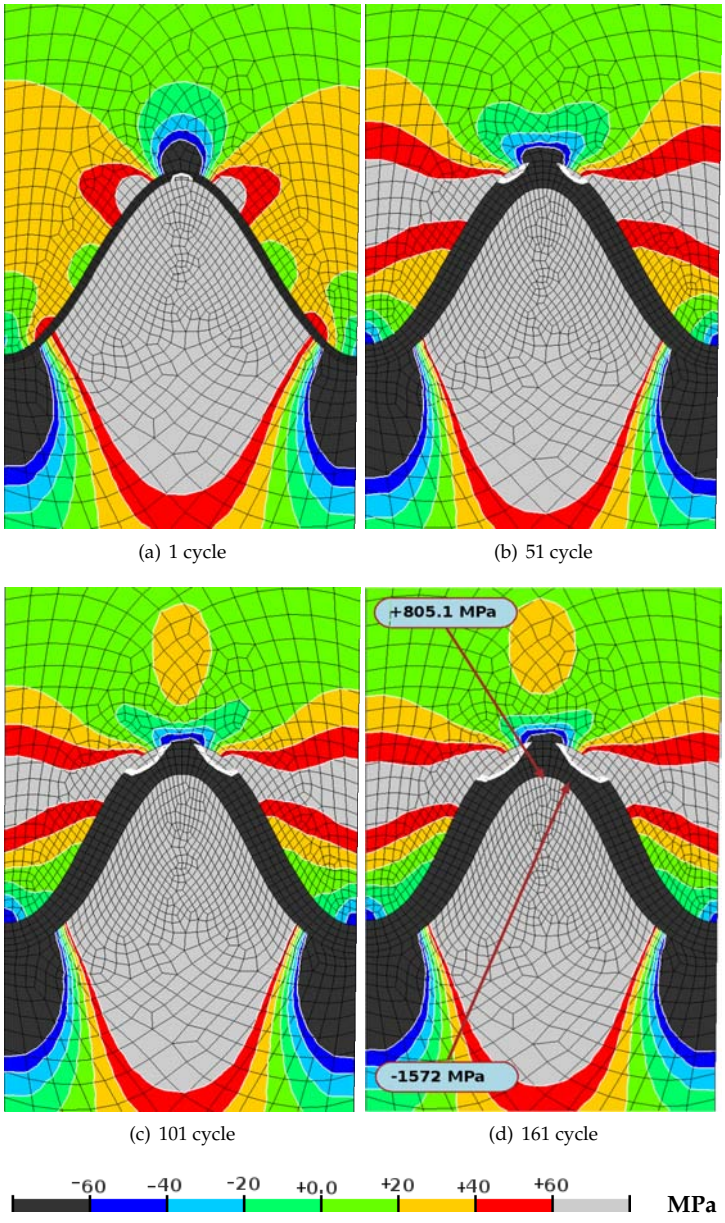


(a) 1 cycle (b) 51 cycle

(c) 101 cycle (d) 161 cycle

Figure 5.22: Development of radial stress with consideration of a 50% higher thermal expansion coefficient of the base material. Other parameters remained unchanged as in the reference case.

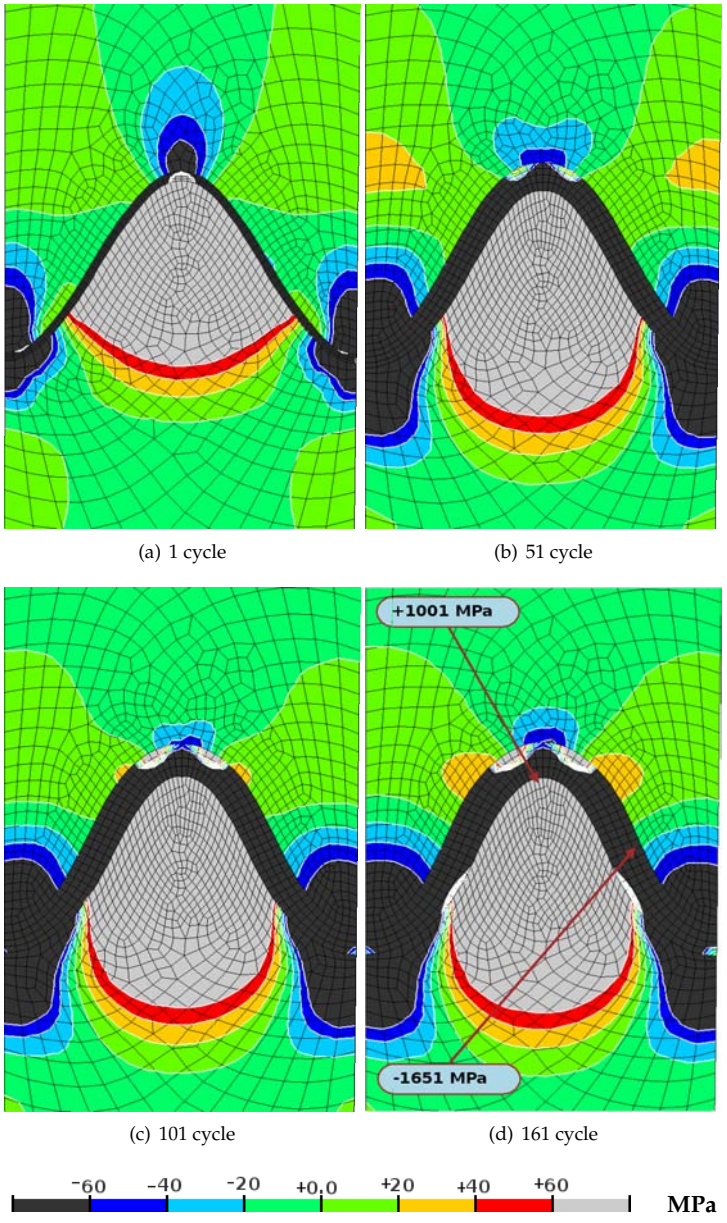


(a) 1 cycle (b) 51 cycle

(c) 101 cycle (d) 161 cycle

Figure 5.23: Radial stress distribution including a 50% lower thermal expansion coefficient of the base material. Other parameters remained unchanged as in the reference case.

regions. Although the stress values at these tensile paths were significantly lower and tensile zones were smaller.

#### 5.2.1.7 Concluding Remarks

modifications of the thermal expansion coefficient in base material (*CMSX-4*), bond coat (*BC*) and thermal barrier coating (*TBC*) have been studied. In order to clearly show its influences on stress development in the TBCs extreme variations of material properties were chosen. It was shown that increasing the TEC in the TBC layer resulted in bigger tensile stresses at valleys in the TBC layer in comparison with the reference case. Furthermore, increasing the TEC in the base material increased the tensile stresses and the size of the lateral tensile zone in the TBC. In the case of an increase of the TEC in BC also resulted in bigger lateral continuous tensile path above valley. Moreover compressive zones were bigger at the valley regions in comparison with the reference case. Additionally, the tensile stresses at the TGO/BC interface increased about 60%.

The following three cases could be beneficial: 1) Decreasing the TEC in the TBC would lead to a small increase of tensile stresses at the TGO/BC interface, but the compressive zones in the TBC at valleys would be bigger in size (Fig. 5.21(d)). 2) Considering decrease of the TEC in the base material would further decrease the tensile stresses in the TBC increasing the lifetime of TBCs, based on the assumption that lower tensile stresses or smaller tensile zones do not cause important crack formation. Additionally the compressive zones would increase (Fig. 5.23(d)). The maximum tensile stress in the TBC after 161 cycles could indeed be reduced from 79 MPa to 35 MPa. Thus it was shown that by decreasing the TEC of 50% in the CMSX-4 one can reduce tensile stresses in the TBC more than twice. Therefore considering a smaller decrease of the TEC should already give a profit. 3) A closer inspection of the obtained results suggest that a decrease of the TEC in BC would form tensile zones at valleys in the TBC Fig. 5.18(d). Moreover the tensile stresses in the full TBCs were small and the maximum of 331.7 MPa tensile stress was obtained in the TGO.

### 5.2.2 Influence of the Elastic modulus on the stress response

The exposure to high temperatures causes sintering in the TBC and consequently an increase of stiffness. Typical values for experimentally determined stiffness increase in case of APS-TBC is about 50% [2]. This value was selected as basis for current studies.

#### 5.2.2.1 Increasing Young's Modulus of the TBC by 50% .

Fig. 5.24 shows the stress distribution in a stiffer TBC with a 50% higher Young's Modulus compared to the reference case. The stress development is shown in Fig. 5.24. The stress distribution for each selected cycle looked similar to the reference simulation. However, as a result of an increased Young's Modulus in the TBC layer the tensile zones in the TBC appeared to occupy larger areas and the stress values were bigger in comparison to reference case. The maximum radial tensile stress of 189 MPa within the TBC was obtained after 161 cycles at the off-peak next to the TGO. The almost same position is also occupied by the maximum radial tensile stress of the TBC in the reference case, however the value decreased more than twice after the same cycle number. Furthermore, the maximum compressive stress within the TBC increased more than twice lower in the reference case in comparison with the higher stiffness of TBC. Whereas in the reference case this stress was localized at the valley next to TGO. However in the current case it shifted to the peak position.

The total maximum tensile and compressive stresses in the TBCs were also decreased compared to the reference case and the value of 927.6 MPa was obtained at the peak of asperity in the BC Fig. 5.24(d). Additionally the maximum compressive stress of -1496 MPa was found at off-valley in the TGO.

#### 5.2.2.2 Decreasing Young's Modulus of TBC by 50%

The effect of a 50% decrease of the Young's modulus of TBC on the stress response is described in the following. A lower stiffness could be obtained by higher porosity of the TBC. The stresses in the TBC were significantly lower than in the case of increasing the TBC stiffness. Tensile stress zones at valley regions in the TBC layer were obtained after the first cycle Fig. 5.25(a), except for the bottom parts of valleys where small compressive stresses were present. Moreover the peak was under compression (Fig. 5.25(a)). During cycling the tensile zones at off-valley regions decreased and after the last simulated cycle the valleys were occupied by compressive stresses (Fig. 5.25(d)). The peak of TBC and the off-peak regions were in a tensile mode Fig. 5.25(d).

After the first cycle, tensile stresses were found at the peak in the TGO layer next to the BC (Fig. 5.25(a)). Other areas in TGO were under compressive stresses (Fig. 5.25(a)). These stresses in TGO were developing in the same way as it was in the reference case (5.1.6.2). However, the tensile stress zones in TGO obtained after 161st cycle are bigger and the stresses were higher Fig. 5.25(d). The compressive stress of -1782 MPa was found at the middle part of TGO close to the TBC layer.

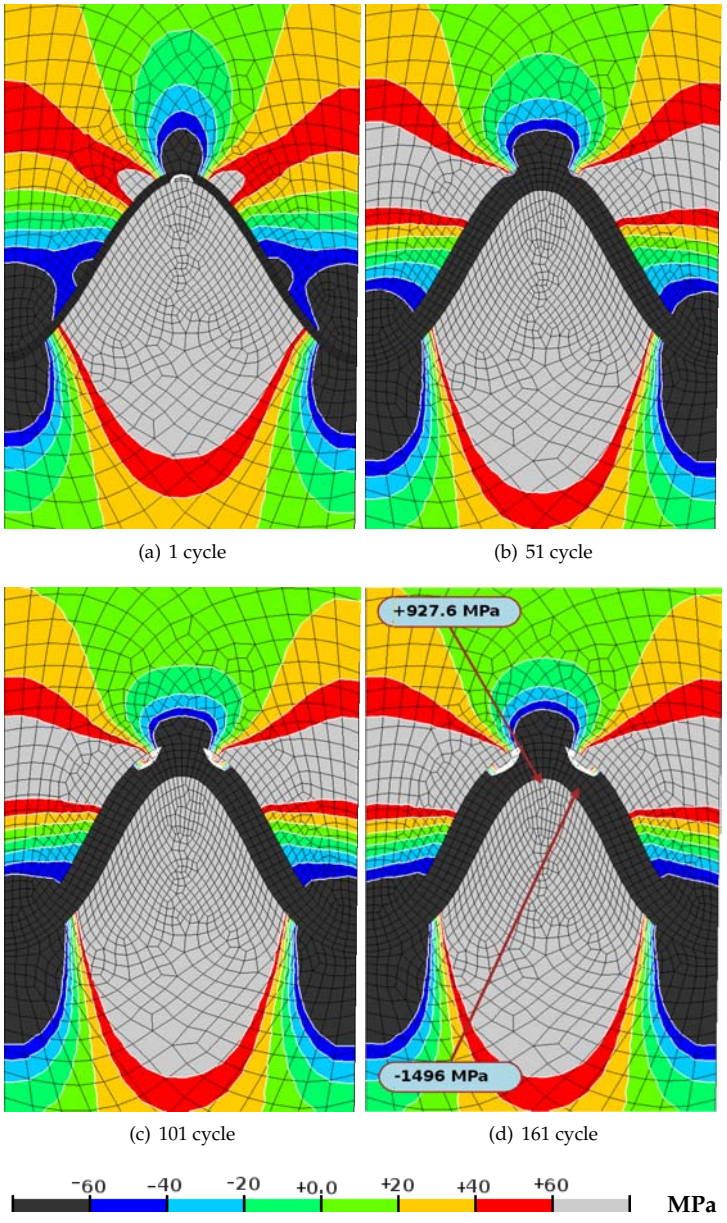


(a) 1 cycle (b) 51 cycle

(c) 101 cycle (d) 161 cycle

Figure 5.24: Radial stress distribution with consideration of a 50% higher elastic modulus of the TBC. Other parameters remained as in the unmodified case.

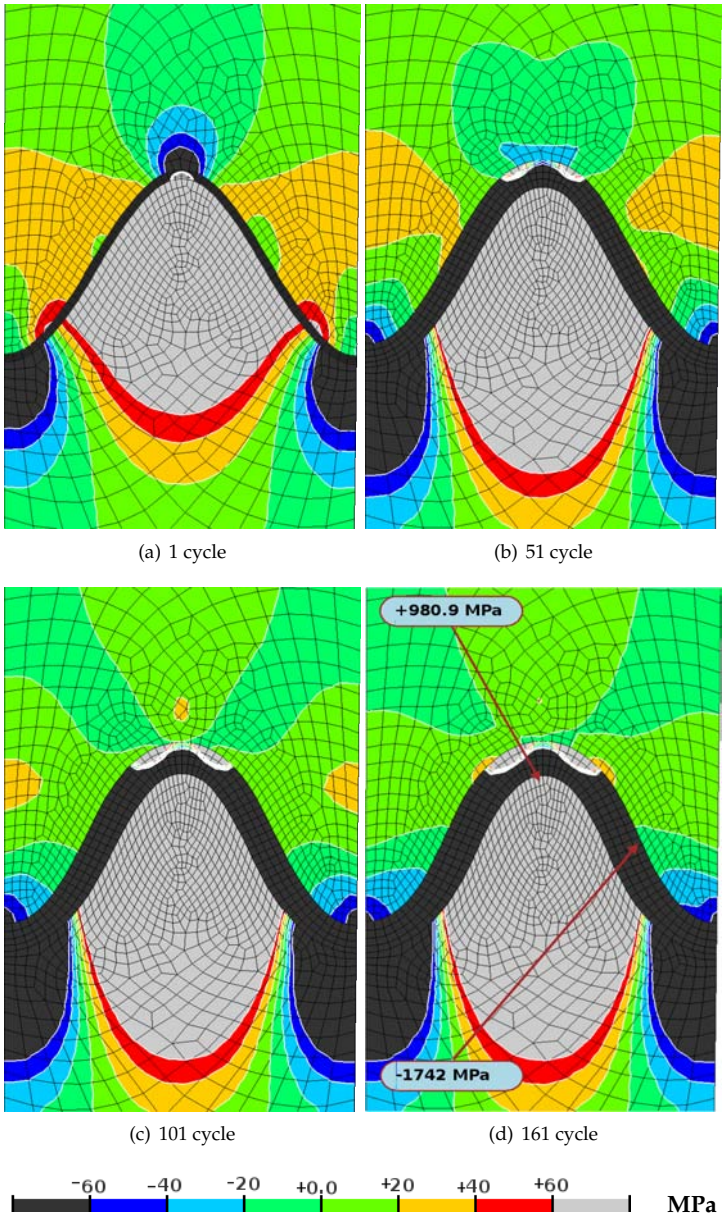


(a) 1 cycle (b) 51 cycle

(c) 101 cycle (d) 161 cycle

Figure 5.25: Development of radial stresses in the vicinity of asperity considering softer TBC (a 50% lower elastic modulus). Other parameters remained unchanged as in the reference calculations.

The stress development in the BC layer was very similar to the reference case. Namely, tensile stresses were concentrated at the peak of asperity and compressive stresses occupied valley regions (Fig. 5.25(a)). The maximum of 980.9 MPa tensile stress was obtained at the peak in the BC.

#### 5.2.2.3 Concluding Remarks

Two variations of stiffness have been studied in this section. One can clearly see a negative influence of a stiffness increase. This is manifested by continuous tensile zones from off-peaks to the boundaries of the unit cell (Figs. 5.24). However, the maximum tensile and compressive stresses decreased about 5% in comparison with the reference case (5.1.6.2).

On the other hand the TBCs profit from a more porous TBC layer, because the tensile stresses in TBC were lower than in the reference case. This is manifested by the fact that the tensile stresses within the continuous tensile path from off-peaks to the boundaries of the unit cell above the valleys in the TBC were below 10 MPa after 161 cycles. However, the maximum tensile and compressive stresses increased in comparison with the reference. The increased of maximum tensile stresses was about 20 MPa (1.2%) and can be neglected, as it is a very small variation and the BC has a rather high tensile strength at RT where these stresses appeared. This suggests to introduce a higher porosity in the TBC and to lower sintering kinetics if possible.

### 5.2.3 Variation of BC creep rates

#### 5.2.3.1 Influence of a 1000 higher times of creep rate in the BC via increase of the Norton factor in the creep equation

In this section the influence of creep rates on the stress response will be discussed. Fig. 5.26 shows the resulting stress distribution for the cycle numbers 1, 51, 101 and 161. The higher creep rates lead generally to a fast relaxation of stresses in the bond coat at temperature above $900^oC$. The high relaxation rates influence however not only the stress response in the BC, but also in the TGO and the TBC.

Although this relaxation affected the stress level in all three layers, the stress development was nevertheless similar to the reference case. The maximum tensile stress decreased about 100 MPa compared to the reference case and was located at the same place as in the reference case. Moreover the compressive stresses in the BC also decreased about 7%. Beside the stress change in the BC also in the TGO tensile and compressive stresses decreased and the maximum compressive value of -1373 MPa was located in the same place as in the unmodified case. In addition the tensile stresses in the TGO slightly decreased about 4% in comparison with the reference case.

Also the TBC tensile and compressive stresses slightly decreased about 6% in comparison with the reference case. However during cycling for about the first 50 cycle the tensile stresses above valley regions were higher and the areas occupied by these stresses were bigger (Fig. 5.26(b)). Further cycling resulted in very similar stress distribution as in the reference case.

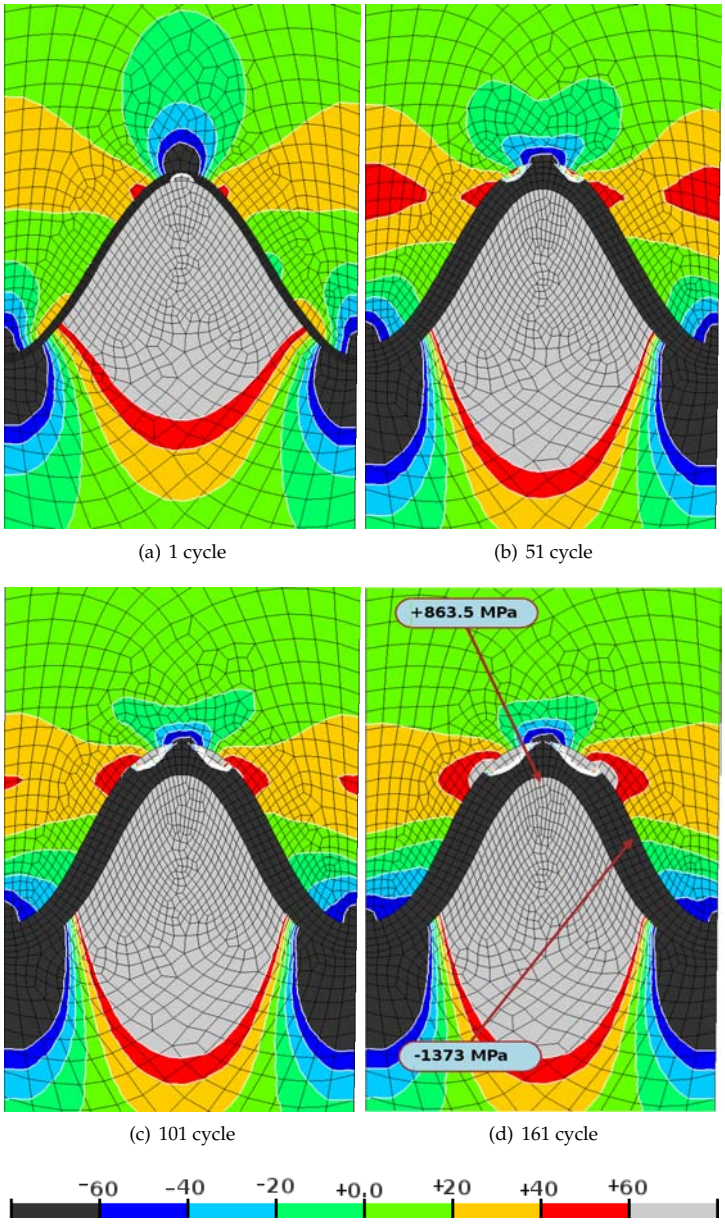


(a) 1 cycle (b) 51 cycle

(c) 101 cycle (d) 161 cycle

Figure 5.26: Influence of a higher creep rates in the BC on radial stress development at selected number of cycles. Other parameters remained as in the reference calculations.

One can conclude that higher creep rates in the BC result in lower maximal tensile and compressive stresses in TBCs. However, the tensile stress paths in TBC above the valleys of the asperity were slightly broader in comparison with the reference case (5.1.6.2).

#### 5.2.3.2 Influence of a 1000 times lower creep rate in the BC via decrease of the Norton factor in the creep equation

When the relaxation of stresses is slower due to lower creep rates the maximum tensile and compressive stress values were more than 100 MPa higher in comparison with the reference case. The values are indicated in Fig. 5.27(d).

However the stress distribution was almost identical as in the reference simulation. Not only the maximum values of stress increased also the stress level in the BC was higher of about 10%. However in the TGO the compressive stresses decreased around 20%, but tensile stresses increased about 8%. In the TBC tensile stresses were slightly lower about 2%. Again, compressive stresses were higher (about 3%) than in the reference case. Moreover the lateral tensile stress paths from off-peak regions to the boundaries of the unit cell were as not broad as in the reference simulation.

#### 5.2.3.3 Concluding Remarks

The stress development and distribution of higher and lower creep rates of BC in comparison with the reference case shows only small differences in the stress field in the TBC layer. Mostly the BC layer was affected, where higher tensile stresses were obtained with lower creep rates. It can be concluded that higher creep rates help to keep low stress values in the BC and at the BC/TGO interface. However, by analyzing the present results, one can deduce that the influence of the creep properties of the BC on the life-time of TBCs has in the past been overestimated.

### 5.2.4 Influence of TBC creep rates

Here influence of an increase or a decrease of creep rates in TBC layer on stress development was studied. This was achieved by lowering the $A$ and $A'$-factor of the creep law given in 2.2 by a factor of 1000. In following only the difference on stress development in comparison with the reference case will be addressed.

#### 5.2.4.1 Influence of a 1000 times higher creep rate of TBC

Considering higher TBC creep rates resulted in an accelerated relaxation of stresses in the TBC (Fig. 5.28(a)). The tensile stress zones at off-peak regions in TBC developed slower than in the reference case. Moreover the stress level in the TBC was lower compared to the reference case. Namely the tensile and compressive stresses decreased about 8% and 19%, respectively. Additionally the compressive stress zones at valley regions occupied bigger areas after 161 cycles (Figs. 5.28(c) - 5.28(d)).

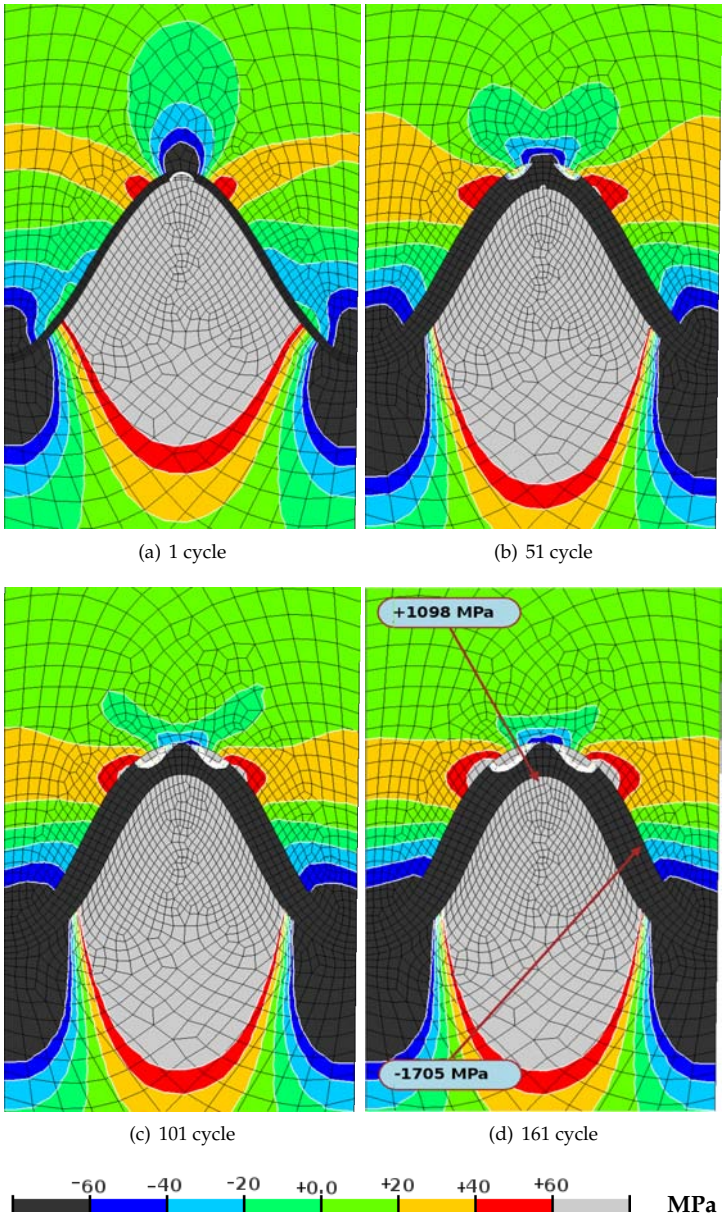


(a) 1 cycle (b) 51 cycle

(c) 101 cycle (d) 161 cycle

Figure 5.27: Development of radial stress considering a 1000 times lower creep rates in the BC. Other parameters remained unchanged as in the reference case.

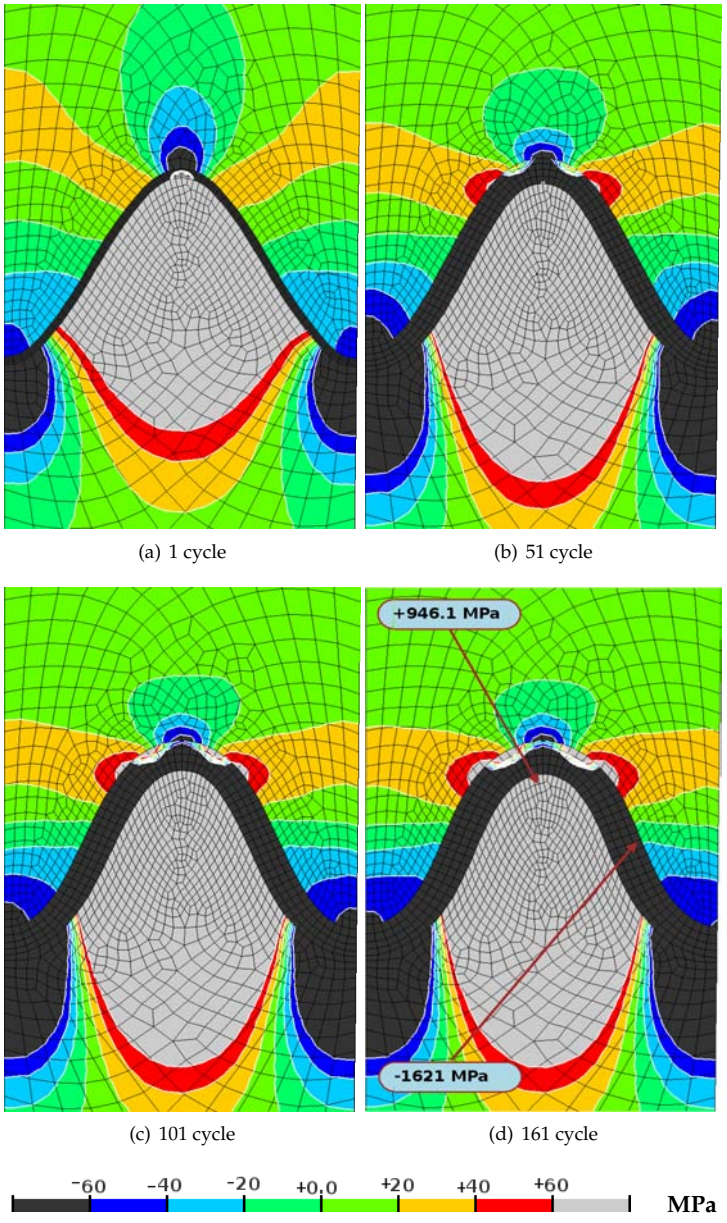


(a) 1 cycle (b) 51 cycle

(c) 101 cycle (d) 161 cycle

Figure 5.28: Radial stress considering a 1000 times higher creep rate in the TBC. Other parameters remained as in the reference case.

In the TGO the radial tensile stresses decreased about 41%, but the compressive stress slightly increased from -1585 MPa to -1621 MPa (about 3%) compared to the reference case. Moreover, the stress field in the BC is practically unchanged. Additionally the stress level slightly decreased about 2.5%.

#### 5.2.4.2 Influence of a 1000 times lower creep rate of TBC

As a next consequent step the creep properties of the TBC where modified towards 1000 times lower creep rates. All others parameters of the simulation were identical with the reference case.

By decreasing the creep rates of the TBC, relaxation in the TBC was slower. The results of the radial stress distribution are given in Fig. 5.29. In the TBC four tensile zones were obtained after the first cycles, two at off-peak regions and two at off-valley regions, each time close to the TGO interface. The peak and the valleys in TBC were under compressive stresses (Fig 5.29(a)). At the 51st cycle continuous tensile stress zones have developed, spread out from the flanks of TGO/TBC interface to the boundaries of the unit cell. The compressive stress values at valleys and at the peak also increased during cycling. Moreover both of these stress values (tensile and compressive) were higher of about 120% in comparison with the reference case. Additionally the lateral radial tensile zones were broader compared to the reference case.

Comparing the tensile and compressive stresses in the TGO with the reference case shows that these stresses increased about 80% and 36%, respectively. However the stress distribution was practically similar as in the reference case. The variation of creep rates in TBC did not influence the concentration of tensile or compressive stresses at the peak and valleys in the BC. However the maximum tensile stress of 981.4 MPa obtained at the peak in BC was slightly higher (about 1.3%) than in reference case. Also the maximum compressive stress in the TGO increased about 4.7%.

#### 5.2.4.3 Concluding Remarks

It can be concluded that lower creep rates of the TBC will result in higher stresses in the ceramic system. It could be shown that the stresses in the TBC do not relax fast enough to prevent the development of a large tensile stress path above the valleys. These tensile paths in TBC could be a reason for a lower lifetime of TBCs. Moreover, a geometrical instability of the TGO layer was obtained which is a direct effect of the lower relaxation in the TBC layer and was manifested as inhomogeneous thickness of the TGO layer. However higher creep rates of the TBC resulted in decreased of tensile stresses at BC/TGO interface. In addition, the lateral tensile paths in the TBC were not as broad as in the reference case. Furthermore, the stress level in the TBC layer decreased. Therefore one could expect a prolonged lifetime.

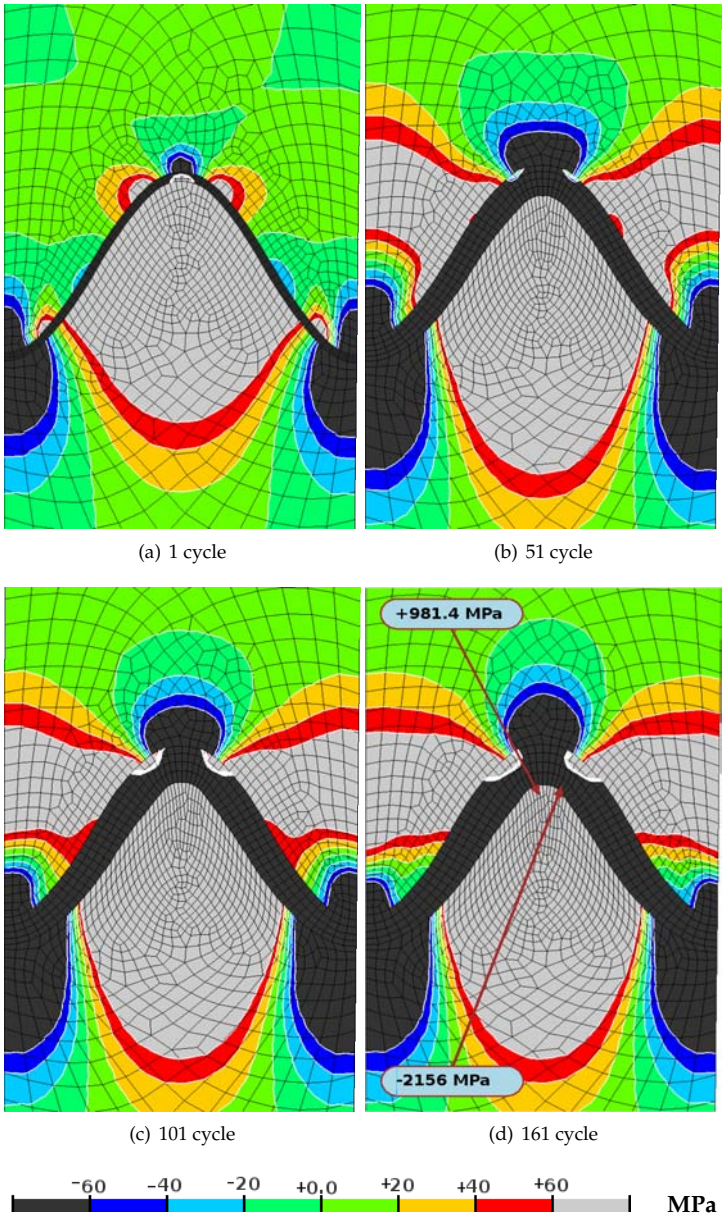


(a) 1 cycle (b) 51 cycle

(c) 101 cycle (d) 161 cycle

Figure 5.29: Influence of a 1000 times lower creep rate in the TBC on radial stress development. Other parameters remained unchanged as in the reference calculations.

### 5.2.5 Influence of TGO creep

Depending on the grain size a time dependent irreversible creep deformation can generally be observed in ceramics. A TGO, having a grain size significantly below 1 $\mu m$, was reported to undergo creep deformation [43]. Thus in the present chapter the influence of creep deformation and stress relaxation within the TGO on the stress response during thermal cycling is analyzed. The creep behavior was implemented as described in chapter 2.2. In the first step only creep without plastic deformation and in the second step creep and plastic deformation was considered. Together with the case described in chapter 5.1.6.2, for which only plastic deformation was taken into account, the relative influence of plasticity and creep can be separated and assessed.

The results for the first step are given in Fig. 5.30. After the 1st cycle a significant low stress level was observed in the TBC layer. The peak was fully occupied by tensile stresses. The valleys were still under compression as in the reference case. During cycling the tensile stresses at the peak decreased and changed to slightly compressive. However, as a general observation the tensile stress level remained very low within the complete TBC. Moreover, the tensile and compressive stress values decreased about 50%.

The TGO showed after the first cycle the same stress distribution as in the reference case. During cycling the tensile and compressive stress level in the TGO decreased about 6% and 43%, respectively, due to stress relaxation of the TGO. Here almost the complete peak remains during the whole simulation under radial tensile stresses, except the area close to the TBC layer where compressive stresses were obtained.

The relaxation process of the TGO has practically not affected the stress distribution in the BC. However tensile stress values decreased about 12% and compressive increased about 43% within the BC layer.

The stress response obtained by a combination of creep and plastic deformation within the TGO resulted in a stress distribution as shown in Fig. 5.31. However, the result does not differ much from the previous case and only the stress values were slightly affected. Here a maximum tensile stress of 845.6 MPa was obtained at the peak of BC, which is a reduction of 4.2 MPa in comparison with the reference case. However, the maximum tensile stress within the TGO has increased about 72.4 MPa to 983.2 MPa. Moreover the tensile stress values decreased about 13% in the BC. In contrast the compressive stresses increased within this layer about 37%. Additionally, tensile stress level increased about 28% in the TGO, but compressive stress values decreased about 38%. Furthermore in the TBC the tensile and compressive stress level decreased about 60% and 39%, respectively.

As general remark the TGO creep results in a geometrical instability of the oxide layer manifested by an inhomogeneous TGO thickness and the interface shape which slightly rescales from a perfect sinusoidal form. Additionally the tensile stresses in the TGO were always located at the peak. Moreover, the creep of TGO reduced in both presented studies the maximum stress level in the TBC layer in comparison with the reference case. However considering additionally to creep of TGO plastic deformation the tensile stresses in the TGO increased. As the stress level within the TBC was lower

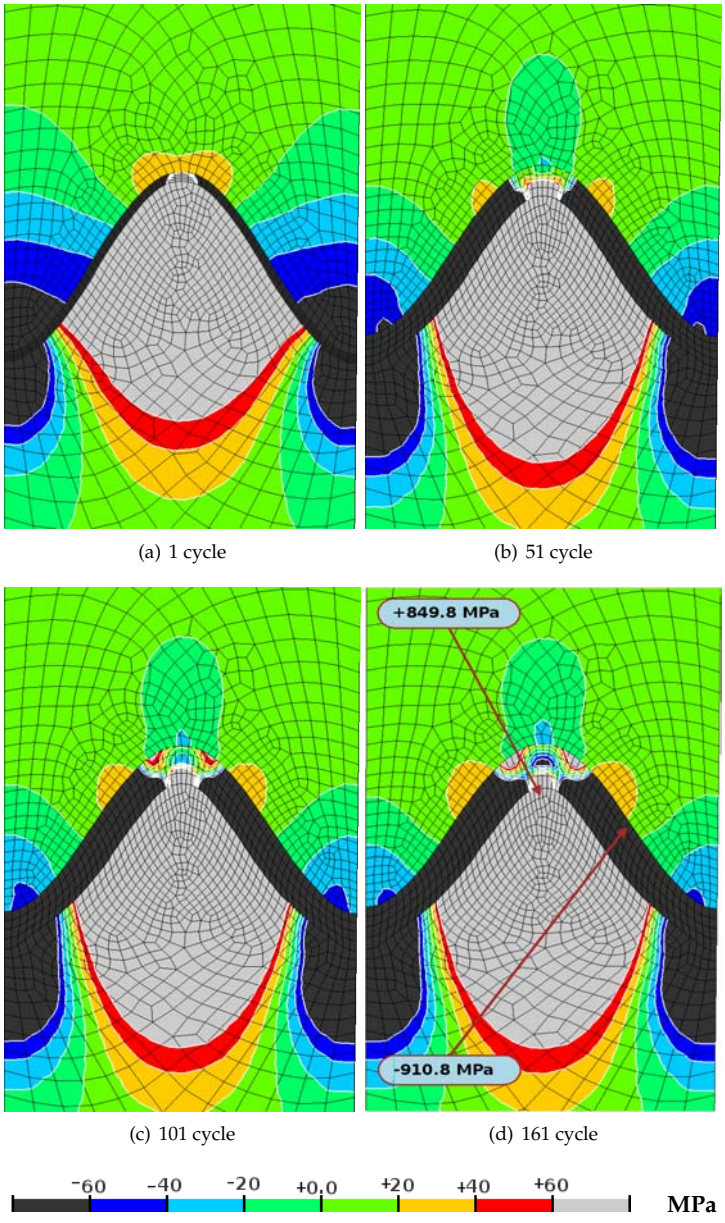


(a) 1 cycle (b) 51 cycle

(c) 101 cycle (d) 161 cycle

Figure 5.30: Calculation with reference parameter set, but additionally with TGO creep.

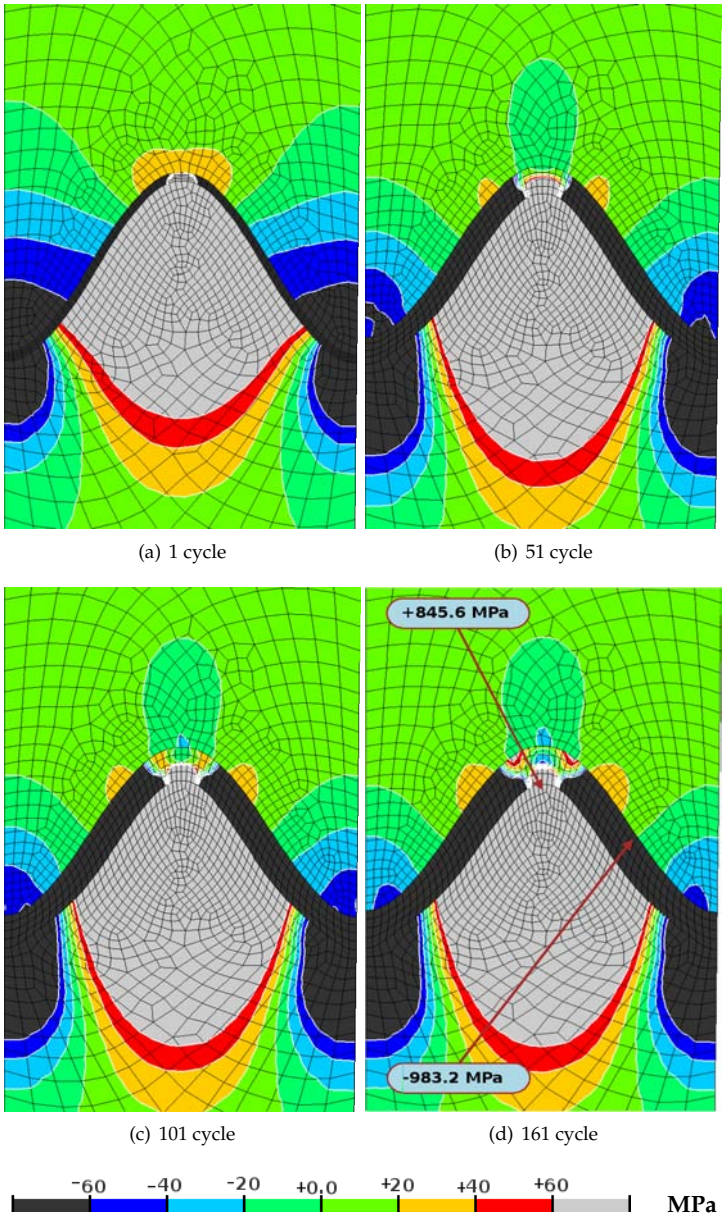


(a) 1 cycle (b) 51 cycle

(c) 101 cycle (d) 161 cycle

Figure 5.31: Influence of creep and plastic behavior of the TGO on radial stresses development.

one can conclude that creep relaxation of the TGO should be very beneficial for a TBCs lifetime.

### 5.2.6 Influence of base material creep

Creep data of Ni-based superalloys have been intensively investigated in the past. The creep data of CMSX-4, published by Pindera [40] served as a basis for the following simulation. Creep of the base material is assumed in the temperature range from $750^oC$ to $1050^oC$. All other parameters remained as in the reference case.

Fig. 5.32 shows the radial stress distribution at the end of 1st, 51st, 101st and 161st cycle in the vicinity of BC/TGO/TBC interface. The stress development looks very similar to the calculation without creep of the base material as it was for the reference case (section 5.1.6.2). The maximum and minimum values of stresses have only slightly decreased (less than 1%). Based on this result one can conclude that a parameter with such a small influence does not justify its implementation in a complex FE-simulation, as calculation time is increased and converging of the model becomes more critical.

### 5.2.7 Influence of lateral TGO growth

In this section the influence of oxide layer lengthening on the stress field development is studied. Two cases are considered, namely without and with 20% lateral out-of-plane oxidation. As it was explained in section 5.1.6.2, the reference case was calculated assuming 5% of lateral oxidation. Therefore, here in this section, only the differences in stress development due to different rate of lateral oxidation in comparison with the reference case will discussed.

As a first case, the simulation of stress development in absence of lateral oxidation is analyzed. The results are shown in Fig. 5.33. The stresses in the TBC layer were the most affected. Already after the first cycle tensile stress values at off-peak regions in the TBC were higher in comparison with the reference case. Contrary to the reference case, where tensile stresses above 20 MPa formed a continuous path from off-valley regions to the boundaries of the unit cell, in current case the tensile zones were smaller and have not formed such paths. Additionally the compressive zones in the TBC were bigger in size. During cycling these tensile zones at off-peak regions expanded in a horizontal direction and the compressive stress level at valleys decreased. Moreover, the tensile stress level within this layer after 161 cycles was slightly lower (about 1%) compared to the reference case. Furthermore, the compressive stresses in the TBC increased about 11%.

The stress distribution in the TGO layer was practically the same as in the reference case. Only the tensile stress level has increased about 24% , but compressive stress values decreased (10%). The same is true for the BC layer where tensile and compressive stresses decreased about 1% and 5%, respectively.

The impact of 20% lateral oxidation increase, modeled as an elongation of the elements in lateral direction has an influence on increasing the amplitude of TBCs as-

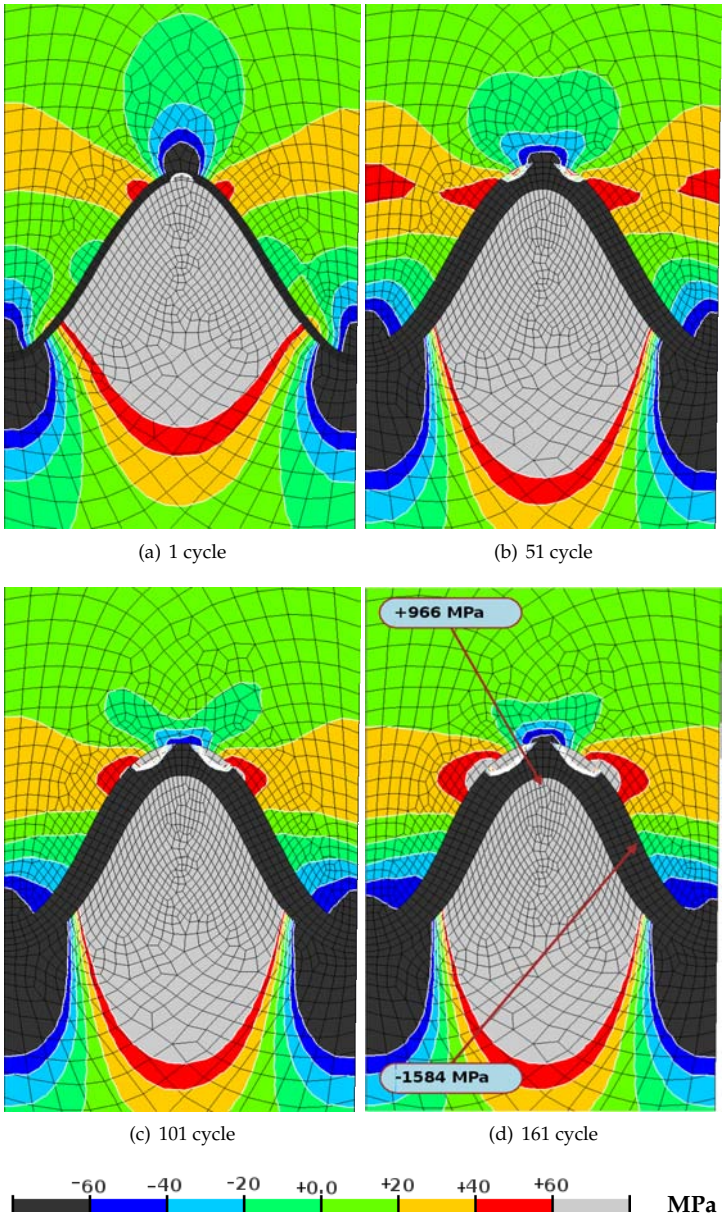


(a) 1 cycle (b) 51 cycle

(c) 101 cycle (d) 161 cycle

Figure 5.32: Simulation of influence of base material creep on stress development. All stresses are in MPa.

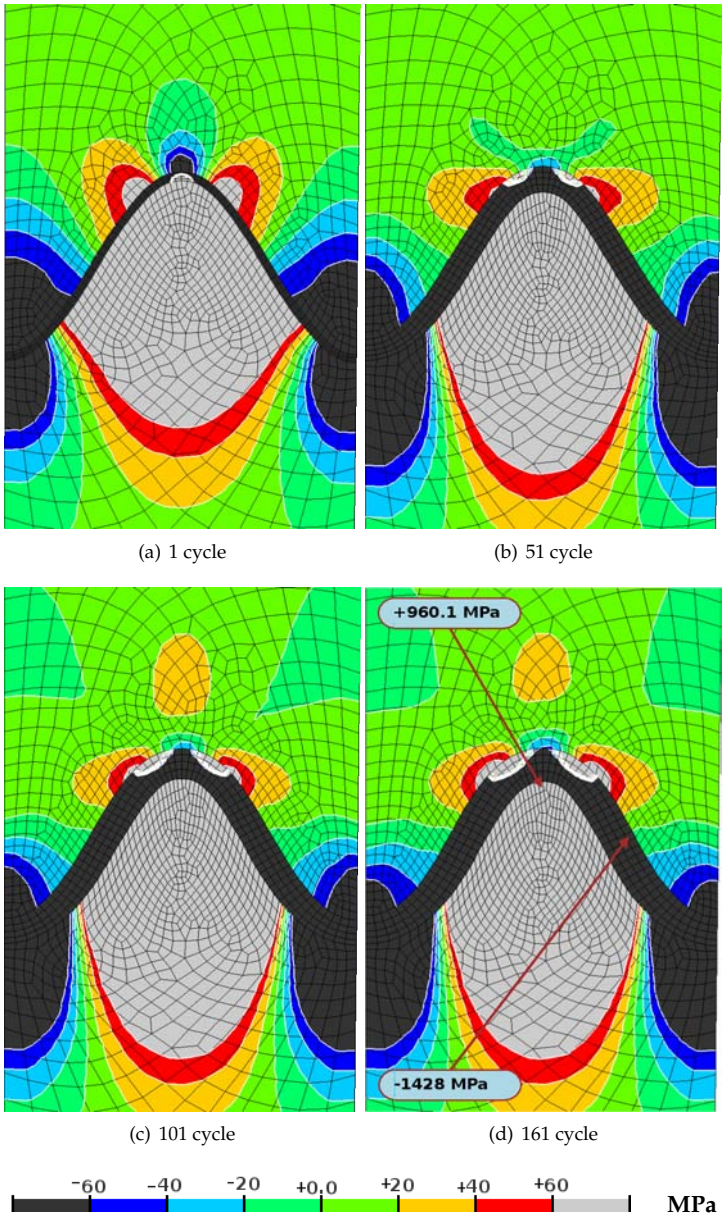


(a) 1 cycle (b) 51 cycle

(c) 101 cycle (d) 161 cycle

Figure 5.33: Development of radial stress distribution in absence of lateral oxidation.

perity (Fig. 5.34). Within the TBC layer one can notice larger tensile stress zones at off-peak and valleys regions in the TBC at the 1st cycle Fig. 5.34(a) compared to the reference case. The bottom of the valleys and the peak region are under compression stresses. During the first 50 cycles the tensile stress zones at off-peak region have expanded and occupy the complete regions above the valleys Fig. 5.34(b). With continued cycling this expansion process of the tensile zones goes on. However, after 161 cycles the stress level significantly increased; in the TBC about 40% and more than 50% in the case of tensile and compressive stresses respectively, compared to the unmodified case.

In TGO layer stress development was similar to the reference case. After 161 cycles the tensile stress level decreased about 2%, but tensile stress values slightly increased (1.3%) within the TGO.

The stress distribution within the BC is rather the same as in all previous examples. The maximal tensile and compressive stress values in radial direction are indicated in Fig. 5.34(d). In contrast to the increase of the tensile stress values in the BC about 6% after 161, cycles the compressive stress level slightly decreased (1%) in comparison with the reference simulation.

It has been shown that lengthening of the TGO is directly related to stress development in TBCs by increase in the amplitude of the interface roughness. Moreover, it promoted the creation of bigger tensile stress paths in the TBC layer above valleys from off-peak regions to the boundaries of the unit cell, going into the TGO. Based on the current studies of lengthening influence on stress development, one can conclude, that to increase the lifetime of TBCs , lateral oxidation should be at a very low level.

### 5.2.8 Influence of roughness amplitude and wavelength

As the previous section revealed a negative influence of the amplitude increasing during cycling, now the influence of the interface shape itself is studied. Amplitude and wavelength parameterize the sinus function. This allows to modify the interface by changing these parameters.

#### 5.2.8.1 Sinusoidal interface with 30 $\mu m$ amplitude and 60 $\mu m$ wavelength

The reference model consists of a sinusoidal interface with an amplitude of 15 $\mu m$ and a wavelength of 60 $\mu m$. Here the influence of a rougher interface of 30 $\mu m$ amplitude is considered. As a result of roughness the increase areas occupied by compressive stresses at the valleys of the TBC were bigger after the first cycle, compared to the reference case (Fig. 5.35). Additionally, a larger compressive stress zone was obtained at the peak. Moreover the tensile stress paths from off-peak regions to the boundaries of the unit cell still exist as in the reference case. The tensile stress values in these paths were in range between 20 and 60 MPa. During cycling the compressive stress zones at valleys and at the peak of the TBC decreased and occupied smaller areas. On the other hand the tensile and compressive stress values increased after 161 cycles in comparison with the reference case in the TBC about 11% and 8%, respectively.

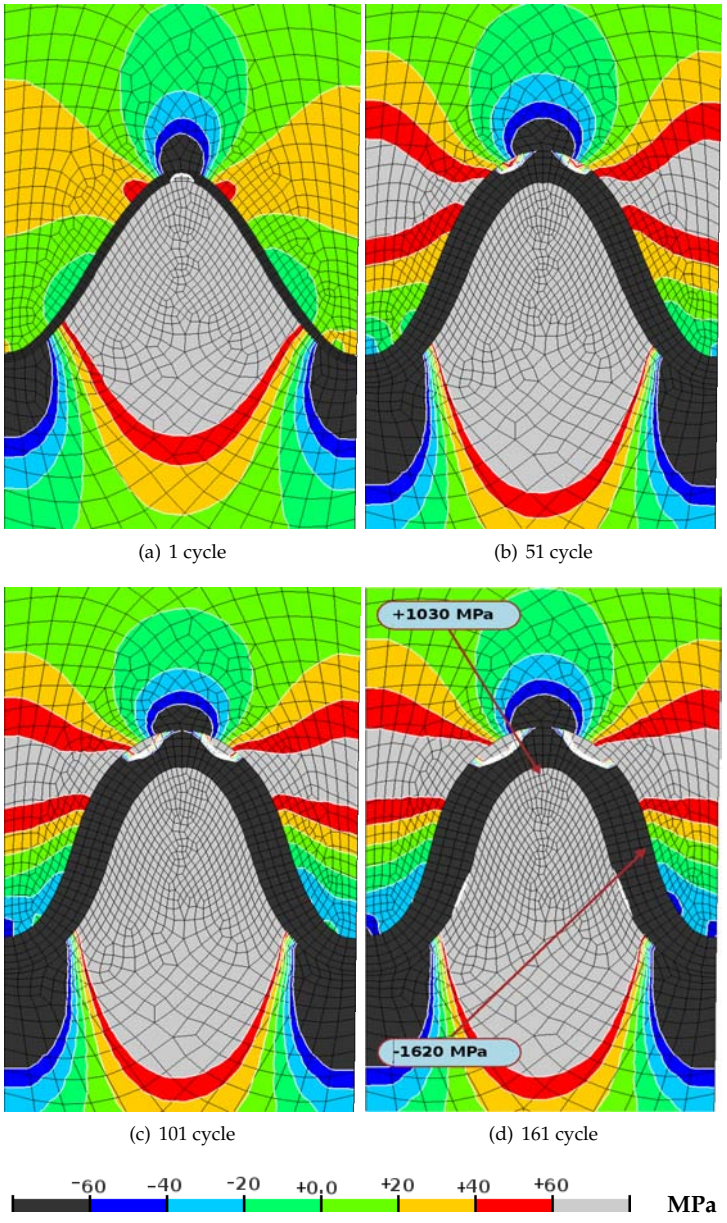


(a) 1 cycle (b) 51 cycle

(c) 101 cycle (d) 161 cycle

Figure 5.34: Calculation with the reference parameter set with higher (20%) lateral oxidation and its influence on radial stress development.

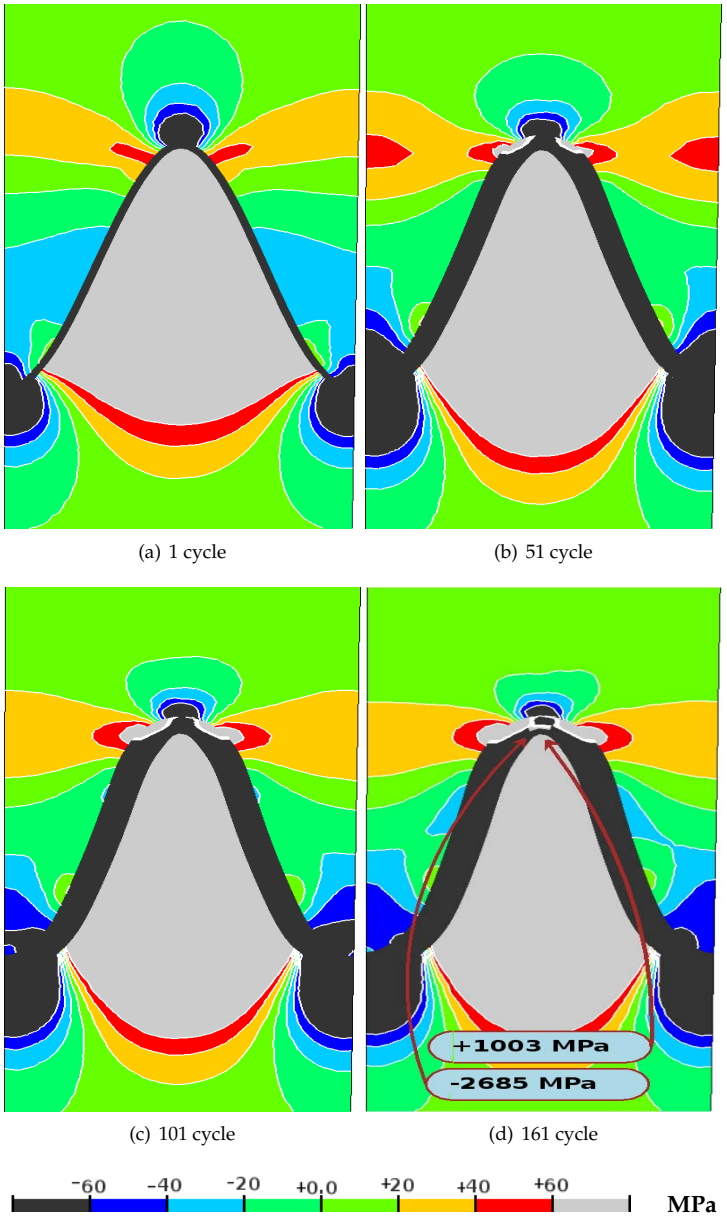


Figure 5.35: Influence of higher (30 $\mu m$) interface amplitude on stress development, the other parameters were consider as in the reference calculations. To better visualize the stress distribution the mesh was removed.

Contrary to the reference case the TGO layer was fully under compressive stresses after the first cycle. Additionally during cycling large tensile zones were obtained at off-peak regions in the TGO layer Fig. 5.35(b). These tensile zones have expanded and the values of tensile stresses increased. Moreover a 3'rd tensile zone was obtained between the 101'th and 161st cycle at the peak of asperity in the TGO layer. These zones formed a continuous tensile zone within TGO above the peak. Taking into account tensile paths within the TBC , a non interrupted tensile zone all over the modeled area became apparent partially in the TGO and in the TBC. Furthermore, the stress level in the TGO increased about 170% and 70% in the case of tensile and compressive stresses, respectively, compared to the reference case.

The stress distribution within the BC was again not significantly influenced by this parametric modification of the model. However tensile stresses slightly increased (3.5%) in the BC, but compressive stresses decreased about 1.5%.

It can be concluded, that as consequence of higher roughness of $30\mu m$ interface a complete tensile stress path above the valleys in the TBC and partially in the TGO is formed and could lead to the often experimentally observed black and white failure [16; 26; 50].

#### 5.2.8.2 Sinusoidal interface with 15 $\mu m$ amplitude and 30 $\mu m$ wavelength

Here the same interface shape and amplitude were considered as in the reference case, with however a shorter wavelength of only 30 $\mu m$.

Fig. 5.36 shows the stress distribution in radial direction it the vicinity of the asperity. As a results of shortening the wavelength of the interface high tensile stresses developed in the TBC above valleys after the 1st cycle. However, during cycling the tensile zones decreased in size (Figs. 5.36(b) -. 5.36(d)). Instead these tensile zones in the valleys and above developed higher compressive stresses during cycling as in the reference case. After 161 cycles the tensile stress level in the TBC decreased less than 1% in contrast to compressive stresses which increased about 62%.

The wavelength also affected the stress development in the TGO. After the 1st cycle the TGO was fully under compression as in the case above (increase in an amplitude of roughness). Thickening of the TGO resulted in additional formation of tensile zones at the middle regions in the TGO next to the BC (Figs. 5.36(b) -. 5.36(d)). Furthermore at the middle of the thickness in the TGO at the peak of asperity a small tensile zone was also formed. The stress level in the TGO significantly increased during cycling and after 161 cycles the tensile and compressive stresses increased about 218% and 80%, respectively, compared to the reference case.

The stress distribution in the BC was similar to the reference case. However, tensile stress values in the BC increased (1.2%), but compressive decreased about 20%.

It has been presented, based on this simulation, that a shorter wavelength combined with a reference value of amplitude did not create a continuous possible tensile path within the TGO. Such paths were not present in the TBC after 161 cycles neither.

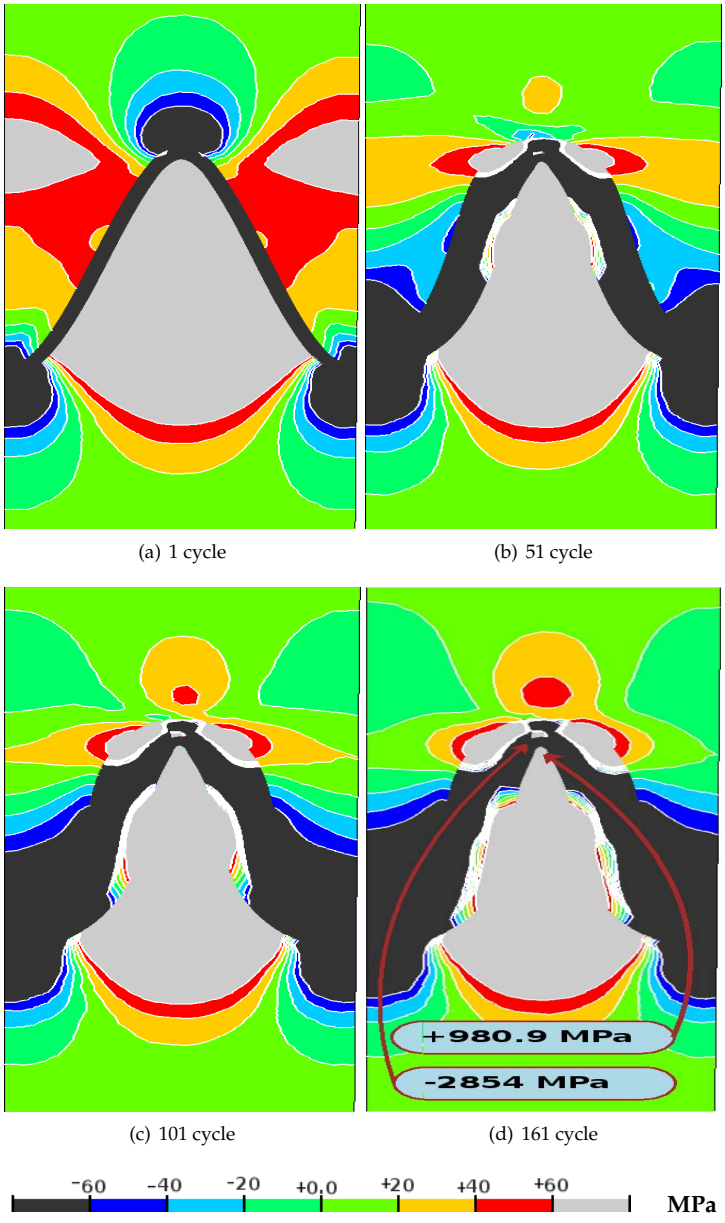


(a) 1 cycle (b) 51 cycle

(c) 101 cycle (d) 161 cycle

Figure 5.36: Calculation with reference parameter set considering shorter wavelength of interface. To better visualize the stress distribution the mesh was removed from picture view.

#### 5.2.8.3 Sinusoidal interface with 15 $\mu m$ amplitude and 90 $\mu m$ wavelength

Increasing the wavelength flatters the interface of the asperity and by that influences the stress development in the TBCs. In Fig. 5.37 the radial stress distribution was shown for selected number of cycles (1st, 51st, 101st, and 161st). The tensile stresses in the TBC obtained already after the first cycle were lower than in the reference case and areas occupied by stresses above 20 MPa were significantly smaller (Fig. 5.37(a)). Moreover, compressive stresses were also lower. However due to thickening of the oxide layer the tensile stress zones and values of these stresses significantly increased and occupied bigger areas in the TBC (Figs. 5.37(b) -. 5.37(d)) compared to the reference case. Although, comparing the tensile stress level of the current and reference simulation showed a decrease of stress values about 33%. Moreover compressive stresses increased (11%) in comparison with reference case.

In the TGO the stress distribution after the first cycle was similar as in the reference case. Contrary to the reference simulation due to thickening of the TGO the off-peak tensile stresses within the TGO were not obtained and the TGO remained under compression up to the end of simulation. In addition tensile and compressive stress level decreased about 77% and 18%, respectively.

In the BC no major changes in stress distribution were obtained compared to the reference calculation. However, the tensile stresses level decreased about 25% ,but compression stress level slightly increased (less then 1%) in comparison with the reference case. As a result of such a simulation, maximal radial tensile stress of 727.3 MPa was obtained after 161 cycles and was lower than in the reference study.

One can remark that the roughness is one key parameter which influences stress development in TBCs. In the case of a sinusoidal interface of 15 $\mu m$ amplitude and 60 $\mu m$ wavelength no additional tensile zones at the peak in the middle of the TGO was introduced as it was the case of a rougher interfaces (Fig. 5.14). However, the same amplitude with a shorter wavelength promotes compressive zones at valleys and flanks in the TBC. It was shown that an increase of wavelength decreases the stress level in TBCs, as the interface is getting flatter.

To optimize the shape of the interface for modeling proposes one shall fit the interface by a geometrical function which best fit to the shape obtained from a SEM picture. Additionally this function should depend on at least two variables such as amplitude and wavelength. Moreover to emphasize the important limit of an amplitude increase here, once again is recalled, that higher increase of tensile stress values in the TBC were obtained in the case of rougher interface from all studied variations of different values of amplitude and wavelength. Therefore, the amplitude should not be increased, but the wavelength could be the optimization parameter. It was shown that increasing the wavelength decreases all radial tensile stresses in TBCs as it was discussed above.

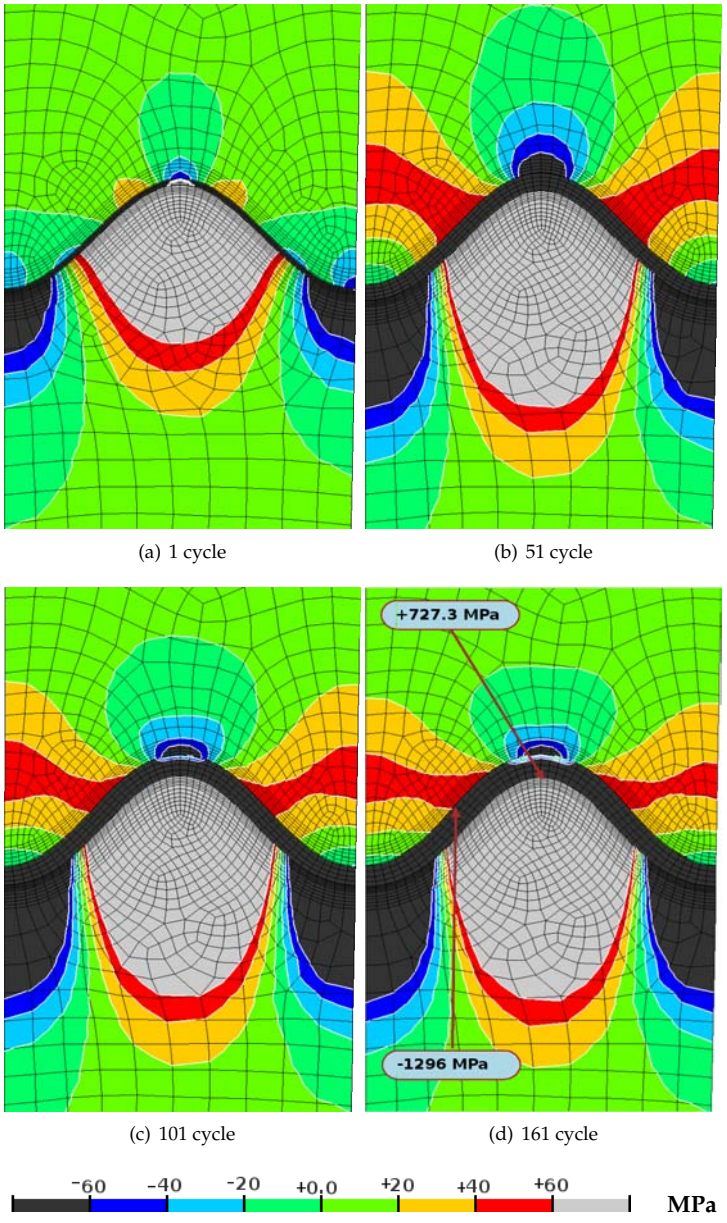


(a) 1 cycle (b) 51 cycle

(c) 101 cycle (d) 161 cycle

Figure 5.37: Influence of a longer wavelength (90 $\mu m$) on stress development.

### 5.2.9 Influence of different shapes of the interface

A real interface of an APS-TBC does not consist of a perfect sinusoidal shape with well defined wavelength and amplitude. Due to the manufacturing process it has a highly irregular interface roughness. Reproducing a real interface shape in a model would increase the effort to generate a suitable mesh and would further result in far too long calculation times. For these reasons, the interface was idealized. In order to still get some insight of the influence of different interface shapes the present section shows results of two different examples, namely a semicircle and a semielliptic interface.

#### 5.2.9.1 Semicircle interface with 15 $\mu m$ amplitude and 60 $\mu m$ wavelength

As a first interface variation a semicircle interface with 15 $\mu m$ amplitude and 60 $\mu m$ wavelength is modeled. These parameters are equivalent to the reference model with sinusoidal interface. The two models only differ in the shape of the interface.

The results of this FE simulation are shown in Fig. 5.38. Mainly the TBC layer was affected by the change of the interface shape. The valleys of the TBC layer were occupied by compressive stresses after the 1st cycle. At the peak compressive stresses were found. However the areas from boundaries of the unit cell to off-peaks were occupied by tensile stresses. Additionally bigger tensile stresses were concentrated at the boundaries of the unit cell above valleys. As the thickness of the oxide layer increased the tensile and compressive stress values in the TBC also increased (Fig. 5.38(b)). However, the compressive stress zones at the peak first increased than decreased again. Furthermore, the stress level in the TBC increased about 50% and 35% in the case of tensile and compressive stresses respectively in comparison with the reference simulation.

In the TGO after the first cycle the stress development was similar to the reference case. Moreover the tensile zones at the peak regions next to TBC decreased slower than in the reference case. However, between the 101st and 161st cycle the tensile stresses at the peak switched to compression. At the off-peak regions small tensile zones were formed instead after 161 cycle. The maximum tensile stress level decreased in the TGO decreased about 71% compared to the reference case, but the compressive stresses increased (32%).

The BC still exhibited tensile stresses at the peak and compressive stresses at the valleys as in the reference case. Although, stress level in the BC decreased about 9% in the case of tensile stresses and 19% in the case of compressive stresses in comparison with the reference simulation.

#### 5.2.9.2 Semielliptic interface with 15 $\mu m$ amplitude and 90 $\mu m$ wavelength

Consequently the present section shows the results of a second interface variation. The semielliptic interface was achieved by simply increasing the wavelength of the previous semicircle interface.

The stress development is shown in Fig. 5.39. In the TBC layer compressive stresses were found at valley and at off-peak regions after the first cycle. The other areas

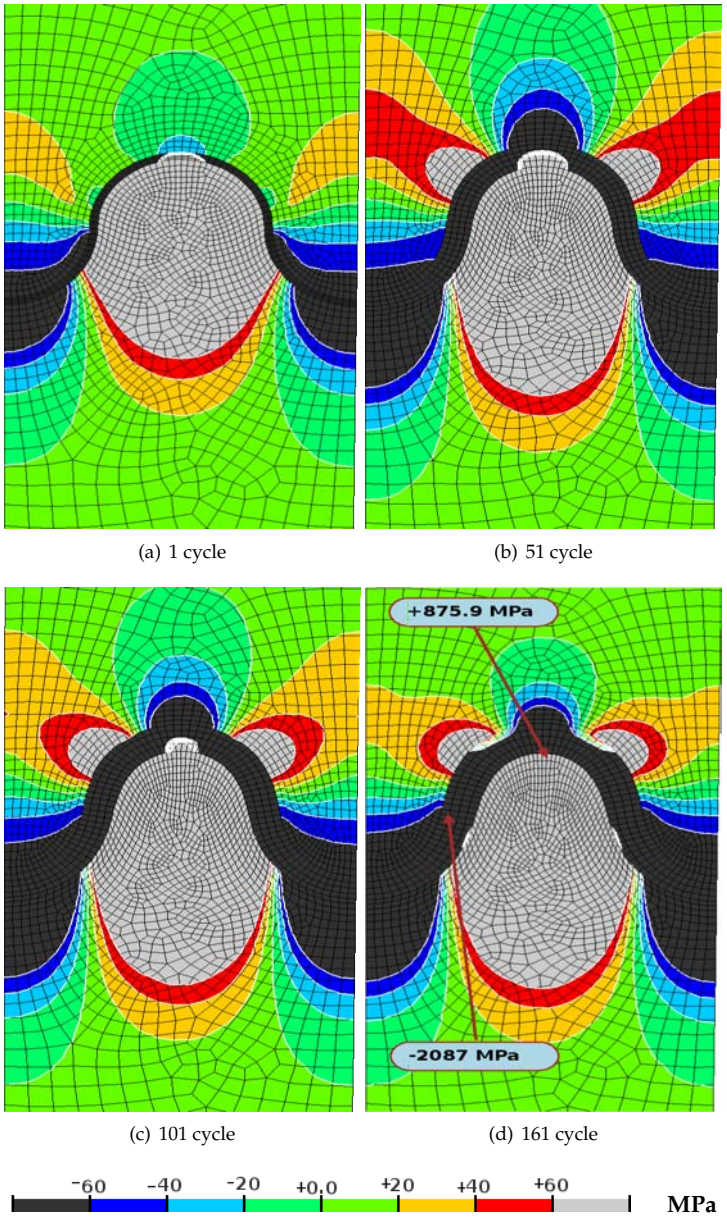


(a) 1 cycle (b) 51 cycle

(c) 101 cycle (d) 161 cycle

Figure 5.38: Radial stress distribution, with consideration of the BC/TBC interface modeled as semicircle. All other parameters remained as in the reference case.

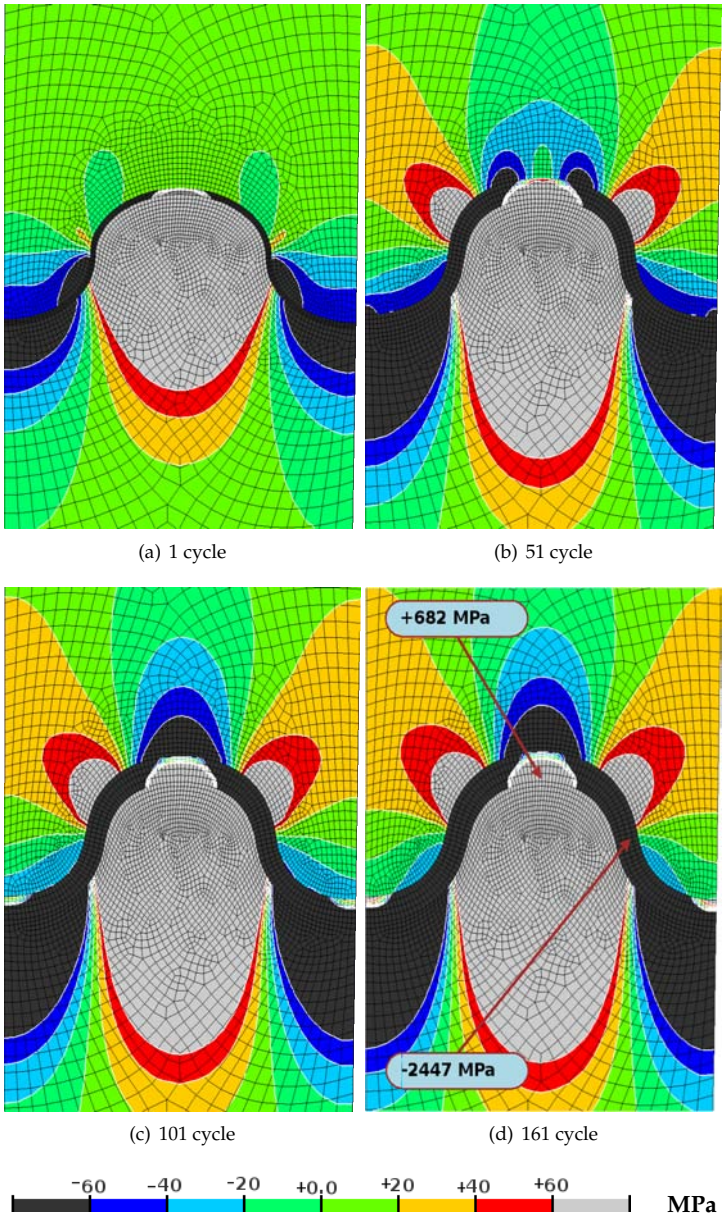


(a) 1 cycle (b) 51 cycle

(c) 101 cycle (d) 161 cycle

Figure 5.39: Calculation with reference parameter set with consideration of the BC/TBC interface modeled as semielliptic.

were occupied by tensile stresses. These tensile stress zones have increased during cycling. However the compressive stresses at valleys in TBC decreased. The compressive stresses at the peak in the TBC were obtained at around 50 cycles and increased during further cycling. The final stress distribution (after 161 cycles) was similar as in the previous case. The tensile stresses above valley were higher and areas occupied by these stresses were broader compared to the semicircle and the reference cases. The tensile and compressive stresses increased about 107% and 23%, respectively compared to the reference case. However in comparison with the previous case the tensile stresses increased about 38%, but compressive stresses decreased about 9%.

In the TGO a tensile stresses development was similar as in the previous case (semicircle) up to 101 cycles. The main difference in stress development was seen at valley region next to the TBC layer. In these regions after 101 cycles the tensile stress zones were formed and increased during the next 50 cycles compared to the previous and the reference cases. Contrary to the previous and the reference cases the tensile stresses at off-peak regions were not obtained, instead the peak was still under tension. However, tensile stress level increased about 166% compared to the reference case and was also 9 times higher than in the previous case. Furthermore, the compressive stress values increased about 55% and 18% compared to the reference and the semicircle cases, respectively.

In the BC the stress development was similar as in the reference and semicircle cases. However the tensile stress level decreased about 37% and 30% in the reference and semicircle cases respectively. Furthermore, compressive stress level decreased by 30% compared to the reference case and by 14% in comparison with the previous calculation.

#### 5.2.9.3 Concluding Remarks

The present section could prove that the shape of the interface has an influence on stress development. Considering the semicircle interface the maximum values of tensile stresses were lower than with sinusoidal asperity. However the elliptic interface introduced the lowest maximal tensile stresses in TBCs. Additionally, due to lateral oxidation the elliptic interface changes the shape in order to become a more semicircle interface. Disadvantage of the elliptic interface is the tensile stress development at the peak of the TGO. In case of a semicircle interface the tensile stresses at the peak in TGO have switched to compressive during cycling. Additionally, the compressive stresses at valleys in the TBC decrease faster than with a semicircle interface.

### 5.2.10 Long term stress development

Several models correlate the lifetime of TBCs to the thickness of TGO. The simulations presented in previous sections were performed up to the 161st cycle, which corresponds to a TGO thickness of $5.7\mu m$. In the present section, this simulation with the reference parameter set is continued up to 621 cycles ($Thickness^{TGO}_{cycle=621} = 8.6\ \mu m$). The stress distribution at the end of 166, 301, 441, and 621 cycles are shown in Fig. 5.40. The maximum tensile stresses of 1023 MPa obtained after the 621st cycle at the peak of the BC do not differ much from the respective values after the 161st cycle (969.1 MPa). However significantly bigger (about 116%) tensile stress zones developed after 621 cycles in the TGO layer at off-peak positions compared to the reference case after 161 cycles. During cycling these tensile stress zones have increased with the result that a small link of tensile stresses appeared between these two stress zones, close to the interface with the TBC. The compressive stress level also increased about 215% after 621 cycle in compression with the reference case after 161 cycle. Additionally at off-valley regions close to the BC the development of tensile zones was observed beyond the 301st cycle. Within the TBC compressive stresses concentrated at the valleys. During cycling the values of these stresses (19%) increased compared to the 161st cycle. Also the peak of TBC was occupied by a growing compressive stress zone. The tensile stress zones at off-peak regions in the vicinity of the TGO layer also increased about 41% after 621 cycles in comparison with the reference case after 161 cycles.

The FE simulation could prove that an increase of TGO thickness by further cycling generates higher tensile and compressive stresses. Additionally, a continuous tensile stress path from the tip of the TGO over off-peak of the TBC to the flanks becomes always present at an high enough cycle number. As a result, a crack can follow the tensile paths and propagate above valleys in the TBC layer. Tendencies in the development of the tensile zones suggest that tensile stresses at off-peak regions in the TBC would attract cracks, which are formed in the TGO.

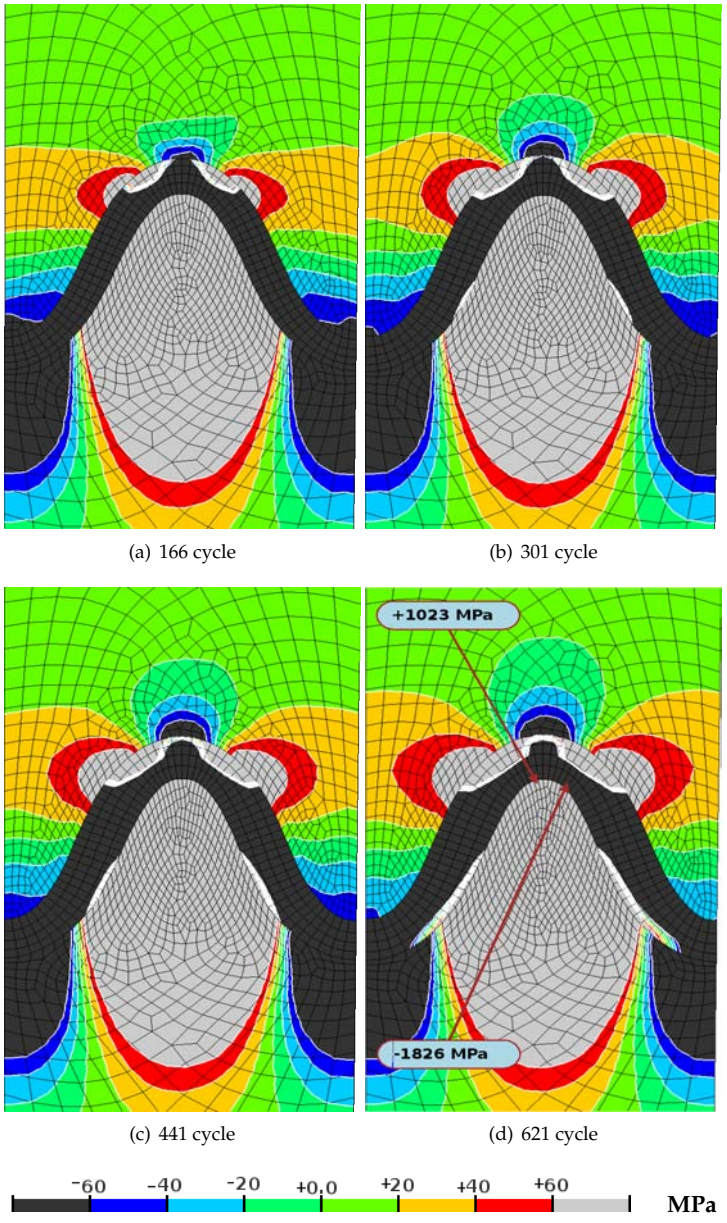


(a) 166 cycle (b) 301 cycle

(c) 441 cycle (d) 621 cycle

Figure 5.40: Radial stress distribution at selected number of cycles with reference parameter set.

## 5.3 Damage simulations at the peak of the TGO/BC interface

It has been observed that cracks were acquired at the TGO/BC interface. Therefore a crack was placed between the TGO and BC layer at the tip of asperity and has been modeled as cohesive zone. Details concerning cohesive zone modeling are given in chapter 3.2.1. 36 elements were modeled as cohesive zone elements giving a predefined crack path that follows exactly the TGO/BC interface.

Fig. 5.41(a) shows the stress distribution after the 1st cycle in the vicinity of BC/TGO/TBC interface with two different scales of stresses. The radial stress field, plotted in the range between -250 and 250 MPa emphasizes the stress redistribution due to crack growth. The stress field after the 1st cycles looks similar to the reference case. As the TGO thickness increased tensile stresses in the TBC also increased. Moreover, bigger tensile stresses were found at the off-peak regions in the TBC. When the crack was initiated at the 19'th cycle at the peak of the cohesive zone, the stresses redistributed around the crack due to softening of TGO/BC interface. By the crack initiation it has been understood that the stiffness of cohesive element was reduced to the level of TGO stiffness. In other case the interface acts as a rigid element because the stiffness was assumed to be very high in comparison with TGO stiffness. During continued cycling the tensile stress zone at the peak in the TGO was diminished. Instead, two tensile zones at the off-peak close to the TBC layer were obtained Fig. 5.41(b). Due to the formation of the crack at the 19'th cycle two additional tensile stresses zones were found at the crack tip in the TGO. Moreover, at the peak in the BC lower tensile stresses (below 200 MPa) were obtained, which is an effect of crack formation and propagation along the TGO/BC interface. As the crack propagated further tensile stress zones at the off-peaks in the TBC decreased. However compressive stresses at the valleys in the TBC increased. Maximum tensile stresses of 1198 MPa were found at middle part of the TGO, and maximum compressive stresses of -1492 MPa were found at the peak of the TGO layer as indicated in Fig. 5.42(b).

The full spallation of TBCs has not been simulated yet, because the crack was placed at the tip of the TGO/BC interface and a crack path following the interface is not most realistic. However stress redistribution due to crack formation and propagation was obtained and presented. The unsymmetrical stress distribution (Fig. 5.41(d)) in the BC is a result of the high mesh sensitivity of cohesive elements. Additionally, the crack formation and propagation is sensitive to critical shear energy release rate. Therefore a reliable data set of critical energy release rate in normal and shear direction is a basic requirement to properly model the crack. Moreover, the stiffness of cohesive elements plays an important role of the stress development in the cohesive zone and by that crack initiation.

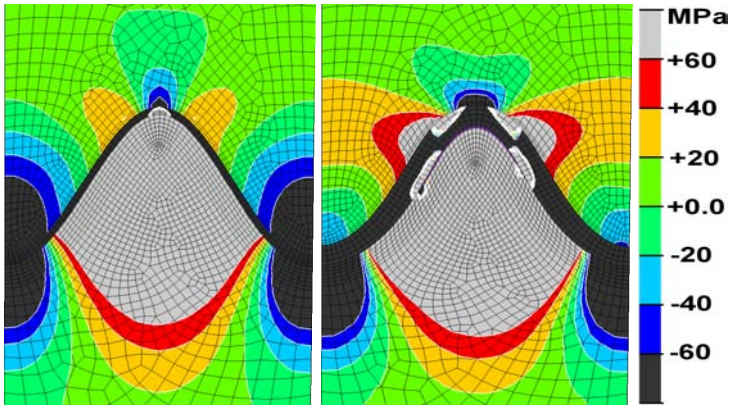


(a) 1 cycle (b) 51 cycle

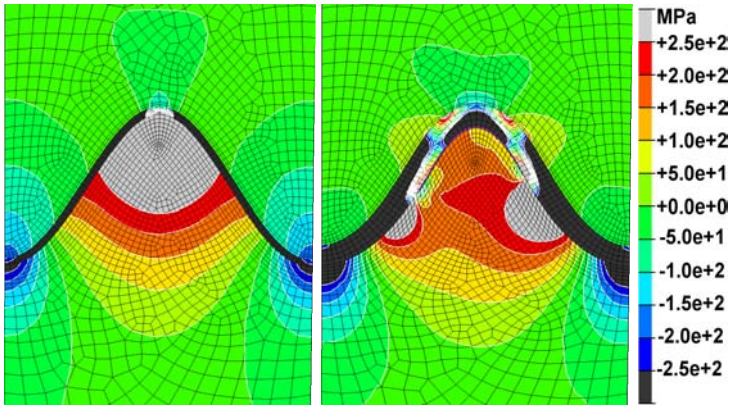


(c) 1 cycle (d) 51 cycle

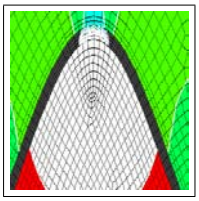

(e) Zoom of cohesive region after 1st cycle

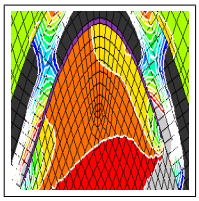

(f) Zoom of crack after 51 cycles

Figure 5.41: Radial stress distribution with continuous oxidation at 1st and 51st cycle, with consideration of crack formation and propagation at the BC/TGO interface modeled as cohesive zone. Other parameters remained unchanged as in the reference case.

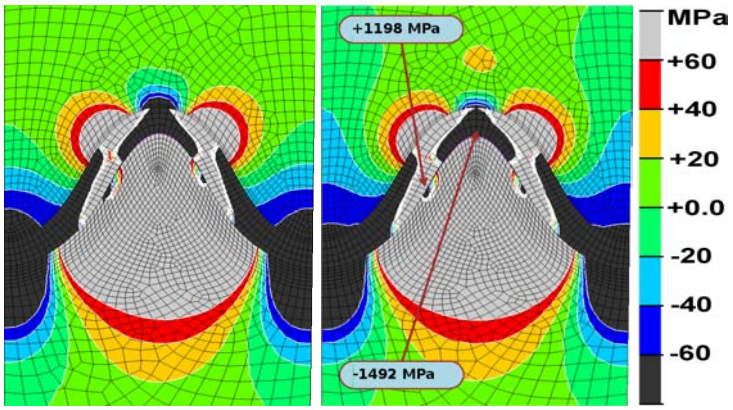


(a) 101 cycle (b) 161 cycle

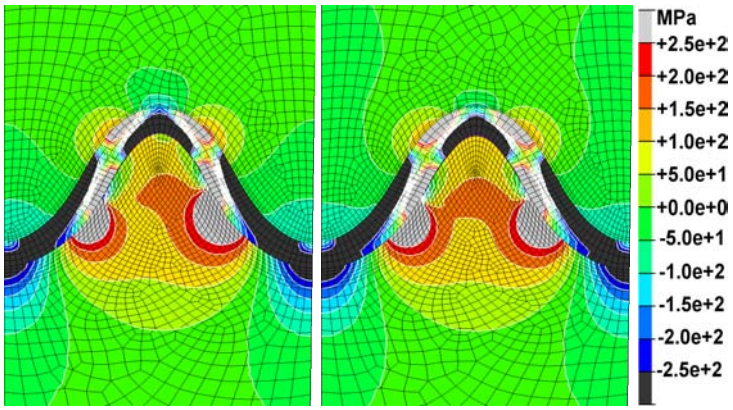


(c) 101 cycle (d) 161 cycle

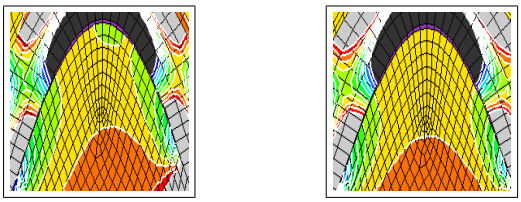

(e) Zoom of crack after 101 cycle (f) Zoom of crack after 161 cycle

Figure 5.42: Radial stress distribution with continuous oxidation at 101st and 161st cycle, with consideration of crack formation and propagation at the BC/TGO interface modeled as cohesive zone. Other parameters remained unchanged as in the reference case.

# Discussion and Conclusions

The investigation of stress development in TBC systems due to thermal cycling with dwell time at high temperature, including BC oxidation is discussed in this chapter and conclusions will be drawn. Generally, the FE results were assessed on the basis of the distribution of radial stresses in the vicinity of the TGO at the end of a cycle at RT. The assessment and the conclusion was done with respect to local regions near and in the TGO with high tensile stresses, which could lead to crack formation or crack propagation (critical sites). At first the development of the reference parameter set is discussed and after that the systematic parameter variations and the simulation of crack formation and crack growth is addressed.

### Influence of oxidation

The results presented in chapter 4.4.2 show that modeling of the TGO thickness with different but constant values compared to simulation of continuous TGO growth (with and without lateral oxidation) does not reflect the behavior of a real TBC system under thermal cyclic loading conditions with oxidation, as the stresses were underestimated due to neglecting of oxide growth strains in the TGO layer. Additionally, the lengthening of the oxide layer (lateral TGO growth) resulted in an increase of amplitude and in a significant expansion of the tensile stress zones and increase of tensile stresses in the vicinity of interface. This implies that the lateral oxidation plays an important role and can not be neglected. In other words, any numerical simulations of TBCs should at least, consider oxidation as a continuous process and include lateral growth (lengthening).

### Influence of material properties

Furthermore, it was shown that the continuous oxidation leads principally to unrealistic high stresses in all three materials, if only elastic properties are taken into account.
➦**Influence of plastic behavior of the bond coat**
We found that for the sinusoidal interface radial tensile stresses are concentrated at the tip of the BC due to plastic behavior of the bond coat with consideration of out-of-plane oxidation, including 5% of lateral oxidation. In addition, in the case of BC plasticity the stress conversion from tensile to compressive, at the tip of the BC, has not been obtained during TGO thickening. This was observed in the purely elastic

case with also the same value of lateral oxidation. Furthermore, an increase of areas occupied by radial tensile stresses in the TBC from off-peak regions to the boundaries of the unit cell was observed and its values were bigger.

➦**Influence of plastic behavior of the TGO**

However, when we considered only plastic behavior of the TGO and oxidation of the BC geometrical instabilities of the oxide layer appeared (the TGO layer lost its perfectly sinusoidal shape). Nevertheless, the stress level significantly decreased by about 75% and 64% in BC and TGO layer, respectively, but in the TBC the stress values decreased only by about 5% (5.1.3) in comparison with the purely elastic calculation considering continuous oxidation.

➦**Influence of plastic behavior of the BC and the TGO**

Taking into account plastic deformation of both, the BC and the TGO layer, the geometrical instabilities of the interface shape were more pronounced in the TGO, even though the stress values decreased due to additional stress redistribution via plastic deformation in the TGO. Finally, it can be concluded that the purely elastic case overestimates tensile and compressive stresses, and that a plastic redistribution decreases the stresses significantly.

➦**Influence of the BC creep behavior**

By considering creep behavior of the BC instead of plastic behavior with TGO plasticity and continuous oxidation including of 5% lateral oxidation it was shown that the tensile stress zones in TBC above the valleys were developing slower and the maximum tensile stress value was lower by about 11%. The slower development of tensile zones should have a positive effect on the lifetime of TBCs. Contrary to this the maximum tensile stress value at the peak in the BC was higher by about 14%.

➦**Influence of the TBC creep behavior**

We have also shown that by including TBC creep, the stresses in TBC layer further relaxed (decreased by about 85%) and geometrical instabilities resulting from BC and TGO plasticity were stabilized. In contrast to this the creep of the BC does not stabilize the instabilities.

It was observed during close inspection of the first and the second cycle, that higher tensile and compressive stresses developed at high temperature mainly at off-valley regions of the TBC by considering a temperature value of $200^oC$ at which the stress free state occurs. Furthermore, the maximum tensile stress value in the TBC layer at the end of dwell time at high temperature during the first cycles was 31% higher than the maximum value of stress at the end of dwell time at RT, as oxidation dominates stress development during the first cycles. This proved that, the assumption of a stress free state at high temperature used by other authors [4; 42; 44] is not fully correct as the system is not able to fully relax the stresses.

Based on these results it can be concluded that a realistic simulation of the stress response of TBCs requires realistic data including at least a) BC and TGO plasticity, b) BC and TBC creep, c) oxidation kinetics (and its implementation as a continuous process), and d) a correct assumption of stress free state.

It was shown that consideration of the above mentioned parameters (reference case) resulted in radial tensile stresses concentrated at the peak in the BC. Moreover,

in the TGO, tensile stresses from off-peak to off-peak were obtained. Next to this tensile zone in the TGO a continuous tensile path above valleys in the TBC was also obtained and always present. Furthermore, the peak and valley regions of the TBC were under compression. These tensile paths in the TGO and in the TBC confirmed experimental findings of TBCs fracture (see Fig. 6.2(c)).

➦**Influence of the thermal expansion coefficient (TEC)**

A number of material properties modifications, have been studied (chapter 5.2) based on the reference case. It was demonstrated that increasing the TEC in the TBC layer increased the tensile stresses above valleys. Furthermore, increasing the TEC in the base material has shown that tensile stress values above valleys in the TBC were higher (about 52%) which could promote crack formation and its growth in the TBC. However, an increase of the TEC in the BC resulted in an increase of the compressive zone at valleys in the TBC layer (more than 200%), which could have a positive effect on lifetime by acting as a crack stopper. Contrary to this positive effect, the negative influence was also observed as an increase of about 60% in the tensile stresses at the TGO/BC interface was obtained.

However, other modifications of the TEC have shown possible benefits for the stress response of the TBCs component: It was shown that the compressive stress zones at valleys in the TBC were increased and its maximum stress values increased by about 126% and 43% in the case of decrease of the TEC of the TBC and CMSX-4, respectively. However, the tensile stresses at the TGO/BC interface have slightly increased by about 3% and 4% due to the decrease of the TEC in the TBC as well as in the base material, respectively, and as small variations these effects can be neglected. By decreasing the TEC in the BC, tensile stresses in the TBC decreased by about 21%, although they occupied fully the valleys. However, these tensile stresses were small (below 66 MPa) and the TBC layer might resist crack formation.

➦**Influence of the TBC stiffness**

In this thesis the sintering effect in TBC was not considered. Instead, the variations of stiffness and its influence on stress response was studied. In chapter 5.2.2, it was shown that a stiffness increase of the TBC promote continuous radial tensile stress zones from off-peak regions to the boundaries of the FE unit cell in the TBC (these stresses increased by about 142%). However, the maximum tensile and compressive stress values decreased in the BC by about 4% compared to the reference case (5.1.6.2). On the other hand the TBC profit from a more porous TBC layer, because the tensile stresses in TBC were lower (about 67%) than in the reference case. It was manifested by the fact that the tensile stresses within the continuous tensile path from off-peaks to the boundaries of the unit cell above the valleys in the TBC were mostly below 10 MPa. In contrast to that an increase of the stiffness results in a slightly increase by about 1.5% and 2% of the maximum tensile and compressive stress values, respectively, in the BC compared to the reference. Therefore, it can be neglected, as it is very small and the BC is rather stress resistant. It is proposed that higher porosity in the TBC should be introduced and lower sintering kinetics, if possible. This has proved that porosity is an important factor in the aimed improvment of TBCs.

The more porous TBC can be achieved by a new method of manufacturing TBC

layer which was proposed by Jadhava et al. 2005 [29]. This method is a further development of the *Air Plasma-Sprayed* method and is based on a *Solution-Precursor-Plasma-Spray*. The new coating has higher porosity and lower thermal conductivity than conventional APS-TBCs.

The present work was intended to give an answer on the questions: i) is a soft *Bond Coat* better or not, and ii) is a soft *Thermal Barrier Coating* better or not with particular regard to the deformation resistance at high temperature (creep resistance). The answers to these questions are demonstrated by the results obtained from variations of creep rates in bond coat (5.2.3.1) and in thermal barrier coating (5.2.3.2).

➦**Influence of a soft or creep resistant BC**

The results obtained show that higher creep rates in the BC resulted in lower maximum radial tensile and compressive stress values in TBCs in comparison with the reference case. However, broader tensile stress paths in the TBC above the valleys of the asperity were observed in comparison with the reference case. Moreover the stress development in the TBC layer was only slightly affected by an increase or decrease of creep rates of BC compared to reference case. The stress field in the BC was mostly affected in form of higher tensile stresses (about 13%), obtained with lower creep rates. One can conclude that higher creep rates help to keep low stress values in TBCs. However, the small sensitivity of different creep rates in BC on stress development in the TBCs has shown that neither a significant positive nor negative influence on the lifetime can be extrapolated. It can thus be concluded that the importance of the creep behavior of the BC has been overestimated in the past.

➦**Influence of a soft or creep resistant TBC**

Studies of TBC creep rate variations on stress development were also considered. It was shown that higher creep rates in the TBC layer mainly led to a lower stress level in the TBC layer. Moreover, the maximum tensile and compressive stress values decreased in the BC and TGO compared to the reference case and should be beneficial for the lifetime of TBCs.

Finally it can be concluded that lower creep rates of the TBC were not profitable for TBCs. As stresses could not relax fast enough to prevent the development of a large tensile stress path (stress values increased about 120% in comparison with the reference case) above the valleys in the TBC and these tensile paths in the TBC could be a reason for a lower lifetime of TBCs.

➦**Influence of the TGO creep**

However, it was shown that not only lower creep rates of the TBC were promoting a geometrical instability of the TGO. Also TGO creep resulted in a geometrical instability of the oxide layer. The radial tensile stresses were always concentrated at the peak. Additionally a significant decrease of the stress level in TBCs in comparison with the reference case indicates that creep relaxation of the TGO should be very beneficial for a TBCs lifetime.

➦**Influence of the base material creep**

The effect of base material creep on stress development in the TBCs was demonstrated in chapter 5.2.6. Here, it was shown that creep of base material affected only marginally the stress development in TBCs for the case of pure thermal cycling with

dwell-time at high temperature. Since the effect was small (below 1% decrease of stresses), its implementation in a complex FE-simulation does not seem to be justified, when only thermal cycling and no TMF strains are taken into account.

➦**Influence of higher (20%) lateral growth of the TGO**

In the case of higher lateral oxidation rate (5.2.7) stress values in TBCs were larger. It was obtained that higher values of lateral oxidation promote a lateral tensile path above valleys in TBC and by that a possible crack could be promoted more easily than in case of lower rate of lateral oxidation. Therefore, out-of-plane and lateral oxidation rates should be minimized.

### Influence of interface roughness and shape

However, not only the material properties of TBCs, affect the stress development. Also the interface shape plays an important role, as the interface is directly affected by oxidation of the bond coat.

The challenge is to give the answer to the question, what kind of interface should be manufactured or would rather be preferable, to obtain lower stresses or a longer lifetime.

➦**Influence of interface roughness**

It was shown in chapter 5.2.8.1 that in the case of a rougher interface (30 $\mu m$ instead of 15 $\mu m$ amplitude and 60 $\mu m$ wavelength) additional radial tensile stresses were obtained at the peak in the TGO and created a continuous radial tensile path within TGO. This was not obtained in the reference case. Moreover, it was shown that tensile stress values above valleys in the TBC increased by more than 10% in comparison with the reference case.

➦**Influence of a shorter wavelength of the interface**

However, the same amplitude as in the reference case (15 $\mu m$) with a shorter wavelength ( 30 $\mu m$ ) resulted in an expansion of compressive zones at the valleys and above them in the TBC by decrease of tensile zones. Additionally, the tensile stress level in the TBC slightly decreased, but compressive stress values in the TBC increased by 62%. Furthermore, the maximum tensile stress located at the peak in the BC slightly increased (only by about 1%).

➦**Influence of a longer wavelength of the interface**

Moreover it was demonstrated (5.2.8.3), that an increase of wavelength decreases the stress level in TBCs, as the interface is getting flatter.

As it was discussed above that the tensile stress values in the TBC layer increased due to an increase of amplitude or lateral oxidation (by about 10% and 38%, respectively). Additionally it was shown that higher amplitude resulted in a continuos tensile path at the peak within the TGO. Section 5.2.8.3 demonstrated that increasing the wavelength decreases the radial tensile stresses in the TBC layer to values of about 55 MPa. However, these low tensile stresses occupied almost fully the valleys. Decreasing the wavelength leads generally to bigger tensile stresses in the TGO. This was manifested by increase of maximum tensile and compressive stress values by about 220% and 80%, respectively, in the TGO. Contrary to this large changes the tensile

stress level in the BC at the peak slightly increased. Furthermore, the tensile zones in the TBC layer occupied significantly smaller areas and its values were slightly lower. In addition the continuous path within the TGO was not present as it was in the case of rougher interface. Therefore, the amplitude should not be increased, but the wavelength could be the optimization parameter.

➦**Influence of interface shape**

Considering the semicircle interface, as shown in chapter 5.2.9, the maximum value of tensile stresses was lower than that for a sinusoidal asperity. Increasing the wavelength of this semicircle interface resulted in a semielliptical interface. This modified interface with increased wavelength introduced the lowest maximum tensile stresses in TBCs. We found that, due to lateral oxidation the elliptical interface changes the shape in order to became a more semicircle interface. It was also demonstrated that in the case of semielliptical interface the maximum radial tensile stress concentrated always at the peak of the TGO as it is indicated in Fig. 5.39(d) (+682 MPa). Contrary to this, in the case of a semicircle interface the tensile stresses at the peak in the TGO switched to compressive during cycling. An other important finding is, that the compressive radial stresses at valleys of the TBC decreased faster in the case of a semielliptic interface than with a semicircle interface.

It can be concluded that as a strategy to optimize the shape of the interface one shall fit the interface by a geometrical function which best approximates the shape obtained from a SEM-micrographs. Additionally, this function should depend at least on two variables such as $A_h$ - amplitude and $\lambda_w$ - wavelength $f(A_h, \lambda_w)$.

Due to these variations a ratio which can characterize the stress development for different interface shapes is postulated as $\xi = \frac{\int_{S_a}^{S_b} C(s)ds}{\lambda_w}$, where $\int_{S_a}^{S_b} C(s)ds$ is the length on interface shape and $\lambda_w$ is the wavelength . Such a representation facilitates the understanding of stress development as the $\xi$ parameter differentiates between a variety of interfaces ( Fig. 6.1).

### Influence of a long term cyclic oxidation loading on stress development

Additionally it was shown during long term simulation (5.2.10) that thickening of the TGO led to permanent presence of continuous radial tensile paths above valley in the TBC and a continious increase of the tensile stress values in this path. As a result, a crack can follow the tensile paths and propagate above valleys in the TBC layer. Such a crack could be further attracted by radial tensile stresses at off-peak region in the TGO and propagate through TGO creating spallation. This finding confirmed experimental evidence of frequently observed failure cracks in TBCs.

Concentration of the maximum radial tensile stresses at the tip in the BC next to the TGO was obtained for the reference calculation and in all varied parameters. Thus a simulation of crack formation at the BC/TGO interface by cohesive zone elements was carried out 5.3.

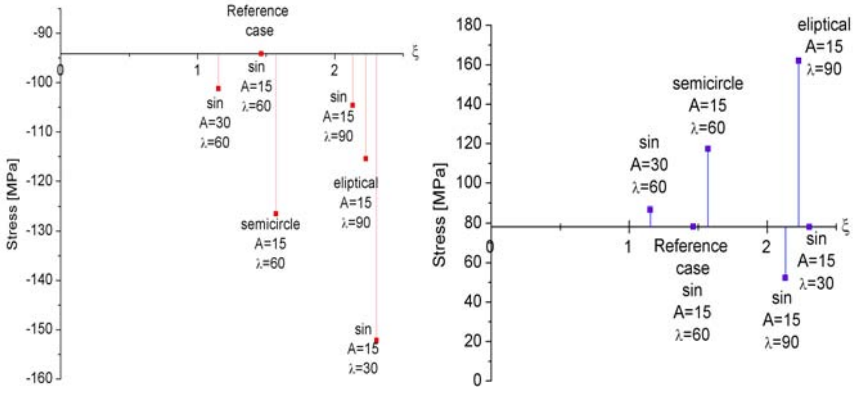


(a) compressive (b) tensile

Figure 6.1: Maximum radial stress values in the TBC layer after 161 cycles as a function of dimensionless $\xi$ parameter. The horizontal axis position indicates the stress values for the reference case.

### Influence of crack formation at the BC/TGO interface on stress development

We have found that due to the formation of a crack (at the BC/TGO interface) radial tensile stresses at peak of asperities were redistributed. In our case the first micro-cracks have been formed during cooling from $121^oC$ to RT at an early stage (19'th cycle). This was manifested by a significant decrease of the stiffness of the cohesive zone elements to a level of TGO stiffness and it was visualized as additional displacement (at the BC/TGO interface) in Fig. 5.41(d). Moreover, at the peak in the BC lower tensile stresses (below 200 MPa) were obtained, which is an effect of micro-crack formation and propagation along the TGO/BC interface. Furthermore it was shown that tensile stress paths across the TGO layer were present (Fig. 6.2(a)). This particularly confirmed experimental evidence that cracks are not only present at peak of the BC/TGO interface, but can also cross the TGO and penetrate TBC above valleys (Fig. 6.2(b) and Fig. 6.2(c)) [26].

Additionally inspection of stress development during crack formation and propagation revealed an unsymmetrical stress distribution (Fig. 5.44(e)) in the BC, which is a result of the high mesh sensitivity of cohesive elements. Furthermore the crack formation and propagation is sensitive to critical shear energy release rate. These findings show that proper modeling of crack requires reliable data of critical energy release rate in normal and shear direction. Moreover, the stiffness of cohesive elements is thought to play an important role in the stress development in the cohesive zone. Based on this study it is suggested that the stiffness of cohesive elements at BC/TGO interface should be slightly higher than the TGO stiffness.

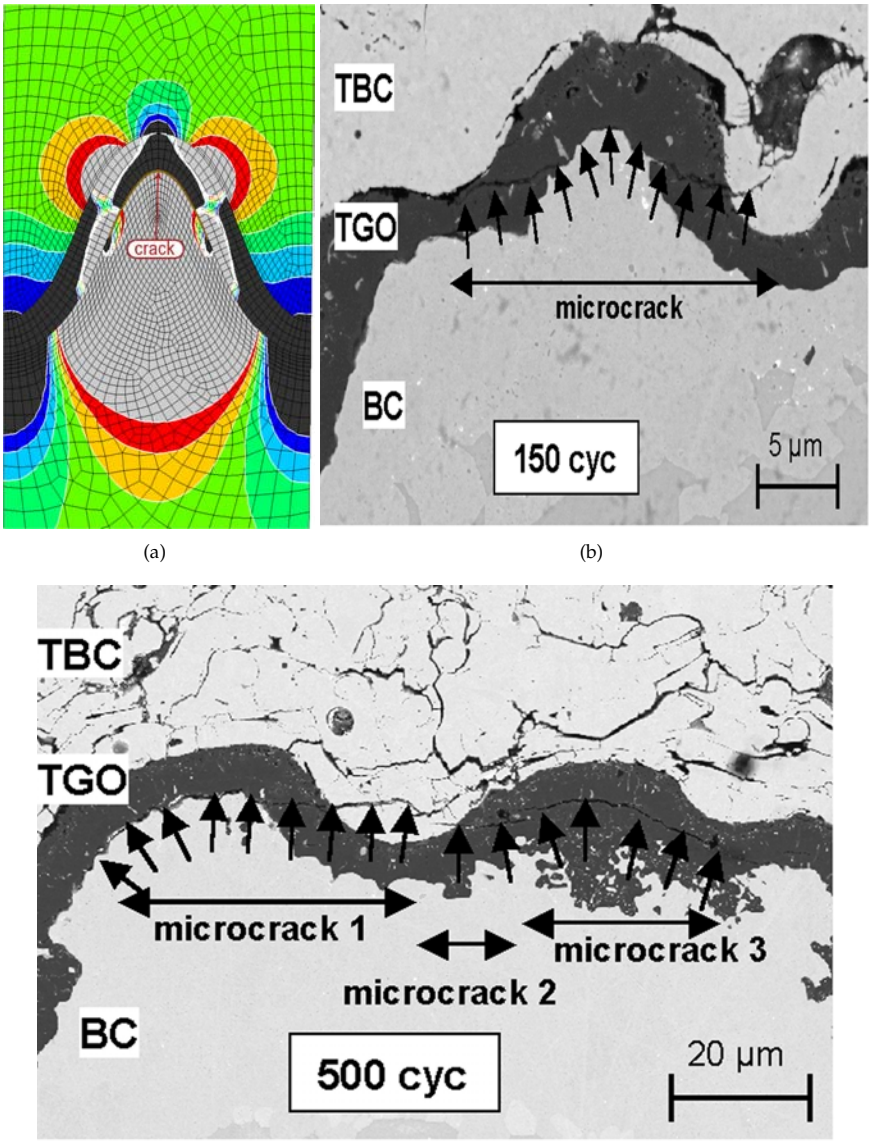


Figure 6.2: Numerically calculated and experimentally observed cracks in APS-TBC [26]

Finally, it can be concluded that the performed FE simulations of the stress response at the metal ceramic interface of plasma-sprayed TBCs provide the prediction of critical sites for crack formation along the roughness profile and predict the trends with respect to the direction of crack growth (crack propagation path). Furthermore, the FE simulations were used as a basis for analyzing and assessing the parameters, which affect the stress response qualitatively as well as quantitatively (Tabs.1 - 11) and can thus be used to improve the properties of the coating materials.

From the results obtained, one can take the final conclusion that the set of parameters such as: 1) the time dependent material properties of the TBC and TGO, 2) the oxidation kinetics, particularly with regard to lateral oxidation, and 3) the shape of the interface play the crucial role in the stress development during thermal cycling. Against the background of this finding variations of other parameters can almost be neglected.

# Appendix A

Detailed quantitative assessment of all calculations. The sequence of the tables is identical to the sequence of the respective chapters.

Table 1: The maximum tensile and compressive stress values for different TGO thickness and interface shapes obtained for all three layers after cooling from $200^oC$ to RT. All layers were purely elastic.

| Interface shape | TGO thickness $[\mu m]$ | BC layer $\sigma_{max}$ [MPa] | BC layer $\sigma_{min}$ [MPa] | TGO layer $\sigma_{max}$ [MPa] | TGO layer $\sigma_{min}$ [MPa] | TBC layer $\sigma_{max}$ [MPa] | TBC layer $\sigma_{min}$ [MPa] |
|---|---|---|---|---|---|---|---|
| Sinusoidal | 0.5 | 102.9 | -71.15 | 29.64 | -313.3 | 4.528 | -5.969 |
| Semicircle | 0.5 | 23.2 | -16.68 | 16.83 | -442.9 | 4.019 | -7.002 |
| Sinusoidal | 2 | 39.62 | -28.55 | 80.79 | -258.4 | 3.79 | -4.457 |
| Semicircle | 2 | 64.01 | -39.1 | 46.74 | -390.8 | 1.994 | -4.328 |
| Sinusoidal | 5 | 171.5 | -97.27 | 94.95 | -185.6 | 5.322 | -10.95 |
| Semicircle | 5 | 114 | -63.66 | 84.41 | -286.9 | 5.953 | -5.297 |

Table 2: The maximum tensile and compressive stress values and their differences ($\Delta\sigma_j^i = \frac{\sigma_j^i - \sigma_j^i|_{sin(\delta=5\mu m)}}{\sigma_j^i|_{sin(\delta=5\mu m)}}$, where: i=BC,TGO,TBC; j=min,max; $\sigma_j^i|_{sin(\delta=5\mu m)}$ taken from Tab. 1 for sinusoidal interface) obtained for all three layers after the last simulated cycle at RT are compared to stress values obtained for sinusoidal interface of $5\mu m$ TGO thickness. The continuous out-of-plane oxidation of the BC was assumed. All stress values are in MPa

| | BC layer $\sigma_{max}$ | BC layer $\sigma_{min}$ | TGO layer $\sigma_{max}$ | TGO layer $\sigma_{min}$ | TBC layer $\sigma_{max}$ | TBC layer $\sigma_{min}$ |
|---|---|---|---|---|---|---|
| without lateral oxidation | 4120 | -20100 | 27890 | -31080 | 1712 | -3236 |
| $\Delta\sigma_j^i$[%] | 2302 | 20564 | 29273 | 16646 | 32068 | 29453 |
| 5% of lateral oxidation | 15390 | 14820 | 1811 | -16390 | -49290 | -2452 |
| $\Delta\sigma_j^i$[%] | 8874 | 16750 | 15508 | 26457 | 33929 | 22293 |

Table 3: The maximum tensile and compressive stress values obtained for all three layers after the last simulated cycle at RT. In all simulations the continuous out-of-plane oxidation including 5% lateral oxidation was considered.

| Comments | Material properties | | | | BC layer | | TGO layer | | TBC layer | |
|---|---|---|---|---|---|---|---|---|---|---|
| | BC layer | | TGO layer | TBC layer | $\sigma_{max}$ | $\sigma_{min}$ | $\sigma_{max}$ | $\sigma_{min}$ | $\sigma_{max}$ | $\sigma_{min}$ |
| | Creep | Plastic | Plastic | Creep | [MPa] | [MPa] | [MPa] | [MPa] | [MPa] | [MPa] |
| | | ✓ | | | 820.1 | -360.2 | 25370 | -40460 | 3118 | -3029 |
| | | | ✓ | | 3877 | -2465 | 5306 | -5101 | 1726 | 1133 |
| | | ✓ | ✓ | | 1040 | -4532 | 231.9 | -2404 | 540.6 | -438.2 |
| | ✓ | | ✓ | | 1183 | -716.9 | 165.6 | -2147 | 481 | -562.4 |
| | ✓ | ✓ | ✓ | | 963.3 | -439.5 | 310 | -2439 | 491.7 | -541.3 |
| | | ✓ | ✓ | ✓ | 1091 | -470.4 | 177.3 | -1730 | 79.76 | -997.6 |
| Reference case | ✓ | ✓ | ✓ | ✓ | 969.1 | -399.5 | 266.2 | -1585 | 78.21 | -94.14 |

Table 4: The maximum tensile and compressive stress values and their differences ($\Delta\sigma = \frac{\sigma_j^i - \sigma_j^i|_{Ref.case}}{\sigma_j^i|_{Ref.case}}$, where: i=BC,TGO,TBC; j=min,max; $\sigma_j^i|_{Ref.case}$ taken from Tab. 3 for the reference case) obtained for all three layers after the last simulated cycle at RT are compared to stress values obtained for the reference case. Only variations of thermal expansion coefficient are shown other properties remained as in the reference case.

| Variation TEC | Layer | BC layer | | | | TGO layer | | | | TBC layer | | | |
|---|---|---|---|---|---|---|---|---|---|---|---|---|---|
| | | $\sigma_{max}$ [MPa] | $\Delta\sigma$ [%] | $\sigma_{min}$ [MPa] | $\Delta\sigma$ [%] | $\sigma_{max}$ [MPa] | $\Delta\sigma$ [%] | $\sigma_{min}$ [MPa] | $\Delta\sigma$ [%] | $\sigma_{max}$ [MPa] | $\Delta\sigma$ [%] | $\sigma_{min}$ [MPa] | $\Delta\sigma$ [%] |
| A 50% higher | BC | 1547 | 60 | -420 | 5 | 321.3 | 21 | -2414 | 52 | 112.3 | 44 | 155.1 | -265 |
| A 50% lower | BC | 109.8 | -89 | -278.2 | -30 | 331.7 | 25 | -1496 | -6 | 61.66 | -21 | -35.37 | -62 |
| A 50% higher | TBC | 947 | -2 | -414.3 | 4 | 132.5 | -50 | -1706 | 8 | 91.53 | 17 | -159.6 | 70 |
| A 50% lower | TBC | 991.8 | 2 | -383 | -4 | 413.5 | 55 | -1462 | -8 | 99.45 | 27 | -213.1 | 126 |
| A 50% higher | CMSX-4 | 805.1 | -17 | -532.9 | 33 | 417.8 | 57 | -1572 | -1 | 119.1 | 52 | -92.5 | -2 |
| A 50% lower | CMSX-4 | 1001 | 3 | -270.5 | -32 | 174.5 | -34 | -1651 | 4 | 34.11 | -56 | -134.3 | 43 |

Table 5: The maximum tensile and compressive stress values and their differences ($\Delta\sigma = \frac{\sigma_j^i - \sigma_j^i|_{Ref.case}}{\sigma_j^i|_{Ref.case}}$, where: i=BC,TGO,TBC; j=min,max; $\sigma_j^i|_{Ref.case}$ taken from Tab. 3 for the reference case) obtained for all three layers after the last simulated cycle at RT are compared to stress values obtained for the reference case. Only variations of stiffness of the TBC are shown other properties remained as in the reference case.

| Variation Stiffness | Layer | BC layer | | | | TGO layer | | | | TBC layer | | | |
|---|---|---|---|---|---|---|---|---|---|---|---|---|---|
| | | $\sigma_{max}$ [MPa] | $\Delta\sigma$ [%] | $\sigma_{min}$ [MPa] | $\Delta\sigma$ [%] | $\sigma_{max}$ [MPa] | $\Delta\sigma$ [%] | $\sigma_{min}$ [MPa] | $\Delta\sigma$ [%] | $\sigma_{max}$ [MPa] | $\Delta\sigma$ [%] | $\sigma_{min}$ [MPa] | $\Delta\sigma$ [%] |
| A 50% higher | TBC | 927.6 | -4 | -380.2 | -5 | 162.3 | -39 | -1496 | -6 | 189.4 | 142 | -232.7 | 147 |
| A 50% lower | TBC | 980.9 | 1 | -405.5 | 2 | 310.7 | 17 | -1742 | 10 | 25.87 | -67 | -69.34 | -26 |

Table 6: The maximum tensile and compressive stress values and their differences ($\Delta\sigma = \frac{\sigma_j^i - \sigma_j^i|_{Ref.case}}{\sigma_j^i|_{Ref.case}}$, where: i=BC,TGO,TBC; j=min,max; $\sigma_j^i|_{Ref.case}$ taken from Tab. 3 for the reference case) obtained for all three layers after the last simulated cycle at RT are compared to stress values obtained for the reference case. Only variations of creep are shown other properties remained as in the reference case.

| Variation Creep | Layer | BC layer | | | | TGO layer | | | | TBC layer | | | |
|---|---|---|---|---|---|---|---|---|---|---|---|---|---|
| | | $\sigma_{max}$ [MPa] | $\Delta\sigma$ [%] | $\sigma_{min}$ [MPa] | $\Delta\sigma$ [%] | $\sigma_{max}$ [MPa] | $\Delta\sigma$ [%] | $\sigma_{min}$ [MPa] | $\Delta\sigma$ [%] | $\sigma_{max}$ [MPa] | $\Delta\sigma$ [%] | $\sigma_{min}$ [MPa] | $\Delta\sigma$ [%] |
| A 1000 times higher | BC | 863.5 | -11 | -374.2 | -6 | 256.1 | -4 | -1373 | -13 | 73.62 | -6 | -79.27 | -16 |
| A 1000 times lower | BC | 1098 | 13 | -435.7 | 9 | 215.5 | -19 | -1705 | 8 | 76.64 | -2 | -96.53 | 3 |
| A 1000 times higher | TBC | 946.1 | -2 | -391.2 | -2 | 156.5 | -41 | -1621 | 2 | 71.81 | -8 | -76.42 | -19 |
| A 1000 times lower | TBC | 981.2 | 1 | -418.4 | 5 | 479.7 | 80 | -2156 | 36 | 172.5 | 121 | -242.5 | 158 |
| creep without plasticity | TGO | 849.9 | -12 | -573.9 | 44 | 252.5 | -5 | -910.8 | -43 | 39.01 | -50 | -51.41 | -45 |
| creep | TGO | 845.6 | -13 | -545.4 | 37 | 342 | 28 | -983.2 | -38 | 31.95 | -59 | -58.09 | -38 |
| creep | CMSX-4 | 966 | 1 | -396.9 | -1 | 258.5 | -3 | -1584 | 1 | 78.35 | 1 | -94.16 | 1 |

Table 7: The maximum tensile and compressive stress values and their differences ($\Delta\sigma = \frac{\sigma_j^i - \sigma_j^i|_{Ref.case}}{\sigma_j^i|_{Ref.case}}$, where: i=BC,TGO,TBC; j=min,max; $\sigma_j^i|_{Ref.case}$ taken from Tab. 3 for the reference case) obtained for all three layers after the last simulated cycle at RT are compared to stress values obtained for the reference case. Only variations of lateral oxidation are shown other properties remained as in the reference case.

| Variation lateral growth | BC layer | | | | TGO layer | | | | TBC layer | | | |
|---|---|---|---|---|---|---|---|---|---|---|---|---|
| | $\sigma_{max}$ [MPa] | $\Delta\sigma$ [%] | $\sigma_{min}$ [MPa] | $\Delta\sigma$ [%] | $\sigma_{max}$ [MPa] | $\Delta\sigma$ [%] | $\sigma_{min}$ [MPa] | $\Delta\sigma$ [%] | $\sigma_{max}$ [MPa] | $\Delta\sigma$ [%] | $\sigma_{min}$ [MPa] | $\Delta\sigma$ [%] |
| 0% | 960.1 | -1 | -381.2 | -5 | 331.4 | 24 | -1428 | -10 | 77.46 | -1 | -104.4 | 11 |
| 20% | 1030 | 6 | -395.2 | -1 | 260.5 | -2 | -1605 | 1 | 108.2 | 38 | -145.2 | 54 |

Table 8: The maximum tensile and compressive stress values and their differences ($\Delta\sigma = \frac{\sigma_j^i - \sigma_j^i|_{Ref.case}}{\sigma_j^i|_{Ref.case}}$, where: i=BC,TGO,TBC; j=min,max; $\sigma_j^i|_{Ref.case}$ taken from Tab. 3 for the reference case) obtained for all three layers after the last simulated cycle at RT are compared to stress values obtained for the reference case. Only variations of roughness and amplitude of sinusoidal interface (BC/TGO/TBC) are shown other properties remained as in the reference case.

| Amplitude | Wavelength | BC layer | | | | TGO layer | | | | TBC layer | | | |
|---|---|---|---|---|---|---|---|---|---|---|---|---|---|
| | | $\sigma_{max}$ | $\Delta\sigma$ | $\sigma_{min}$ | $\Delta\sigma$ | $\sigma_{max}$ | $\Delta\sigma$ | $\sigma_{min}$ | $\Delta\sigma$ | $\sigma_{max}$ | $\Delta\sigma$ | $\sigma_{min}$ | $\Delta\sigma$ |
| $[\mu m]$ | $[\mu m]$ | [MPa] | [%] | [MPa] | [%] | [MPa] | [%] | [MPa] | [%] | [MPa] | [%] | [MPa] | [%] |
| 30 | 60 | 1003 | 3 | -393.6 | -1 | 718 | 170 | -2685 | 69 | 86.72 | 11 | -101.2 | 7 |
| 15 | 30 | 980 | 1 | -323.1 | -19 | 845.6 | 218 | -2854 | 80 | 78.06 | 1 | -152.2 | 62 |
| 15 | 90 | 727.3 | -25 | -402.5 | 1 | 61.65 | -77 | -1296 | -18 | 52.28 | -33 | -104.6 | 11 |

Table 9: The maximum tensile and compressive stress values and their differences ($\Delta\sigma = \frac{\sigma_j^i - \sigma_j^i|_{Ref.case}}{\sigma_j^i|_{Ref.case}}$, where: i=BC,TGO,TBC; j=min,max; $\sigma_j^i|_{Ref.case}$ taken from Tab. 3 for the reference case) obtained for all three layers after the last simulated cycle at RT are compared to stress values obtained for the reference case. Only variations of the BC/TGO/TBC interface shape are shown other properties remained as in the reference case.

| Shape | Amplitude | Wavelength | BC layer | | | | TGO layer | | | | TBC layer | | | |
|---|---|---|---|---|---|---|---|---|---|---|---|---|---|---|
| | | | $\sigma_{max}$ | $\Delta\sigma$ | $\sigma_{min}$ | $\Delta\sigma$ | $\sigma_{max}$ | $\Delta\sigma$ | $\sigma_{min}$ | $\Delta\sigma$ | $\sigma_{max}$ | $\Delta\sigma$ | $\sigma_{min}$ | $\Delta\sigma$ |
| | [$\mu m$] | [$\mu m$] | [MPa] | [%] | [MPa] | [%] | [MPa] | [%] | [MPa] | [%] | [MPa] | [%] | [MPa] | [%] |
| Semicircle | 15 | 60 | 875.9 | -10 | -323.5 | -19 | 75.54 | -72 | -2087 | 32 | 117.3 | 50 | -126.5 | 34 |
| Semi-ellipsoid | 15 | 90 | 609.9 | -37 | -280.4 | -30 | 681.2 | 156 | -2447 | 54 | 162.1 | 107 | -115.4 | 23 |

Table 10: Long term simulation of the reference case. The maximum tensile and compressive stress values and their differences ($\Delta\sigma = \frac{\sigma_j^i - \sigma_j^i|_{Ref.case}}{\sigma_j^i|_{Ref.case}}$, where: i=BC,TGO,TBC; j=min,max; $\sigma_j^i|_{Ref.case}$ taken from Tab. 3 for the reference case after 161 cycles) obtained for all three layers after the last simulated cycle at RT are compared to stress values obtained after 161 cycles.

| Cycle | BC layer | | | | TGO layer | | | | TBC layer | | | |
|---|---|---|---|---|---|---|---|---|---|---|---|---|
| | $\sigma_{max}$ | $\Delta\sigma$ | $\sigma_{min}$ | $\Delta\sigma$ | $\sigma_{max}$ | $\Delta\sigma$ | $\sigma_{min}$ | $\Delta\sigma$ | $\sigma_{max}$ | $\Delta\sigma$ | $\sigma_{min}$ | $\Delta\sigma$ |
| | [MPa] | [%] | [MPa] | [%] | [MPa] | [%] | [MPa] | [%] | [MPa] | [%] | [MPa] | [%] |
| 621 | 1023 | 6 | -409.7 | 3 | 576.2 | 116 | 1826 | -215 | 110.2 | 41 | -112.7 | 20 |

Table 11: The maximum tensile and compressive stress values and their differences ($\Delta\sigma = \frac{\sigma_j^i - \sigma_j^i|_{Ref.case}}{\sigma_j^i|_{Ref.case}}$, where: i=BC,TGO,TBC; j=min,max; $\sigma_j^i|_{Ref.case}$ taken from Tab. 3 for the reference case) obtained for all three layers after the last simulated cycle at RT are compared to stress values obtained for the reference case. Crack formation simulation.

| BC layer | | | | TGO layer | | | | TBC layer | | | |
|---|---|---|---|---|---|---|---|---|---|---|---|
| $\sigma_{max}$ | $\Delta\sigma$ | $\sigma_{min}$ | $\Delta\sigma$ | $\sigma_{max}$ | $\Delta\sigma$ | $\sigma_{min}$ | $\Delta\sigma$ | $\sigma_{max}$ | $\Delta\sigma$ | $\sigma_{min}$ | $\Delta\sigma$ |
| [MPa] | [%] | [MPa] | [%] | [MPa] | [%] | [MPa] | [%] | [MPa] | [%] | [MPa] | [%] |
| 710.5 | -27 | -340.7 | -15 | 1198 | 350 | -1492 | -6 | 145.6 | 86 | -87.42 | -7 |

# Bibliography


[1] ABAQUS, Inc., Rising Sun Mills 166 Valley Street Providence RI 02909-2499 http://www.abaqus.com. *ABAQUS Analysis User's Manual*, version 6.5 edition, 2005. Volume IV: Elements.

[2] M. AHRENS, S. LAMPENSCHERF, R. VASSEN, AND D. STÖVER. Sintering and creep processes in plasma-sprayed thermal barrier coatings. *Journal of Thermal Spray Technology*, **33**:432–442, 2004.

[3] M. AHRENS, R. VASSEN, AND D. STÖVER. Stress distributions in plasma-sprayed thermal barrier coatings as a function of interface roughness and oxide scale thickness. *Surface and Coatings Technology*, **161 and Issue 1**:26–35, 2002.

[4] M. BÄKER, J. RÖSLER, AND G. HEINZE. A parametric study of the stress state of thermal barrier coatings Part II: cooling stresses. *Acta Materialia*, **53**:469–476, 2005.

[5] M. L. BENZEGGAGH AND M. KENANE. Measurement of mixed-mode delamination fracture toughness of unidirectional glass/epoxy composites with mixed-mode bending apparatus. *Composites Science and Technology*, **56**:439–449, 1996.

[6] M. L. BENZEGGAGH AND M. KENANE. Mixed-mode delamination fracture toughness of unidirectional glass/epoxy composites under fatigue loading. *Composites Science and Technology*, **57**:597–605, 1997.

[7] H.L. BERNSTEIN. A model for the oxide growth stress and its effect on the creep of metals. *Met. Trans.*, **18A**:975–986, 1987.

[8] E. P. BUSSO. Oxidation-induced stresses in ceramic-metal interfaces. *Journal de physique*, **9**:287–296, 1999.

[9] E. P. BUSSO, J. LIN, S. SAKURAI, AND M. NAKAYAMA. A mechanistic study of oxidation-induced degradation in a plasma-sprayed thermal barrier coating system.: Part I: model formulation. *Acta mater.*, **49**:1515–1528, 2001.

[10] E.P. BUSSO, J. LIN, AND S. SAKURAI. A mechanistic study of oxidation-induced degradation in a plasma-sprayed thermal barrier coating system. Part II: life prediction model. *Acta mater.*, **49**:1529–1536, 2001.

[11] M. CALIEZ, F. FEYEL J. L. CHABOCHE, AND S. KRUCH. Numerical simulation of EBPVD thermal barrier coatings spallation. *Acta Materialia*, **51**:1133–1141, 2003.

[12] G.C. CHANG, W. PHUCHAROEN, AND M. MILLER. Behaviour of thermal barrier coatings for advanced gas turbine blades. *Surface and Coatings Technology*, **30**:13–28, 1987.

[13] J. CHENG, E. H. JORDAN, B. BARBER, AND M. GELL. Thermal/residual stress in an electron beam physical vapor deposited thermal barrier coating system. *Acta mater.*, **46**(16):5839–5850, 1998.

[14] ROBERT D. COOK. *Finite Element Modeling for Stress Analysis*. Wiley, 1995.

[15] H. ECHSLER. *Oxidationsverhalten und mechanische Eigenschaften von Waermedaemmschichten und deren Einfluss auf eine Lebensdauervorhersage*. PhD thesis, der Rheinisch-Westfälischen Technischen Hochschule Aachen, 2003. ISBN 3-8322-1895-5.

[16] H. ECHSLER, V. SHEMET, M. SCHÜTZE, L. SINGHEISER, AND W.J. QUADAKKERS. Cracking in and around the thermally grown oxide in thermal barrier coatings: a comparison of isothermal and cyclic oxidation. *Journal of Materials Science*, **41**:1047–1058, 2006.

[17] A. G. EVANS, M. Y. HE, AND J. W. HUTCHINSON. Mechanics-based scaling laws for the durability of thermal barrier coatings. *Progress in Materials Science*, **46**:249–271, 2001.

[18] A.G. EVANS, D.R. MUMM, J.W. HUTCHINSON, G.H. MEIER, AND F.S. PETTIT. Mechanisms controlling the durability of thermal barrier coatings. *Progress in Materials Science*, **46**:505–553, 2001.

[19] H.E. EVANS. Stress effects in high temperature oxidation of metals. *Inter. Mater. Rev.*, **40**:1–40, 1995.

[20] A. M. FREBORG, B.L. FERGUSON, W.J. BRINDLEY, AND G.J. PETRUS. Modeling oxidation induced stresses in thermal barrier coatings. *Material Science and Engineering A*, **245**:182–190, 1998. Issue 2.

[21] M. Y. HE, A. G. EVANS, AND J. W. HUTCHINSON. The ratcheting of compressed thermally grown thin films on ductile substrates. *Acta mater.*, **48**:2593–2601, 2000.

[22] M. Y. HE, J. W. HUTCHINSON, AND A. G. EVANS. Large deformation simulations of cyclic displacement instabilities in thermal barrier systems. *Acta Materialia*, **50**:1063–107, 2002.

[23] M. Y. HE, J. W. HUTCHINSON, AND A. G. EVANS. Simulation of stresses and delamination in a plasma-sprayed thermal barrier system upon thermal cycling. *Materials Science and Engineering A*, **345**:172–178, 2003.

[24] S. HECKMANN, R. HERZOG, R. STEINBRECH, F. SCHUBERT, AND L. SINGHEISER. Visco-plastc properties of separated thermal barrier coatings under compression loading. In *Materials for Advanced Power Engineering 2002*, **21**, pages 561–568, Liege, Belgium, Proceedings of the 7th Liege Conference 2002, 30. September - 2. October 2002. ISBN 3-89336-213-2.

[25] SIMON HECKMANN. *Ermittlung des Verformungs- und Schädigungsverhaltens von Wärmedämmschichtsystemen*. PhD thesis, Von der Fakultät für Maschinenwesen der Rheinisch-Westfälischen Technischen Hochschule Aachen, 2003.

[26] R. HERZOG, P. BEDNARZ, E. TRUNOVA, V. SHEMET, R.W. STEINBRECH, F. SCHUBERT, AND L. SINGHEISER. Simulation of stress development and crack formation in APS-TBCs for cyclic oxidation loading and comparison with experimental observations. Proceedings of the 30th International Conference and Exposition on Advanced Ceramics and Composites 2006.

[27] C. H. HSUEH AND E. R. FULLER. Analytical modeling of oxide thickness effects on residual stresses in thermal barrier coatings. *Scripta Materialia*, **42**:781–787, 2000.

[28] CHUN-HWAY HSUEH AND EDWIN R. FULLER JR. Residual stresses in thermal barrier coatings: effects of interface asperity curvature/height and oxide thickness. *Material Science and Engineering A*, **283**:46–55, 2000.

[29] AMOL JADHAV, NITIN P. PADTURE, FANG WU, ERIC H. JORDAN, AND MAURICE GELL. Thick ceramic thermal barrier coatings with high durability deposited using solution-precursor plasma spray. *Materials Science and Engineering A*, **405**:313–320, 2005.

[30] M. JINNESTRAND AND S. SJÖSTRÖM. Investigation by 3D FE simulations of delamination crack initiation in TBC caused by alumina growth. *Surface and Coatings Technology*, **135**:188–195, 2001.

[31] A. M. KARLSSON, J.W. HUTCHINSON, AND A. G. EVANS. A fundamental model of cyclic instabilities in thermal barrier systems. *J. Mech. and Physics Solids*, **50**:1565–1589, 2002.

[32] A. M. KARLSSON, C. G. LEVI, AND A. G. EVANS. A model study of displacement instabilities during cyclic oxidation. *Acta Materialia*, **50**:1263–1273, 2002.

[33] A. M. KARLSSON, T. XU, AND A. G. EVANS. The effect of the thermal barrier coating on the displacement instability in thermal barrier systems. *Acta Materialia*, **50**:1211–1218, 2002.

[34] A.M. KARLSSON AND A.G. EVANS. A numerical model for the cyclic instability of thermally grown oxides in thermal barrier systems. *Acta mater.*, **49**:1793–1804, 2001.

[35] DARYL L. LOGAN. *A First Course in the Finite Element Method*. Brooks-Cole, 3 edition, 2002.

[36] P. MAJERUS, R.W. STEINBRECH, R. HERZOG, AND F. SCHUBERT. Deformation behaviour of a low pressure plasma-sprayed NiCoCrAlY bond coat under shear loading at temperatures above 750 c. In *Materials for Advanced Power Engineering 2002*, Proceedings of the 7th Liege Conference 2002, 30. September - 2. October 2002 2004. ISBN 3-89336-213-2.

[37] PATRICK MAJERUS. *Neue Verfahren zur Analyse des Verformungs- und Schädigungsverhaltens von MCrAlY-Schichten im Wärmedämmschichtsystem*. PhD thesis, Von der Fakultät für Maschinenwesen der Rheinisch-Westfälischen Technischen Hochschule Aachen, 2003.

[38] D. R. MUMM, M. WATANABE, A. G. EVANS, AND J. A. PFAENDTNER. The influence of test method on failure mechanisms and durability of a thermal barrier system. *Acta Materialia*, **52**:1123–1131, 2004.

[39] NITIN P. PADTURE, MAURICE GELL, , AND ERIC H. JORDAN. Thermal barrier coatings for gas-turbine engine applications. *Science*, **296**:280–284, 2002.

[40] MAREK-JERZY PINDERA, JACOB ABOUDI, AND STEVEN M. ARNOLD. The effect of interface roughness and oxide film thickness on the inelastic response of thermal barrier coatings to thermal cycling. *Material Science and Engineering A*, **284**:158–175, 2000.

[41] MAREK-JERZY PINDERA, JACOB ABOUDI, AND STEVEN M. ARNOLD. Analysis of spallation mechanism in thermal barrier coatings with graded bond coats using the higher-order theory for FGMs. *Engineering Fracture Mechanics*, **69**:1587–1606, 2002.

[42] J. RÖSLER. Mechanical integrity of thermal barrier coated material systems . *Advanced Engineering Materials*, **7**:50–54, 2005.

[43] J. RÖSLER, M. BÄKER, AND K. AUFZUG. A parametric study of the stress state of thermal barrier coatings, Part I: creep relaxation. *Acta Materialia*, **52**:4809–4817, 2004.

[44] J. RÖSLER, M. BÄKER, AND M. VOLGMANN. Stress state and failure mechanisms of thermal barrier coatings: role of creep in thermally grown oxide. *Acta mater.*, **49**:3659–3670, 2001.

[45] K.W. SCHLICHTING, N.P. PADTURE, E.H. JORDAN, AND M. GELL. Failure modes in plasma-sprayed thermal barrier coatings. *Materials Science and Engineering A*, **342**:120–130, 2003.

[46] J. SCHWARZER, D. LÖHE, AND O. VÖHRINGER. Influence of the TGO creep behavior on delamination stress development in thermal barrier coating systems. *Materials Science and Engineering A*, **387-389**:692–695, 2004.

[47] K. SFAR, J. AKTAA, AND D. MUNZ. Numerical investigation of residual stress fields and crack behavior in TBC systems. *Materials Science and Engineering A*, **333**:351–360, 2002.

[48] I. M. SMITH AND D. V. GRIFFITHS. *Programming the Finite Element Method*. Wiley & Sons, Chichester, 4 edition, 2004.

[49] F. TRÄGER, M. AHRENS, R. VASSEN, AND D. STÖVER. A life time model for ceramic thermal barrier coatings. *Materials Science and Engineering A*, **358**:255–265, 2003.

[50] E. TRUNOVA, R. HERZOG, T. WAKUI, R.W. STEINBRECH, E. WESSEL, AND L. SINGHEISER. Micromechanisms affecting macroscopic deformation of plasma-sprayed TBCs. In *Ceramic Engineering and Science Proceedings*, **25, Issue 4**, pages 411–416, 2004. 28th International Conference on Advanced Ceramics and Composites, B.

[51] R. VASSEN, G. KERKHOFF, AND D. STÖVER. Development of a micromechanical life prediction model for plasma sprayed thermal barrier coatings. *Materials Science and Engineering A*, **303**:100–109, 2001.

[52] T. XU, M. Y. HE, AND A. G. EVANS. A numerical assessment of the durability of thermal barrier systems that fail by ratcheting of the thermally grown oxide. *Acta Materialia*, **51**:3807–3820, 2003.

[53] H.X. ZHU, N.A. FLECK, A.C.F. COCKS, AND A.G. EVANS. Numerical simulations of crack formation from pegs in thermal barrier systems with nicocraly bond coats. *Materials Science and Engineering A*, **404**:26–32, 2005.

[54] OLGIERD C. ZIENKIEWICZ AND R. L. TAYLOR. *The Finite Element Method for Solid and Structural Mechanics*. Elsevier, 6 edition, 2005.

[55] OLGIERD C. ZIENKIEWICZ, R. L. TAYLOR, AND J.Z. ZHU. *The Finite Element Method: Its Basis and Fundamentals*. Elsevier, 6 edition, 2005.

Schriften des Forschungszentrums Jülich
Reihe Energietechnik / Energy Technology

1. **Fusion Theory**
   Proceedings of the Seventh European Fusion Theory Conference
   edited by A. Rogister (1998); X, 306 pages
   ISBN: 978-3-89336-219-6

2. **Radioactive Waste Products 1997**
   Proceedings of the 3rd International Seminar on Radioactive Waste Products held in Würzburg (Germany) from 23 to 26 June 1997
   edited by R. Odoj, J. Baier, P. Brennecke et al. (1998), XXIV, 506 pages
   ISBN: 978-3-89336-225-7

3. **Energieforschung 1998**
   Vorlesungsmanuskripte des 4. Ferienkurs „Energieforschung“
   vom 20. bis 26. September 1998 im Congrescentrum Rolduc und
   im Forschungszentrum Jülich
   herausgegeben von J.-Fr. Hake, W. Kuckshinrichs, K. Kugeler u. a. (1998),
   500 Seiten
   ISBN: 978-3-89336-226-4

4. **Materials for Advances Power Engineering 1998**
   Abstracts of the 6th Liège Conference
   edited by J. Lecomte-Beckers, F. Schubert, P. J. Ennis (1998), 184 pages
   ISBN: 978-3-89336-227-1

5. **Materials for Advances Power Engineering 1998**
   Proceedings of the 6th Liège Conference
   edited by J. Lecomte-Beckers, F. Schubert, P. J. Ennis (1998),
   Part I XXIV, 646, X pages; Part II XXIV, 567, X pages; Part III XXIV, 623, X pages
   ISBN: 978-3-89336-228-8

6. **Schule und Energie**
   1. Seminar Energiesparen, Solarenergie, Windenergie. Jülich, 03. und 04.06.1998
   herausgegeben von P. Mann, W. Welz, D. Brandt, B. Holz (1998), 112 Seiten
   ISBN: 978-3-89336-231-8

7. **Energieforschung**
   Vorlesungsmanuskripte des 3. Ferienkurses „Energieforschung“
   vom 22. bis 30. September 1997 im Forschungszentrum Jülich
   herausgegeben von J.-Fr. Hake, W. Kuckshinrichs, K. Kugeler u. a. (1997),
   505 Seiten
   ISBN: 978-3-89336-211-0

8. **Liberalisierung des Energiemarktes**
   Vortragsmanuskripte des 5. Ferienkurs „Energieforschung“
   vom 27. September bis 1. Oktober 1999 im Congrescentrum Rolduc und
   im Forschungszentrum Jülich
   herausgegeben von J.-Fr. Hake, A. Kraft, K. Kugeler u. a. (1999), 350 Seiten
   ISBN: 978-3-89336-248-6

9. **Models and Criteria for Prediction of Deflagration-to-Detonation Transition (DDT) in Hydrogen-Air-Steam-Systems under Severe Accident Conditions**
   edited by R. Klein, W. Rehm (2000), 178 pages
   ISBN: 978-3-89336-258-5

10. **High Temperature Materials Chemistry**
    Abstracts of the 10th International IUPAC Conference, April 10 - 14 2000, Jülich
    edited by K. Hilpert, F. W. Froben, L. Singheiser (2000), 292 pages
    ISBN: 978-3-89336-259-2

11. **Investigation of the Effectiveness of Innovative Passive Safety Systems for Boiling Water Reactors**
    edited by E. F. Hicken, K. Verfondern (2000), X, 287 pages
    ISBN: 978-3-89336-263-9

12. **Zukunft unserer Energieversorgung**
    Vortragsmanuskripte des 6. Ferienkurs „Energieforschung“
    vom 18. September bis 22. September 2000 im Congrescentrum Rolduc und
    im Forschungszentrum Jülich
    herausgegeben von J.-Fr. Hake, S. Vögele, K. Kugeler u. a. (2000),
    IV, 298 Seiten
    ISBN: 978-3-89336-268-4

13. **Implementing Agreement 026**
    For a Programme of Research, Development and Demonstration on Advanced Fuel Cells: Fuel Cell Systems for Transportation. Annex X. Final Report 1997 - 1999
    edited by B. Höhlein; compiled by P. Biedermann (2000), 206 pages
    ISBN: 978-3-89336-275-2

14. **Vorgespannte Guß-Druckbehälter (VGD) als berstsichere Druckbehälter für innovative Anwendungen in der Kerntechnik**
    Prestressed Cast Iron Pressure Vessels as Burst-Proof Pressure Vessels for Innovative Nuclear Applications
    von W. Fröhling, D. Bounin, W. Steinwarz u. a. (2000) XIII, 223 Seiten
    ISBN: 978-3-89336-276-9

15. **High Temperature Materials Chemistry**
    Proceedings of the 10th International IUPAC Conference
    held from 10 to 14 April 2000 at the Forschungszentrum Jülich, Germany
    Part I and II
    edited by K. Hilpert, F. W. Froben, L. Singheiser (2000), xvi, 778, VII pages
    ISBN: 978-3-89336-259-2

16. **Technische Auslegungskriterien und Kostendeterminanten von SOFC- und PEMFC-Systemen in ausgewählten Wohn- und Hotelobjekten**
    von S. König (2001), XII, 194 Seiten
    ISBN: 978-3-89336-284-4

17. **Systemvergleich: Einsatz von Brennstoffzellen in Straßenfahrzeugen**
    von P. Biedermann, K. U. Birnbaum, Th. Grube u. a. (2001), 185 Seiten
    ISBN: 978-3-89336-285-1

18. **Energie und Mobilität**
    Vorlesungsmanuskripte des 7. Ferienkurs „Energieforschung“
    vom 24. September bis 28. September 2001 im Congrescentrum Rolduc und im Forschungszentrum Jülich
    herausgegeben von J.-Fr. Hake, J. Linßen, W. Pfaffenberger u. a. (2001), 205 Seiten
    ISBN: 978-3-89336-291-2

19. **Brennstoffzellensysteme für mobile Anwendungen**
    von P. Biedermann, K. U. Birnbaum, Th. Grube u. a. (2002)
    PDF-Datei auf CD
    ISBN: 978-3-89336-310-0

20. **Materials for Advances Power Engineering 2002**
    Abstracts of the 7th Liège Conference
    edited by J. Lecomte-Beckers, M. Carton, F. Schubert, P. J. Ennis (2002), c. 200 pages
    ISBN: 978-3-89336-311-7

21. **Materials for Advanced Power Engineering 2002**
    Proceedings of the 7th Liège Conference
    Part I, II and III
    edited by J. Lecomte-Beckers, M. Carton, F. Schubert, P. J. Ennis (2002), XXIV, 1814, XII pages
    ISBN: 978-3-89336-312-4

22. **Erneuerbare Energien: Ein Weg zu einer Nachhaltigen Entwicklung?**
    Vorlesungsmanuskripte des 8. Ferienkurs „Energieforschung“
    vom 23. bis 27. September 2002 in der Jakob-Kaiser-Stiftung, Königswinter
    herausgegeben von J.-Fr. Hake, R. Eich, W. Pfaffenberger u. a. (2002), IV, 230 Seiten
    ISBN: 978-3-89336-313-1

23. **Einsparpotenziale bei der Energieversorgung von Wohngebäuden durch Informationstechnologien**
    von A. Kraft (2002), XII, 213 Seiten
    ISBN: 978-3-89336-315-5

24. **Energieforschung in Deutschland**
    Aktueller Entwicklungsstand und Potentiale ausgewählter nichtnuklearer Energietechniken
    herausgegeben von M. Sachse, S. Semke u. a. (2002), II, 158 Seiten, zahlreiche farb. Abb.
    ISBN: 978-3-89336-317-9

25. **Lebensdaueranalysen von Kraftwerken der deutschen Elektrizitätswirtschaft**
    von A. Nollen (2003), ca. 190 Seiten
    ISBN: 978-3-89336-322-3

26. **Technical Session: Fuel Cell Systems of the World Renewable Energy Congress VII**
    Proceedings
    edited by D. Stolten and B. Emonts (2003), VI, 248 pages
    ISBN: 978-3-89336-332-2

27. **Radioactive Waste Products 2002 (RADWAP 2002)**
    Proceedings
    edited by R. Odoj, J. Baier, P. Brennecke and K. Kühn (2003), VI, 420 pages
    ISBN: 978-3-89336-335-3

28. **Methanol als Energieträger**
    von B. Höhlein, T. Grube, P. Biedermann u. a. (2003), XI, 109 Seiten
    ISBN: 978-3-89336-338-4

29. **Hochselektive Extraktionssysteme auf Basis der Dithiophosphinsäuren: Experimentelle und theoretische Untersuchungen zur Actinoiden(III)-Abtrennung**
    von S. A. H. Nabet (2004), VI, 198 Seiten
    ISBN: 978-3-89336-351-3

30. **Benchmarking-Methodik für Komponenten in Polymerelektrolyt-Brennstoffzellen**
    von Matthias Gebert (2004), 194 Seiten
    ISBN: 978-3-89336-355-1

31. **Katalytische und elektrochemische Eigenschaften von eisen- und kobalthaltigen Perowskiten als Kathoden für die oxidkeramische Brennstoffzelle (SOFC)**
    von Andreas Mai (2004), 100 Seiten
    ISBN: 978-3-89336-356-8

32. **Energy Systems Analysis for Political Decision-Making**
edited by J.-Fr. Hake, W. Kuckshinrichs, R. Eich (2004), 180 pages
ISBN: 978-3-89336-365-0

33. **Entwicklung neuer oxidischer Wärmedämmschichten für Anwendungen in stationären und Flug-Gasturbinen**
von R. Vaßen (2004), 141 Seiten
ISBN: 978-3-89336-367-4

34. **Neue Verfahren zur Analyse des Verformungs- und Schädigungsverhaltens von MCrAlY-Schichten im Wärmedämmschichtsystem**
von P. Majerus (2004), 157 Seiten
ISBN: 978-3-89336-372-8

35. **Einfluss der Oberflächenstrukturierung auf die optischen Eigenschaften der Dünnschichtsolarzellen auf der Basis von a-Si:H und µc-Si:H**
von N. Senoussaoui (2004), 120 Seiten
ISBN: 978-3-89336-378-0

36. **Entwicklung und Untersuchung von Katalysatorelementen für innovative Wasserstoff-Rekombinatoren**
von I.M. Tragsdorf (2005), 119 Seiten
ISBN: 978-3-89336-384-1

37. **Bruchmechanische Untersuchungen an Werkstoffen für Dampfkraftwerke mit Frischdampftemperaturen von 500 bis 650°C**
von L. Mikulová (2005), 149 Seiten
ISBN: 978-3-89336-391-9

38. **Untersuchungen der Strukturstabilität von Ni-(Fe)-Basislegierungen für Rotorwellen in Dampfturbinen mit Arbeitstemperaturen über 700 °C**
von T. Seliga (2005), 106 Seiten
ISBN: 978-3-89336-392-6

39. **IWV-3 Report 2005. Zukunft als Herausforderung**
(2005), 115 Seiten
ISBN: 978-3-89336-393-3

40. **Integrierter Photodetektor zur Längenmessung**
von E. Bunte (2005), XI, 110 Seiten
ISBN: 978-3-89336-397-1

41. **Microcrystalline Silicon Films and Solar Cells Investigated by Photoluminescence Spectroscopy**
by T. Merdzhanova (2005), X, 137 pages
ISBN: 978-3-89336-401-5

42. **IWV-3 Report 2005. Future as a challenge**
(2005), 115 pages
ISBN: 978-3-89336-405-3

43. **Electron Spin Resonance and Transient Photocurrent Measurements on Microcrystalline Silicon**
by T. Dylla (2005), X, 138 pages
ISBN: 978-3-89336-410-7

44. **Simulation und Analyse des dynamischen Verhaltens von Kraftwerken mit oxidkeramischer Brennstoffzelle (SOFC)**
von M. Finkenrath (2005), IV, 155 Seiten
ISBN: 978-3-89336-414-5

45. **The structure of magnetic field in the TEXTOR-DED**
by K.H. Finken, S.S. Abdullaev, M. Jakubowski, M. Lehnen, A. Nicolai, K.H. Spatschek (2005), 113 pages
ISBN: 978-3-89336-418-3

46. **Entwicklung und Modellierung eines Polymerelektrolyt-Brennstoffzellenstapels der 5 kW Klasse**
von T. Wüster (2005), 211 Seiten
ISBN: 978-3-89336-422-0

47. **Die Normal-Wasserstoffelektrode als Bezugselektrode in der Direkt-Methanol-Brennstoffzelle**
von M. Stähler (2006), VI, 96 Seiten
ISBN: 978-3-89336-428-2

48. **Stabilitäts- und Strukturmodifikationen in Katalysatordispersionen der Direktmethanolbrennstoffzelle**
von C. Schlumbohm (2006), II, 211 Seiten
ISBN: 978-3-89336-429-9

49. **Eduktvorbereitung und Gemischbildung in Reaktionsapparaten zur autothermen Reformierung von dieselähnlichen Kraftstoffen**
von Z. Porš (2006), XX, 182, XII Seiten
ISBN: 978-3-89336-432-9

50. **Spektroskopische Untersuchung der poloidalen Plasmarotation unter dem Einfluß statischer und dynamischer Ergodisierung am Tokamak TEXTOR**
von C. Busch (2006), IV, 81 Seiten
ISBN: 978-3-89336-433-6

51. **Entwicklung und Optimierung von Direktmethanol-Brennstoffzellstapeln**
von M. J. Müller (2006), 167 Seiten
ISBN: 978-3-89336-434-3

52. **Untersuchung des reaktiven Sputterprozesses zur Herstellung von aluminiumdotierten Zinkoxid-Schichten für Silizium-Dünnschichtsolarzellen**
von J. Hüpkes (2006), XIV, 170 Seiten
ISBN: 978-3-89336-435-0

53. **Materials for Advanced Power Engineering 2006**
Proceedings of the 8th Liège Conference
Part I, II and III
edited by J. Lecomte-Beckers, M. Carton, F. Schubert, P. J. Ennis (2006), Getr. Pag.
ISBN: 978-3-89336-436-7

54. **Verdampfung von Werkstoffen beim Betrieb von Hochtemperaturbrennstoffzellen (SOFC)**
von M. Stanislowski (2006), IV, 154 Seiten
ISBN: 978-3-89336-438-1

55. **Methanol as an Energy Carrier**
edited by P. Biedermann, Th. Grube, B. Höhlein (2006), XVII, 186 Seiten
ISBN: 978-3-89336-446-6

56. **Kraftstoffe und Antriebe für die Zukunft**
Vorlesungsmanuskripte des 1. Herbstseminars „Kraftstoffe und Antriebe für die Zukunft“ vom 9.-13. Oktober 2006 an der TU Berlin
herausgegeben von V. Schindler, C. Funk, J.-Fr. Hake, J. Linßen (2006), VIII, 221 Seiten
ISBN: 978-3-89336-452-7

57. **Plasma Deposition of Microcrystalline Silicon Solar Cells: Looking Beyond the Glass**
by M. N. van den Donker (2006), VI, 110 pages
ISBN: 978-3-89336-456-5

58. **Nuclear Energy for Hydrogen Production**
by K. Verfondern (2007), 186 pages
ISBN: 978-3-89336-468-8

59. **Kraft-Wärme-Kopplung mit Brennstoffzellen in Wohngebäuden im zukünftigen Energiesystem**
von C. H. Jungbluth (2007), XI, 197 Seiten
ISBN: 978-3-89336-469-5

60. **Finite Element Simulation of Stress Evolution in Thermal Barrier Coating Systems**
by P. Bednarz (2007), XIV, 121 pages
ISBN: 978-3-89336-471-8

This book guides you through different numerical approaches to model Thermal Barrier Coating Systems (TBCs). Its main contribution consists of a stepwise improvement of a very simple numerical simulation into a highly complex Finite Element Model that considers all main influencing parameters of thermal loading on the failure behavior of Thermal Barrier Coating Systems in gas turbines. The results of these simulations allow precise validation of the simulations and identify several possibilities to enhance the performance of Thermal Barrier Coatings.

## Author

**Piotr Bednarz** studied at the Warsaw University of Technology, Faculty of Power and Aeronautical Engineering, Poland. Since February 2003 he has worked at the Research Centre Juelich, Institute of Energy Research, IEF-2: Microstructure and Properties of Materials. His research topic is the finite element simulation of the stress evolution in thermal barrier coating systems. The contents of this book have been submitted to the Technical University of Aachen (RWTH Aachen) in fulfilment of the requirements for a Doctor of Engineering degree.

## Institute of Energy Research
## IEF-2 Materials Microstructure and Characterization

The research topics of IEF-2 are focussed on the development and characterization of materials for efficient gas and steam power plants, for high temperature fuel cells and for future fusion reactor components subjected to high thermal loads. The scientific expertises of the institute cover microstructural investigations, surface analysis techniques and the physical, chemical, mechanical and corrosion behaviour of metallic high temperature materials and of ceramic materials used either as structural components or as elements of coating systems.

Forschungszentrum Jülich
*in der Helmholtz-Gemeinschaft*

50 Jahre / Zukunft

**Band / Volume 60**
**ISBN 978-3-89336-471-8**

**Energietechnik**
**Energy Technology**